ABSTRACT

Title of Dissertation: RANDOM PULSE SEQUENCES FOR QUANTUM NOISE SPECTROSCOPY

Kaixin Huang
Doctor of Philosophy, 2025

Dissertation Directed by: Professor Yi-Kai Liu
Institute for Advanced Computer Studies

Qubit noise spectroscopy is an important tool for the experimental investigation of open quantum systems. However, conventional techniques for noise spectroscopy are time-consuming, because they require measurements of the noise spectral density at many different frequencies. In this dissertation, I describe an alternative approach to noise spectroscopy, which requires fewer resources, and relies on direct measurement of arbitrary linear functionals of the noise spectral density. This method uses random pulse sequences with carefully-controlled correlations, which are chosen using algorithms for phase retrieval. These measurements allow us to reconstruct sparse noise spectra via compressed sensing. Our simulations of the performance of the random pulse sequences on a realistic physical system, self-assembled quantum dots, reveal a speedup of an order of magnitude in extracting the noise spectrum, compared to conventional dynamical decoupling approaches.

I also advance this method in two complementary directions: expanding its applicability to a larger class of noise spectra, and simplifying its implementation. First, we extend the

random pulse sequences method to reconstruct piecewise-linear noise spectra, which more realistically model many physical systems. We show through numerical simulations that the new method resolves finer spectral features while maintaining an order-of-magnitude speedup over conventional approaches to noise spectroscopy. Second, we introduce a simplified variant using Rademacher measurements, optimized for sparse spectra, that greatly reduces experimental complexity without compromising reconstruction accuracy. Together, these developments broaden the reach of random pulse sequences noise spectroscopy and enhance its practicality for high-resolution, resource-efficient noise characterization in realistic quantum systems.

RANDOM PULSE SEQUENCES FOR QUANTUM NOISE SPECTROSCOPY

by

Kaixin Huang

Dissertation submitted to the Faculty of the Graduate School of the
University of Maryland, College Park in partial fulfillment
of the requirements for the degree of
Doctor of Philosophy
2025

Advisory Committee:
Professor Mohammad Hafezi, Chair/Co-Advisor
Professor Yi-Kai Liu, Advisor
Professor Alexey Gorshkov
Professor Victor M. Yakovenko
Professor Daniel Gottesman

© Copyright by
Kaixin Huang
2025

Acknowledgments

It is nearly impossible to thank everyone who contributed to the successful completion of this dissertation. Some of those mentioned here may not even recall their contribution, but their influence was substantial and will not be forgotten.

First and foremost, I would like to express my deepest gratitude to my advisor, Professor Yi-Kai Liu, for his invaluable guidance, patience, and insight throughout my Ph.D. journey. I am especially grateful for his constant encouragement and trust, which allowed me the freedom to explore ideas and go through difficult times. I would also like to sincerely thank my co-advisor, Professor Mohammad Hafezi, for his mentorship and inspiring perspective on physics.

I am deeply indebted to my collaborators — Demitry Farfurnik, Alireza Seif, Dror Baron, Yuxin Wang, and many others. Working with them has been one of the most rewarding aspects of my doctoral experience.

I am also deeply grateful to the graduate office. My time in the program has been immeasurably smoother thanks to the generous help and guidance of Josiland Chambers, Donna Hammer, and Tom Cohen.

I would like to thank my family for their unwavering love, understanding, and encouragement. Their support has been a constant source of strength and motivation through the many ups and downs of my graduate life.

I am also grateful to my friends and roommates — Shuyang Wang, Haining Pan, Hao-

nan Xiong, Fei Wu, Su-Kuan Chu and Yunsheng Liu — for their companionship, humor, and countless moments of joy that made this journey lighter and more memorable.

Lastly, I would like to thank my cat, Minga, for being my quiet companion during the long nights of writing and coding. Her presence has brought warmth and comfort to my days.

Thanks to everyone who helped me along the way.

Table of Contents

Acknowledgements ii

Table of Contents iv

List of Figures vi

List of Tables vii

List of Publications viii

Chapter 1: Introduction 1
- 1.1 Motivation . . . 1
- 1.2 Quantum Noise . . . 3
  - 1.2.1 The Open-System Framework . . . 4
  - 1.2.2 Noise in a Qubit Hamiltonian . . . 5
  - 1.2.3 Gaussian and Non-Gaussian Noise . . . 6
  - 1.2.4 Classical vs. Quantum Noise . . . 7
  - 1.2.5 Typical Spectral Forms of Noise . . . 7
- 1.3 Quantum Noise Spectroscopy . . . 8
  - 1.3.1 The Filter-Function Formalism . . . 9
  - 1.3.2 Ramsey and Hahn-Echo Spectroscopy . . . 10
  - 1.3.3 Robust and Composite Pulse Techniques . . . 11
- 1.4 Compressed sensing . . . 11
  - 1.4.1 The Basic Principle . . . 12
  - 1.4.2 Measurement Design and Incoherence . . . 14
  - 1.4.3 Restricted Isometry Property and Recovery Guarantees . . . 14
  - 1.4.4 Algorithms for Realistic Signals . . . 15
  - 1.4.5 Extensions Beyond Classical Sparsity . . . 16
- 1.5 Outline of the Thesis . . . 18

Chapter 2: Random Pulse Sequences 20
- 2.1 Introduction . . . 20
- 2.2 Noise Model . . . 22
- 2.3 Protocols for noise spectroscopy . . . 25
  - 2.3.1 Dynamical decoupling . . . 28
- 2.4 Random pulse sequences . . . 30
- 2.5 Approximating a desired window function . . . 35

2.6 Measuring Linear Functionals of $S(\omega)$ . . . 39
2.7 Accuracy of the method . . . 43
2.7.1 Variance of the decay exponent: the uncorrelated case . . . 44
2.7.2 Variance of the decay exponent: the general case . . . 45
2.7.3 Experimental estimation of the decay exponent . . . 51
2.7.4 Accuracy of the estimator . . . 52
2.8 Alternative generator . . . 57
2.9 Applications to 1-D Chain Mapping of Open Quantum Systems . . . 60
2.9.1 Numerical example . . . 63

Chapter 3: Compressed Sensing with Random Pulses 65
3.1 Theory . . . 66
3.2 Numerical Examples . . . 68
3.3 Application to Quantum Dots . . . 70
3.4 Experimental Demonstration . . . 73
3.5 Outlook . . . 77

Chapter 4: Piecewise Linear Modeling and Rademacher Measurements 79
4.1 Introduction . . . 79
4.2 Model . . . 82
4.3 Estimation of Piecewise Linear Spectra . . . 84
4.4 Rademacher Measurements for Sparse Spectra . . . 87
4.5 Applications . . . 92
4.5.1 Quantum Dots . . . 92
4.5.2 Sensing with Fewer Pulses . . . 98
4.6 Outlook . . . 101

Appendix A: Appendices 103
A.1 Variance of the decay exponent: a special case . . . 103

Bibliography 106

List of Figures

2.1 A single-qubit noise spectroscopy experiment. . . . 26
2.2 An illustration of the CPMG pulse sequence. . . . 27
2.3 Illustrations of the random pulse sequence method. . . . 27
2.4 A geometric interpretation of how to generate the random pulse sequences. . . . 32
2.5 Illustrations of the generation of a target function. . . . 42
2.6 An illustration to generate the random pulses using the alternative generator. . . . 58
2.7 The t-DMRG simulation of the coherence of the qubit over time using the 1-D chain mapping technique. . . . 64

3.1 Reconstructions of ideal sparse spectra using the CS method. . . . 69
3.2 A reconstruction of the noise spectrum of an quantum dot spectrum using pulse sequences of CS. . . . 71
3.3 Numerical simulations of the accuracy of reconstructing the central frequencies. . . . 72
3.4 Reconstructions of the (artificially generated) sparse noise spectrum on commercial platforms. . . . 76
3.5 The accuracy of reconstructing the central frequencies of the injected noise spectrum on different platforms. . . . 77

4.1 Reconstructions of ideal piecewise linear spectra using the CS_{TGV} method. . . . 88
4.2 Reconstructions of an ideal sparse spectrum using the CS_R method. . . . 93
4.3 The accuracy of CS_R method. . . . 94
4.4 Reconstructions of the quantum dots noise spectrum. . . . 96
4.5 Accuracy of reconstructing the InAs/GaAs noise spectrum. . . . 97
4.6 Accuracy of reconstructing the InAs/GaAs noise spectrum with different number of pulses. . . . 100

List of Tables

3.1 Properties of qubits 75

List of Publications

Chapters 2 and 3 of this dissertation are based on material by the author that was published as

[1] K. Huang, D. Farfurnik, A. Seif, M. Hafezi, and Y.-K. Liu, Random pulse sequences for qubit noise spectroscopy, Physical Review Applied **23**, 054090 (2025).

Chapter 4 is based on material by the author that is currently under submission.

Chapter 1: Introduction

1.1 Motivation

The last two decades have witnessed extraordinary advances in the coherent control of microscopic quantum systems [1–4]. From superconducting Josephson circuits to trapped ions, semiconductor spins, and nitrogen–vacancy (NV) centers in diamond, researchers can now manipulate and measure quantum states with high precision. Yet, despite remarkable improvements in gate fidelity and coherence, decoherence—the loss of quantum phase information due to coupling with uncontrolled degrees of freedom—remains the central bottleneck toward scalable quantum technologies.

Quantum noise is the physical manifestation of the unavoidable coupling between a quantum system and its environment. It represents stochastic fluctuations—of magnetic fields, electric potentials, laser phases, phonon environments, or other microscopic variables—that act on the system and randomize its phase or energy. Understanding and quantifying these fluctuations is essential for both advancing quantum computation and enabling high-precision quantum sensing [5–8]. The field of quantum noise spectroscopy builds directly on this motivation: it seeks to treat the qubit not merely as a computational unit but as a sensitive spectrometer of its own environment, capable of revealing the spectral and statistical structure of the surrounding noise.

Reducing the impact of noise is one of the central challenges in building scalable quan-

tum computers. At the physical-control level, dynamical decoupling and related pulse-sequence techniques are designed to suppress low-frequency noise by averaging out unwanted interactions between the qubit and its environment [9–11]. At a higher, logical level, quantum error-correcting codes and fault-tolerant architectures encode information redundantly to detect and correct errors before they propagate [5, 6]. Both approaches depend critically on the properties of the underlying noise spectrum: correlations and frequency structure can all influence logical error rates and threshold conditions for fault tolerance [12–14]. Accurate noise spectroscopy therefore provides the quantitative foundation for improving both low-level control protocols and high-level error-correction strategies.

Although noise spectroscopy has been studied for decades—from early spin-echo experiments to modern dynamical-decoupling and randomized-probe protocols—new frontiers in quantum technologies continue to pose open challenges. As quantum processors grow in size and complexity, there is a pressing need for fast, scalable methods of multi-qubit noise spectroscopy that can characterize correlated noise across tens or hundreds of qubits [15, 16]. At the same time, quantum sensors and precision measurement platforms demand more accurate and efficient spectral estimation techniques that can extract high-resolution noise information without prohibitively long acquisition times [17]. Addressing these challenges requires new theoretical and computational tools that combine physical insight with data-efficient strategies, motivating the development of approaches such as compressed-sensing-based noise spectroscopy explored in this work.

In this chapter, we begin by introducing the physical foundations of quantum noise, describing how environmental coupling gives rise to dephasing, relaxation, and spectral structure. We then review the principles and techniques of quantum noise spectroscopy, showing how tai-

lored control sequences can selectively probe different parts of the noise spectrum. Finally, we introduce compressed sensing, which provides the theoretical basis for reconstructing structured or sparse spectra efficiently. Together, these three topics establish the conceptual and technical framework that underpins the developments presented in this thesis.

1.2 Quantum Noise

All realistic quantum systems interact, to some extent, with their surrounding environment. Even under highly controlled laboratory conditions—within dilution refrigerators, cryogenic vacuum chambers, or shielded optical tables—perfect isolation is unattainable. The coupling between the system and its surroundings introduces random perturbations that modify the system's Hamiltonian in time. These fluctuations, collectively referred to as *quantum noise*, are responsible for decoherence, energy relaxation, and operational errors in quantum devices.

For quantum information processing and precision sensing, where coherent superposition and entanglement are the key physical resources, environmental noise represents a fundamental limitation. Consider a qubit initialized in the superposition state

$$|\psi\rangle = \alpha\,|0\rangle + \beta\,|1\rangle\,. \tag{1.1}$$

In the absence of noise, this state would evolve unitarily, maintaining its phase coherence indefinitely. In practice, random environmental perturbations cause the relative phase between $|0\rangle$ and $|1\rangle$ to fluctuate in time, progressively reducing the off-diagonal coherence element of the qubit's density matrix. This process, known as *decoherence*, transforms a pure quantum state into a statistical mixture and is the primary obstacle to scalable quantum technologies.

1.2.1 The Open-System Framework

The theoretical framework of *open quantum systems* provides a systematic way to describe the effects of environmental coupling [18]. The total Hamiltonian can be expressed as

$$H_{\mathrm{tot}} = H_S + H_B + H_{SB}, \tag{1.2}$$

where H_S describes the system of interest, H_B represents the environmental bath, and H_{SB} captures their mutual interaction. The combined system–bath state evolves unitarily under H_{tot}, but because we typically have no access to the bath, we describe the system's dynamics through the *reduced density matrix*

$$\rho_S(t) = \mathrm{Tr}_B \left[U(t) \left(\rho_S(0) \otimes \rho_B \right) U^\dagger(t) \right], \tag{1.3}$$

where $U(t) = e^{-iH_{\mathrm{tot}}t/\hbar}$ and Tr_B denotes the trace over environmental degrees of freedom. The partial trace introduces apparent irreversibility and randomness into the system's dynamics, even though the overall evolution remains unitary. This reduced description is the mathematical origin of decoherence and energy relaxation.

Physically, the interaction Hamiltonian H_{SB} can often be expressed as a sum of tensor products of system and bath operators,

$$H_{SB}(t) = \sum_\alpha S_\alpha \otimes B_\alpha(t), \tag{1.4}$$

where S_α acts on the system and $B_\alpha(t)$ represents an environmental operator that fluctuates in

time. The environmental noise is statistically characterized by its *autocorrelation functions*

$$C_{\alpha\beta}(\tau) = \langle B_\alpha(t) B_\beta(t+\tau) \rangle_B, \tag{1.5}$$

and their Fourier transforms, the *power spectral densities (PSDs)*,

$$S_{\alpha\beta}(\omega) = \int_{-\infty}^{\infty} e^{-i\omega\tau} C_{\alpha\beta}(\tau)\, d\tau. \tag{1.6}$$

The spectral density $S(\omega)$ quantifies how strongly the environment fluctuates at frequency ω, and it serves as the fundamental object of study in quantum noise spectroscopy.

1.2.2 Noise in a Qubit Hamiltonian

For a single qubit, noise can be modeled as stochastic fluctuations in the effective magnetic or electric fields experienced by the qubit. A general form of the Hamiltonian is

$$H(t) = \frac{\hbar\omega_0}{2}\sigma_z + \frac{\hbar}{2}\left[\delta\omega_z(t)\sigma_z + \delta\omega_x(t)\sigma_x + \delta\omega_y(t)\sigma_y\right], \tag{1.7}$$

where ω_0 is the nominal transition frequency, and $\delta\omega_\alpha(t)$ are random time-dependent fluctuations. The longitudinal term $\delta\omega_z(t)$ produces random phase accumulation, leading to *pure dephasing*, whereas the transverse terms $\delta\omega_{x,y}(t)$ induce transitions between $|0\rangle$ and $|1\rangle$, causing *energy relaxation*.

For purely dephasing noise, the off-diagonal coherence decays as

$$\langle \sigma_+(t) \rangle = e^{-\chi(t)} \langle \sigma_+(0) \rangle, \tag{1.8}$$

where

$$\chi(t) = \frac{1}{\pi} \int_0^\infty S_z(\omega) |F(\omega, t)|^2 \, d\omega, \tag{1.9}$$

and $F(\omega, t)$ is a control-dependent *filter function*. This equation forms the theoretical foundation of noise spectroscopy, linking measurable decoherence to the underlying noise spectrum.

1.2.3 Gaussian and Non-Gaussian Noise

When the environment consists of many weakly coupled degrees of freedom, its cumulative effect on the system can be modeled as a *Gaussian stochastic process*. In that case, all higher-order correlations can be expressed in terms of the two-point correlation function, and the spectral density $S(\omega)$ completely determines the noise statistics. This Gaussian approximation greatly simplifies analysis and forms the basis of most theoretical treatments, such as the filter-function and master-equation formalisms.

However, many physical environments are not strictly Gaussian. In solid-state devices, for example, a small number of fluctuating two-level systems or charge traps can dominate decoherence. These few strongly coupled fluctuators generate *non-Gaussian noise*, characterized by higher-order correlations and non-exponential decay of coherence. The resulting dynamics often exhibit random telegraph behavior, spectral diffusion, or other forms of non-stationarity. Understanding and mitigating these effects remains a key challenge in modern quantum hardware development.

1.2.4 Classical vs. Quantum Noise

A further distinction arises between *classical* and *quantum* noise. Classical noise can be described as a random external field that commutes with itself at all times, while quantum noise originates from operators $B_\alpha(t)$ that obey nontrivial commutation relations. Quantum noise introduces an asymmetry between absorption and emission processes, captured by the *fluctuation–dissipation theorem*, which relates the symmetric and antisymmetric parts of the noise spectrum:

$$S^{(\pm)}(\omega) = \frac{1}{2}\int_{-\infty}^{\infty} e^{-i\omega\tau}\langle\{B(t), B(t+\tau)\}_{\pm}\rangle\, d\tau. \tag{1.10}$$

At thermal equilibrium, these spectra satisfy

$$S^{(-)}(\omega) = e^{-\hbar\omega/k_B T} S^{(+)}(\omega), \tag{1.11}$$

indicating that upward and downward transition rates differ according to the thermal occupation of the environment. This asymmetry becomes important at cryogenic temperatures or when probing the quantum backaction of a measurement apparatus.

1.2.5 Typical Spectral Forms of Noise

Different noise mechanisms correspond to distinct functional forms of the spectral density $S(\omega)$. In the *white-noise limit*, correlations decay instantaneously in time, producing a flat spectrum $S(\omega) = S_0$. This Markovian case yields simple exponential relaxation and dephasing, as described by the Lindblad master equation. At the opposite extreme, slow environmental fluc-

tuations produce *colored noise* with long correlation times. A widely observed example is $1/f$ *noise*, where

$$S(\omega) \propto \frac{1}{\omega^{\alpha}}, \qquad 0.5 \lesssim \alpha \lesssim 1.5. \tag{1.12}$$

This form arises from ensembles of slow fluctuators with a broad distribution of switching rates and dominates decoherence in many solid-state qubits, including superconducting and semiconductor platforms. In other cases, coupling to a discrete environmental mode of frequency ω_c and linewidth γ yields a *Lorentzian* spectrum,

$$S(\omega) = \frac{A\gamma^2}{(\omega - \omega_c)^2 + \gamma^2}, \tag{1.13}$$

revealing narrow-band noise sources such as nuclear spin precession or vibrational modes. Finally, *non-stationary* noise, where the spectrum itself changes in time, can occur due to slow drifts in material properties or charge rearrangements, producing temporally evolving decoherence behavior.

1.3 Quantum Noise Spectroscopy

While decoherence is typically viewed as a detrimental effect in quantum systems, it can also be exploited as a sensitive probe of environmental fluctuations. The central idea of *quantum noise spectroscopy* (QNS) is that the coherence decay of a well-controlled qubit contains information about the spectral density of its surrounding noise. By designing appropriate control sequences, one can shape the qubit's sensitivity to different frequency components of the noise, and thus reconstruct the underlying spectrum. This approach turns the qubit from a fragile

information carrier into a precision spectrometer for its own environment [19–24].

In essence, QNS establishes a quantitative relationship between the environmental power spectral density $S(\omega)$ and the qubit's coherence function $W(t) = e^{-\chi(t)}$, where the decay rate $\chi(t)$ depends on both $S(\omega)$ and a control-dependent *filter function* $F(\omega, t)$:

$$\chi(t) = \frac{1}{\pi} \int_0^\infty S(\omega) |F(\omega, t)|^2 \, d\omega. \tag{1.14}$$

This *filter-function formalism* provides the theoretical backbone of all noise-spectroscopy methods. Different control protocols correspond to different filter functions, enabling the selective sampling of distinct frequency bands of the noise spectrum.

1.3.1 The Filter-Function Formalism

To understand Eq. (1.14) in more detail, consider a qubit subjected to dephasing noise along the σ_z axis with a time-dependent control Hamiltonian $H_c(t) = \frac{1}{2}\hbar\Omega(t)\sigma_x$. In the toggling frame defined by this control, the instantaneous noise Hamiltonian is modulated by a switching function $y(t)$ that alternates between ± 1 depending on the applied pulses.

For stationary Gaussian noise, the dephasing exponent becomes

$$\chi(t) = \frac{1}{2} \int_0^t dt_1 \int_0^t dt_2 \, y(t_1) y(t_2) C(t_1 - t_2) = \frac{1}{\pi} \int_0^\infty S(\omega) |F(\omega, t)|^2 \, d\omega, \tag{1.15}$$

where $F(\omega, t)$ is the Fourier transform of the switching function:

$$F(\omega, t) = \int_0^t y(t') e^{i\omega t'} \, dt'. \tag{1.16}$$

Hence, by choosing $y(t)$ appropriately, one can tailor the spectral response of the qubit to specific frequency windows.

1.3.2 Ramsey and Hahn-Echo Spectroscopy

The simplest noise-spectroscopy experiments employ free evolution or a single refocusing pulse. In a Ramsey sequence, the qubit evolves freely for a duration τ between two $\pi/2$ pulses. The switching function is $y(t) = 1$ for $0 < t < \tau$, leading to a filter function

$$|F_{\text{Ramsey}}(\omega, \tau)|^2 = \frac{4\sin^2(\omega\tau/2)}{\omega^2}. \tag{1.17}$$

This filter strongly weights low-frequency noise, providing information about slow fluctuations and static disorder. Consequently, Ramsey interferometry is used to measure pure dephasing rates and low-frequency $1/f$ noise.

The Hahn-echo or spin-echo sequence adds a single π pulse at time $\tau/2$, which reverses the phase accumulated during the first half of the evolution. The resulting switching function alternates between $+1$ and -1, producing a filter

$$|F_{\text{Echo}}(\omega, \tau)|^2 = \frac{16\sin^4(\omega\tau/4)}{\omega^2}. \tag{1.18}$$

The echo filter suppresses slow fluctuations and enhances sensitivity to noise near frequencies $\omega \sim 2\pi/\tau$, providing improved coherence and frequency selectivity.

1.3.3 Robust and Composite Pulse Techniques

In real experiments, control pulses are never ideal: amplitude miscalibration, detuning, and finite pulse durations lead to systematic errors that can themselves mimic or obscure environmental noise. To ensure reliable noise spectroscopy, these imperfections must be mitigated through robust control design.

One broad class of techniques involves *composite pulses*, in which a logical rotation is implemented through a sequence of pulses with carefully chosen phases and durations that cancel first- or higher-order errors. Representative examples include the BB1, SK1, and CORPSE families [25, 26], which have been widely adopted in nuclear magnetic resonance and quantum information processing.

A simplest example is the robust $\pi\bar{\pi}$ *pair*: a π pulse immediately followed by an inverse $-\pi$ pulse with opposite phase. This pulse sequence suppresses the leading-order effects of rotation-angle and detuning errors.

1.4 Compressed sensing

In conventional signal processing, the Nyquist–Shannon sampling theorem [27, 28] establishes that a band-limited signal must be sampled at least twice its highest frequency component in order to be perfectly reconstructed. This principle has long dictated how scientists and engineers acquire and represent analog signals. However, the Nyquist limit can be prohibitively demanding when one wishes to capture high-resolution information or when data acquisition is intrinsically slow or costly. In many experimental settings—such as imaging, spectroscopy, or quantum measurement—the number of feasible samples is severely limited.

Yet, most real-world signals are not fully arbitrary. They often contain a high degree of redundancy, meaning that their essential information is concentrated in a few degrees of freedom while the rest carries little weight. A photographic image, for example, may consist primarily of large uniform regions separated by sharp edges; an audio signal is dominated by a few tones or harmonics; a noise spectrum might be characterized by a handful of resonant peaks atop a smooth background. These observations suggest that many signals possess an underlying simplicity or *sparsity*—that is, they can be represented by only a few nonzero coefficients in some appropriate basis.

The theory of *compressed sensing* (CS), developed by Emmanuel Candès, Terence Tao, and David Donoho, formalizes this intuition. It provides a rigorous framework for reconstructing sparse or compressible signals from far fewer measurements than traditional sampling theory would require. The landmark works by Candès, Romberg, and Tao [29, 30] demonstrated that exact signal recovery is possible from an undersampled dataset, provided that certain mathematical conditions on sparsity and measurement randomness are met. This discovery sparked a revolution in signal processing and has since influenced fields as diverse as medical imaging, astronomy, radar, and quantum physics [31–34].

1.4.1 The Basic Principle

At the heart of compressed sensing lies a simple mathematical model. Suppose we have an unknown signal $x \in \mathbb{R}^N$ that we wish to reconstruct from a set of linear measurements

$$y = Ax + \epsilon, \tag{1.19}$$

where A is an $M \times N$ measurement matrix with $M \ll N$, y is the measured data, and ϵ represents noise or experimental uncertainty. Because there are fewer equations than unknowns, this system is underdetermined and has infinitely many solutions. The key additional assumption is that x is *sparse*—it contains only $K \ll N$ nonzero components, or can be well approximated by such a vector.

If this sparsity assumption holds, the problem becomes one of identifying which few components of x are nonzero. In its idealized form, this can be written as a combinatorial optimization problem,

$$\min_x \|x\|_0 \quad \text{subject to} \quad y = Ax, \tag{1.20}$$

where $\|x\|_0$ counts the number of nonzero entries in x. However, directly minimizing the ℓ_0-norm is computationally infeasible for all but the smallest problems, since it requires checking all possible combinations of nonzero positions.

One of the central insights of compressed sensing is that the same sparse solution can be obtained by solving a much simpler convex optimization problem,

$$\min_x \|x\|_1 \quad \text{subject to} \quad y = Ax, \tag{1.21}$$

where $\|x\|_1 = \sum_i |x_i|$ is the ℓ_1-norm. This approach, known as *Basis Pursuit* [35], is computationally tractable and can be solved efficiently using standard convex optimization algorithms. The ℓ_1 norm acts as a convex surrogate for sparsity, penalizing the total magnitude of coefficients and naturally encouraging most of them to vanish. This remarkable equivalence between ℓ_0 and ℓ_1 optimization is one of the pillars of compressed sensing.

1.4.2 Measurement Design and Incoherence

A crucial factor determining the success of compressed sensing is the choice of the measurement matrix A. Not every measurement strategy allows sparse recovery; the measurements must contain enough independent information about the signal components. This requirement is captured by the concept of *incoherence* between the measurement basis and the sparsity basis. Intuitively, incoherence means that each measurement mixes together many components of the signal, so that information about any individual component is spread throughout the measurements.

Random matrices play a central role because they are almost always incoherent with any fixed basis. For example, matrices with entries drawn from Gaussian or Bernoulli distributions satisfy the necessary conditions for recovery with overwhelming probability. Similarly, randomly subsampled Fourier matrices also perform well. Randomness ensures that no measurement is overly aligned with the sparsity structure of the signal, thereby avoiding pathological cases of ambiguity.

1.4.3 Restricted Isometry Property and Recovery Guarantees

An important element of the theory of CS is the *Restricted Isometry Property* (RIP) introduced by Candès and Tao [36]. A matrix A satisfies the RIP of order K if it approximately preserves the lengths of all K-sparse vectors:

$$(1 - \delta_K)\|x\|_2^2 \leq \|Ax\|_2^2 \leq (1 + \delta_K)\|x\|_2^2 \tag{1.22}$$

for all x with at most K nonzero elements, where δ_K is a small constant. Intuitively, this means that every subset of K columns of A behaves almost like an orthonormal system. If δ_{2K} is sufficiently small (for instance, less than $\sqrt{2}-1$), then exact recovery of all K-sparse signals via ℓ_1-minimization is guaranteed. Furthermore, this recovery is stable even when the measurements are contaminated with noise (e.g., small additive errors).

A remarkable result is that random Gaussian or Bernoulli matrices satisfy the RIP with high probability provided that the number of measurements scales as $M \gtrsim K \log(N/K)$ [37]. This scaling, far smaller than the classical Nyquist limit ($M \sim N$), is what makes compressed sensing so powerful. It formally establishes that accurate reconstruction is possible with only a logarithmic oversampling factor above the number of degrees of freedom in the signal.

1.4.4 Algorithms for Realistic Signals

Several algorithmic families have been developed for solving compressed sensing problems, each suited to different experimental and computational contexts. The original convex approach, Basis Pursuit, remains the most theoretically clean but can be computationally intensive for large systems. For example, in real physical systems, the noise spectra are usually not ideally sparse. We may adopt suitable data analysis techniques to better process compressed sensing. For example, we can apply the LASSO (least absolute shrinkage and selection) algorithm [38, 39], which solves the following problem,

$$\begin{gathered} \text{find } x \in \mathbb{R}^N \text{ that minimize} \\ \tfrac{1}{2}||y^T - Ax^T||_{L2}^2 + \lambda||x||_{L1}. \end{gathered} \tag{1.23}$$

This can be viewed as a Lagrangian relaxation of Eq. (1.21), which is useful when one is given data y that contain noise or errors. The coefficient λ controls the relative strength between the two parts in Eq. (1.23). In general, when the noise is strong, one need a larger λ to ensure the L_1 regularization term still matters. Meanwhile, λ cannot be too large; otherwise, the result will be too biased. Here, we use the cross-validation (CV) method to establish the value of λ.

1.4.5 Extensions Beyond Classical Sparsity

The notion of sparsity can be extended beyond the simple idea of having only a few nonzero coefficients [40]. Many real-world signals and datasets exhibit more complex but still low-dimensional structures. Two particularly important generalizations are *total variation (TV) minimization* [41–44] and *low-rank matrix recovery* [45–47].

In total variation minimization, sparsity is promoted not in the signal itself but in its discrete gradient. For a one-dimensional signal $x \in \mathbb{R}^N$, the discrete difference operator D is defined by

$$(Dx)_i = x_{i+1} - x_i, \tag{1.24}$$

and the total variation norm is given by

$$\|x\|_{\mathrm{TV}} = \|Dx\|_1 = \sum_{i=1}^{N-1} |x_{i+1} - x_i|. \tag{1.25}$$

The corresponding optimization problem,

$$\min_x \|Dx\|_1 \quad \text{subject to} \quad y = Ax, \tag{1.26}$$

promotes solutions that are *piecewise constant or piecewise smooth*, since only a few discrete derivatives are nonzero. (Note that the equality constraint $y = Ax$ can be relaxed, analogously to Eq. (1.23), to allow for the possibility that the measurements y contain small additive errors.) This formulation effectively penalizes rapid changes while preserving sharp edges, making it particularly useful in image denoising and reconstruction problems [48]. More generally, higher-order difference operators such as D^2 or D^k can be used to encourage *piecewise polynomial* behavior, forming the basis of higher-order trend filtering and total generalized variation (TGV) methods.

When data are naturally represented as matrices, another kind of low-dimensional structure arises: *low rank*. A matrix $X \in \mathbb{R}^{m\times n}$ is said to be low rank if its number of nonzero singular values, $\mathrm{rank}(X)$, is much smaller than $\min(m, n)$. Recovering such a matrix from incomplete or noisy linear measurements $y = \mathcal{A}(X)$ can be formulated as

$$\min_X \mathrm{rank}(X) \quad \text{subject to} \quad y = \mathcal{A}(X), \tag{1.27}$$

which, like the ℓ_0-minimization problem in classical compressed sensing, is combinatorial and computationally intractable. A convex relaxation replaces the rank function with the *nuclear norm*,

$$\|X\|_* = \sum_i \sigma_i(X), \tag{1.28}$$

the sum of the singular values of X. The resulting problem,

$$\min_X \|X\|_* \quad \text{subject to} \quad y = \mathcal{A}(X), \tag{1.29}$$

is known as *nuclear-norm minimization* or *matrix completion*, and it can be solved efficiently by convex optimization [49]. (As noted previously, the equality constraint $y = \mathcal{A}(X)$ can be relaxed, analogously to Eq. (1.23), in case the measurements y contain additive errors.) Under appropriate incoherence and sampling conditions, this formulation exactly recovers the low-rank matrix from a small number of measurements, with guarantees closely analogous to the sparsity-based results of classical compressed sensing.

Both total variation and low-rank recovery exemplify a broader principle: the success of compressed sensing does not depend solely on literal sparsity, but on exploiting any intrinsic low-dimensional structure in the data. By choosing an appropriate regularizer—ℓ_1, total variation, nuclear norm, or others—one can efficiently recover signals, images, or operators that reside on low-complexity manifolds within a high-dimensional ambient space [32, 40, 50].

1.5 Outline of the Thesis

The remainder of this thesis is organized as follows:

- Chapter 2: "Random Pulse Sequences" presents a general framework for the random pulse sequences method with broad applicability. We show that phase retrieval techniques can be used to design pulse sequences for measuring any desired linear functional of $S(\omega)$. We analyze the accuracy of the method and establish a rigorous error bound. We then show a simple application of the method to learn 1-D chain representations of open quantum systems.

- Chapter 3: "Compressed Sensing with Random Pulses" makes use of the framework developed in Chapter 2. We demonstrate the efficient reconstruction of sparse spectra us-

ing a combination of random pulse sequences, and techniques from compressed sensing. We further apply this method to realistic physical platforms, including quantum dots, and commercially-available quantum information processors based on superconducting and trapped ions qubits.

- Chapter 4: "Piecewise Linear Modeling and Rademacher Measurements" advances the general random pulse sequences method in two complementary directions. We extend the method to reconstructing piecewise-linear noise spectra. We also introduce a simplified variant using Rademacher measuremtns, optimized for sparse spectra. We showcase the efficiency of these improvements through numerical simulations on both idealized and realistic physical systems.

Chapter 2: Random Pulse Sequences

2.1 Introduction

Noise spectroscopy is an essential tool for understanding the behavior of a quantum system coupled to an environment. It plays an important role in the experimental investigation of quantum computation and quantum sensing, in physical systems such as superconducting qubits, semiconductor quantum dots, and nitrogen-vacancy centers in diamond [7, 21, 51–55]. Typically, noise spectroscopy consists of estimating the noise spectral density, $S(\omega)$, at many different frequencies ω, using techniques such as relaxometry or dynamical decoupling [24, 56–60].

Dynamical decoupling (DD) pulse sequences have been studied for decades in the field of nuclear magnetic resonance (NMR) to reduce the dephasing of spin ensembles [61, 62], and later implemented in various quantum systems for noise spectroscopy [20–24]. The rotation π-pulses incorporated in these sequences shape the filter function that probes the qubit's environment in the frequency domain. However, this requires the application of many pulse sequences to learn $S(\omega)$ across the whole frequency domain, and is thus quite time-consuming. This problem is exacerbated when one performs multi-qubit noise spectroscopy on systems with many qubits, which are relevant to many promising applications of quantum technologies [59, 63].

In this chapter, we develop a different approach to performing noise spectroscopy, which requires fewer resources, and relies on direct measurement of arbitrary linear functionals of the

noise spectral density $S(\omega)$. This can be used to estimate physically-relevant properties of $S(\omega)$, *without* needing to completely characterize $S(\omega)$. Some properties of $S(\omega)$ that can be measured in this way include: the total noise strength, which can be used to detect changes in the environment of the qubit in real time; inner products between $S(\omega)$ and sinusoidal functions, which are useful for compressed sensing of $S(\omega)$ (described later in this work).

Our approach applies $\pi-$pulses at random timings with carefully-chosen correlations (i.e., random pulse sequences). These random pulse sequences are generated using finite impulse response (FIR) filters, in a way that is simple enough to be implemented in many experimental setups. The design of these FIR filters relies on computational methods for *phase retrieval*, which is the task of estimating a function, given measurements of the (squared) absolute value of its Fourier transform [64]. Algorithms for phase retrieval have a long history of use for image reconstruction in astronomy, crystallography and other fields. Our use of phase retrieval, for sensing in the time and frequency domains, is relatively unusual.

The first main result of this chapter is to show that phase retrieval techniques can be used to design FIR filters for measuring any desired linear functional of $S(\omega)$, subject to some mild admissibility conditions. In addition, we show that the statistical fluctuations in these measurements, due to the random choice of the pulse sequence, become small as one increases the number of pulses M. More precisely, we show that the magnitude of these fluctuations is of order $1/\sqrt{M}$, relative to the expectation value of the measurement.

These results can be compared with other recent works on generating or simulating noise with prescribed time-correlations that are much slower than the system dynamics [65–68]. Our goal in this work is different, however: we use random pulse sequences to measure properties of the noise generated by an unknown environment, rather than to simulate or model a source of

noise that has already been characterized by some other kind of measurement.

We then demonstrate the use of the random pulse sequences method to learn 1-D chain representations of open quantum systems [69], demonstrating their power to efficiently probe open system dynamics.

2.2 Noise Model

Let us consider a single qubit ("the system") coupled to a classical bath that leads to pure dephasing of the qubit. The general Hamiltonian can be written as

$$\hat{H}(t) = \hat{H}_0 + \hat{H}_V(t) = (\Omega + V(t))\sigma_z, \tag{2.1}$$

where $\hat{H}_0 = \Omega\sigma_z$ is the system Hamiltonian and $\hat{H}_V(t)$ is the Hamiltonian associated with a stochastic process $V(t)$ that describes the noise caused by the bath. For example, $V(t)$ can represent a classical fluctuating variable, such as a magnetic field. For simplicity, here we assume that $V(t)$ is a Gaussian process with zero mean value

$$\langle V(t)\rangle_V = 0, \tag{2.2}$$

where $\langle ...\rangle_V$ stands for the average with respect to the ensemble of $V(t)$. The Gaussian process is determined by the auto-correlation

$$\langle V(t)V(t')\rangle_V = g(t-t'). \tag{2.3}$$

In the frequency domain, the spectral density can be defined by the Fourier transform of the auto-correlation,

$$S(\omega) = \int_{-\infty}^{+\infty} e^{-i\omega t} g(t) dt. \tag{2.4}$$

The dynamics of a system coupled to a Gaussian bath can be entirely determined by the spectrum, $S(\omega)$ [18, 70].

In this work, we make an additional assumption that the noise spectrum vanishes at frequencies larger than a cutoff frequency ω_c, that is, $S(\omega) = 0$ when $|\omega| > \omega_c$ [9, 71]. This frequency ω_c is also referred as 'ultraviolet cutoff' for Ohmic spectra and many $1/f$ spectra [72, 73]. We assume that the experimentalist has access to sufficiently fast controls, to probe the noise spectrum up to this cutoff frequency.

The methods for noise spectroscopy described in this work can also be extended to characterize quantum environments, such as bosonic baths [74]. For example, in the spin-boson model [10, 75, 76], the system qubit is weakly coupled with many harmonic oscillators. The bath Hamiltonian and the coupling between system and bath can be written as

$$\hat{H}_B + \hat{H}_V = \sum_k \omega_k a_k^\dagger a_k - \frac{1}{2} \sum_k (g_k a_k + g_k^* a_k^\dagger) \sigma_z, \tag{2.5}$$

where $\hat{H}_B, \hat{H}_V$ are the bath and interacting Hamiltonian, $a_k (a_k^\dagger)$ is the kth mode annihilation (creation) operator of the bath, and g_k is the coupling strength between kth mode and the qubit. The sum over k can be approximated by the frequency integral

$$\sum_k |g_k|^2 \approx \int_0^\infty S(\omega) d\omega, \tag{2.6}$$

where $S(\omega)$ is the spectral function of the bath. When the bath is in thermal equilibrium at inverse temperature β, the noise spectrum can be calculated as

$$S(\omega) = \begin{cases} \pi S(\omega)(\coth(\beta\omega/2) + 1), \omega > 0, \\ \pi J(-\omega)(\coth(-\beta\omega/2) - 1), \omega < 0. \end{cases} \tag{2.7}$$

Unlike a classical bath, the spectrum $S(\omega)$of the bosonic bath contains "classical parts" and "quantum parts" [59],

$$\begin{aligned} S^+(\omega) &= (S(\omega) + S(-\omega))/2, \\ S^-(\omega) &= (S(\omega) - S(-\omega))/2. \end{aligned} \tag{2.8}$$

The "quantum part," $S^-(\omega)$, is nonzero only when the bath is quantum. However, we are only able to characterize the "classical parts" using the spectroscopy method we discussed in this work, as the decay rate only depends on $S^+(\omega)$,

$$\chi(T) = \int_{-\infty}^{\infty} \frac{d\omega}{2\pi} S^+(\omega) W(\omega). \tag{2.9}$$

This brings difficulty to fully characterize $S(\omega)$. For example, suppose we are interested in measuring a linear functional $I = \int_{-\omega_c}^{\omega_c} S(\omega)T(\omega)d\omega$, where the target function $T(\omega)$ is not an even function of ω. We may as well define the even and odd parts of $T(\omega)$ in the following way,

$$\begin{aligned} T^+(\omega) &= (T(\omega) + T(-\omega))/2, \\ T^-(\omega) &= (T(\omega) - T(-\omega))/2. \end{aligned} \tag{2.10}$$

The noise spectroscopy method only allows us to probe $I^+ = \int_{-\omega_c}^{\omega_c} S^+(\omega)T^+(\omega)d\omega$, while the

information about the quantum part, $I^- = \int_{-\omega_c}^{\omega_c} S^-(\omega)T^-(\omega)d\omega$, is missing. However, when the bath is at thermal equilibrium, this difficulty can be circumvented by observing that

$$S^-(\omega) = S^+(\omega)\tanh(\beta\omega/2). \tag{2.11}$$

Thus, if we know the inverse temperature β, we can set up a new target function $T^*(\omega)$ that is always even on ω,

$$T^*(\omega) = T^+(\omega) + T^-(\omega)\tanh(\beta\omega/2). \tag{2.12}$$

Then, we can then use the random pulse method to measure the following linear functional

$$\begin{aligned} I^* &= \int_{-\omega_c}^{\omega_c} S(\omega)T^*(\omega)d\omega \\ &= \int_{-\omega_c}^{\omega_c} S^+(\omega)T^+(\omega)d\omega + \int_{-\omega_c}^{\omega_c} S^+(\omega)\tanh(\beta\omega/2)\cdot T^-(\omega)d\omega \\ &= \int_{-\omega_c}^{\omega_c} S^+(\omega)T^+(\omega)d\omega + \int_{-\omega_c}^{\omega_c} S^-(\omega)T^-(\omega)d\omega \\ &= \int_{-\omega_c}^{\omega_c} S(\omega)T(\omega)d\omega = I. \end{aligned} \tag{2.13}$$

That is to say, we can fully characterize the spectrum of a quantum spin-boson model in thermal equilibrium, provided we know the temperature of the bath.

2.3 Protocols for noise spectroscopy

As illustrated by Fig. 2.1, a general protocol for noise spectroscopy goes as follows: (1) Prepare the system qubit in the $|+\rangle = \frac{1}{\sqrt{2}}(|0\rangle + |1\rangle)$ state using a Hadamard gate. (2) Apply a sequence of π pulses, of total time duration T. (3) Rotate the qubit back with a Hadamard gate

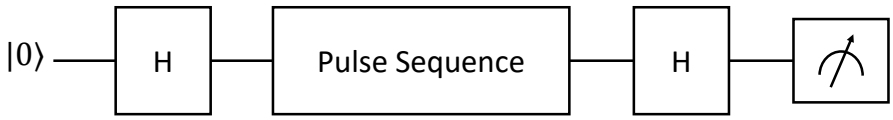


Figure 2.1: A single-qubit noise spectroscopy experiment. The qubit is initialized in the $|+\rangle$ state by a Hadamard gate. Then, the qubit evolves under the application of the pulse sequence. Finally, a measurement is performed in the σ_z basis after another Hadamard gate.

and measure its state in the σ_z basis. (4) Repeat (1)-(3) many times and estimate the probability, $P_0(T)$, to obtain the qubit in the $|0\rangle$ state.

For a stochastic bath, $P_0(T)$ yields an exponential decay, $e^{-\chi(T)}$, which only depends on $S(\omega)$ and the pulse sequence [72, 77, 78],

$$\begin{aligned} P_0(T) &= \tfrac{1}{2}(1 + e^{-\chi(T)}), \\ \chi(T) &= \int_{-\infty}^{\infty} \frac{d\omega}{2\pi} S(\omega)|\tilde{f}(\omega)|^2 = \int_{-\infty}^{\infty} \frac{d\omega}{2\pi} S(\omega)W(\omega), \end{aligned} \tag{2.14}$$

where $f(t)$ is the filter function corresponding to the pulse sequence (see Fig. 2.2), $\tilde{f}(\omega)$ is the Fourier transform of the filter function, and the window function, $W(\omega)$, is defined as $W(\omega) = |\tilde{f}(\omega)|^2$. Note that $f(t)$, $\tilde{f}(\omega)$ and $W(\omega)$ all depend implicitly on the total evolution time T.

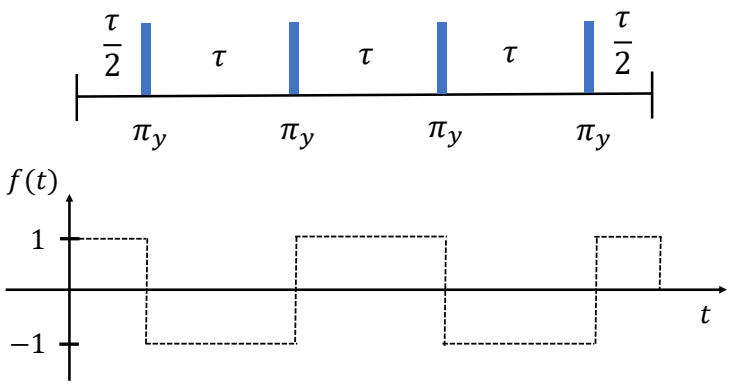


Figure 2.2: Top: An illustration of the CPMG pulse sequence with $M = 4$ instantaneous π-pulses (blue rectangles) along the y axis. The time interval between each two pulses is $\tau = T/M$. The qubit freely evolves for a time of $\tau/2$ before the first pulse and after the last one. Bottom: The corresponding filter function, $f(t)$, flips the sign every time a π-pulse is applied.

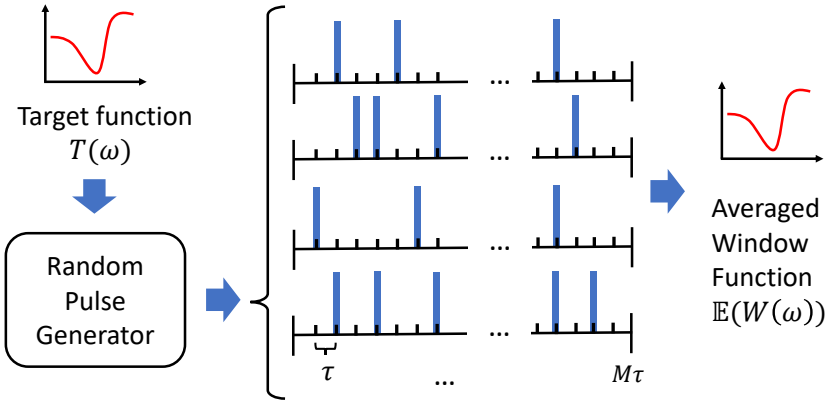


Figure 2.3: Illustration of the random pulse sequence method. Given a target function, $T(\omega)$, a random pulse generator can produce multiple pulse sequences. The blue spikes represent instantaneous π-pulses. The expectation value of the resulting window function, $\mathbb{E}(W(\omega))$, approximates $T(\omega)$. As a result, one can measure the linear functional $\int S(\omega)T(\omega)d\omega$ by averaging the outcome of each individual pulse sequence.

2.3.1 Dynamical decoupling

Here we review the Carr-Purcell-Meiboom-Gill (CPMG) pulse sequence as the typical DD method used for noise spectroscopy [19–23, 61, 79, 80]. The CPMG pulse sequence (illustrated by Fig. 2.2) consists of M rotation π-pulses applied with time period τ ($\tau = T/M$). The window function of this sequence equals

$$W(\omega) = \begin{cases} \frac{32}{\omega^2}\sin^4(\frac{\omega\tau}{4})\sin^2(\frac{\omega M\tau}{2})/\cos^2(\frac{\omega\tau}{2}), \text{for even } M \\ \\ \frac{32}{\omega^2}\sin^4(\frac{\omega\tau}{4})\cos^2(\frac{\omega M\tau}{2})/\cos^2(\frac{\omega\tau}{2}), \text{for odd } M. \end{cases} \tag{2.15}$$

When M is large, $W(\omega)$ can be approximated as a Dirac $\delta-$function located at $\omega = \frac{\pi}{2}\tau$. As a result, the application of a CPMG sequence mainly probes the noise at a single frequency of $\frac{\pi}{2}\tau$. However, the exact window functions in Eq. (2.15) deviate from Dirac $\delta-$functions and include higher harmonics. A commonly used technique to deal with deviations is the Alvarez-Suter method [56, 81, 82], which applies a comb approximation to the window function when M approaches infinity.

In this work, we apply a deconvolution procedure to correct for the deviations without any assumption on M. This window function contains one major peak, at $\omega_0 \approx \frac{\pi}{2}\tau$, and multiple minor peaks at higher harmonics. The reconstructed spectrum $S(\omega)$ from the decoherence data is a solution to the Fredholm type equation

$$\chi(T) = \int_{-\infty}^{\infty} \frac{d\omega}{2\pi} S(\omega)W(\omega). \tag{2.16}$$

Since we assume that the spectrum decays to zero at high frequency, we can reconstruct the spec-

trum from higher to lower frequencies by subtracting the effect of higher harmonics recursively using the analytical form of $W(\omega)$ in Eq. (2.15).

The detailed algorithm goes in the following way: We first approximate the spectrum from the main contribution of the decay exponent due to the major peak,

$$\begin{aligned}\chi(T) &\approx \int_{\omega_-}^{\omega_+} \frac{d\omega}{2\pi} S(\omega) W(\omega) \\ &\approx \frac{S(\omega_0)}{2\pi} \int_{\omega_-}^{\omega_+} d\omega W(\omega) \\ &\approx \frac{S(\omega_0)}{2\pi} \Sigma,\end{aligned} \tag{2.17}$$

where Σ is the area under the major peak, defined as the integral of $W(\omega)$ between the nearest two local minima ω_- and ω_+ around ω_0. Thus we get the first-order approximation of the spectrum,

$$S_1(\omega_0) \approx \frac{2\pi\chi(T)}{\Sigma}. \tag{2.18}$$

We then apply different CPMG sequences to sample the spectrum at various frequencies. We sort all sampled frequencies from highest to lowest, and label them as $[\omega_0^1, \omega_0^2, \ldots, \omega_0^{\max}]$. The corresponding window functions are labelled as $[W^1(\omega), W^2(\omega), \ldots, W^{\max(\omega)}]$. Assuming that the noise spectrum vanishes above the highest sampled frequency, $\omega_{\max}$, expression (2.18) is exact such that $S(\omega_0^{\max}) = S_1(\omega_0^{\max})$. Next we can iteratively calculate the spectrum from the highest frequency downwards,

$$S(\omega_0^i) = S_1(\omega_0^i) - \int_{\omega_+^i}^{\infty} \frac{d\omega}{2\pi} S^*(\omega) W^i(\omega), \tag{2.19}$$

where $S^*(\omega)$ takes the value of the previously (recursively) extracted spectrum at the sampled

frequency closest to ω.

Another commonly applied reconstruction method for noise spectroscopy is the Alvarez-Suter method [56], which requires the assumption of an infinite number of pulses to justify the comb approximation. Compared to that, the decomposition method mentioned above utilize the exact form of the window function, and in general works better for the spectra decaying to zero at high frequency [21, 81, 82].

To fully decompose the spectrum then requires sweeping the free evolution time, τ (or the number of pulses, M). However, such probing across the whole frequency range involves numerous measurements, which are not always necessary for extracting the significant features of the noise.

2.4 Random pulse sequences

We propose an alternative method for noise spectroscopy based on random pulse sequences. Rather than probing single frequencies like the CPMG method, our approach generates window functions, $W(\omega)$, that approximate a desired spectral shape $T(\omega)$. The general idea is to design a *random* pulse generator to produce a group of sequences, such that the expectation value of their window function, $\mathbb{E}(W(\omega))$, can approximate the desired target function, $T(\omega)$, as illustrated in Fig. 2.3. As a result, we can directly estimate the linear functional, $I = \int S(\omega)T(\omega)d\omega$. This procedure is analogous to the generation of a stationary sequence [83], adapted for noise spectroscopy.

The random pulse sequences are generated in the following way. The total experiment time, T, is divided into M equal segments, such that $T = M\tau$. Rotation π-pulses are applied

only at the end of particular segments determined by a random pulse generator. Specifically, we generate a vector of random variables, $\vec{U} = (U_1, \ldots, U_M) \in \{1, -1\}^M$, and a corresponding random pulse sequence, such that:

1. U_i represents the value of the filter function, $f(t)$, in the time segment $t \in [(i-1)\tau, i\tau]$. A π-pulse is applied at time $i\tau$ if and only if $U_i \neq U_{i+1}$.

2. The expectation value of any random variable is zero, i.e., $\mathbb{E}(U_i) = 0$.

3. The covariance of two random variables, U_i, U_j, should only depend on the distance $|j-i|$, i.e., it has the form $\mathbb{E}(U_i U_{i+j}) = R(j)$ (for $j \geq 1$).

Random variables U_i satisfying these properties can be constructed by generating a sequence of independent Gaussian random variables $N_0, N_1, N_2, \ldots$, applying a finite impulse response (FIR) filter with suitably chosen coefficients $(a_0, a_1, \ldots, a_{\lambda-1})$, and then applying the sign function to obtain:

$$U_i = \text{sign}(\sum_{j=0}^{\lambda-1} a_j N_{i+j}), \quad i = 0, 1, 2, \ldots. \tag{2.20}$$

Without loss of generality, we can extend the FIR coefficients to a normalized M dimensional vector $\vec{V}_m = (0, 0, \ldots, a_0, a_1, \ldots, a_{\lambda-1}, 0, \ldots, 0)$ where a_0 appears in position m, so that $U_m = \text{sign}(\vec{V}_m \vec{N}^T)$ and $\vec{V}_m \vec{V}_m^T = 1$. Furthermore, the whole construction process can also be viewed geometrically as a hyper-plane tessellation, see Fig. 2.4. $\vec{V}_m$ is the normal vector of a hyper-plane in $\mathbb{R}^M$ which divides the entire space into two regions. The value of U_m is determined by whether the random vector $\vec{N}$ lies within the corresponding region. The covariance $R(k)$ between U_m and

U_{m+k} (for $k \geq 1$) can thus be calculated using the angle between different hyper-planes:

$$\begin{aligned} R(k) &= \mathbb{E}(U_{m+k}U_m) \\ &= P(U_m \neq U_{m+k}) \cdot (-1) + P(U_m = U_{m+k}) \cdot (+1) \\ &= \frac{\arccos\left(\frac{\vec{V}_m \vec{V}_{m+k}^T}{|\vec{V}_m||\vec{V}_{m+k}|}\right)}{\pi} \cdot (-1) + \frac{(\pi - \arccos\left(\frac{\vec{V}_m \vec{V}_{m+k}^T}{|\vec{V}_n||\vec{V}_{m+k}|}\right)}{\pi} \cdot (+1) \\ &= \frac{2}{\pi}\arcsin\left(\vec{V}_n \vec{V}_{n+k}^T\right) = \frac{2}{\pi}\arcsin\left(\sum_{i=0}^{\lambda-1-k} a_i a_{i+k}\right). \end{aligned} \tag{2.21}$$

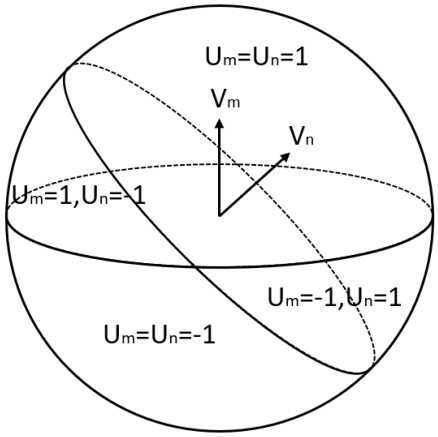


Figure 2.4: A geometric interpretation of how to generate the random pulse sequences, $\vec{U}$, by hyper-plane tessellation. The space is separated by hyper-planes with normal vectors indicated by the FIR coefficients, $\vec{V}_m$. Every time we generate a Gaussian random sequence $\vec{N}$, we can calculate $\vec{U}$ by checking which region $\vec{N}$ lies in after the tessellation. For example, if $\vec{N}$ lies in the right upper corner of the hyper sphere we show, then $U_m = U_n = 1$. Since the elements in $\vec{N}$ are independent Gaussian random variables, $\vec{N}$ is uniformly distributed over all directions. Thus, the covariance between different U_m can be calculated by the solid angles between these hyper-planes.

Next, we can calculate the expectation value of the window function generated by the random pulse sequences. Recall that the decay exponent equals

$$\chi_U(T) = \frac{1}{2\pi}\int_{\pi/\tau}^{\pi/\tau} d\omega S(\omega)W(\omega), \tag{2.22}$$

with

$$W_U(\omega) = \left|\tilde{f}_U(\omega)\right|^2, \tag{2.23}$$

$$\tilde{f}_U(\omega) = \int_{-\infty}^{\infty} dt f_U(t) e^{i\omega t}, \tag{2.24}$$

$$f_U(t) = \begin{cases} U_m & \text{if } t \in [(m-1)\tau, m\tau),\, m \in \{1, 2, \ldots, M\}, \\ 0 & \text{otherwise.} \end{cases} \tag{2.25}$$

Hence we have

$$\begin{aligned} W(\omega) &= \left|\tilde{f}_U(\omega)\right|^2 \\ &= \tau^2 \operatorname{sinc}^2(\tfrac{\omega\tau}{2}) \left|\sum_{m=1}^{M} U_m e^{i\omega m\tau}\right|^2 \\ &= \tau^2 \operatorname{sinc}^2(\tfrac{\omega\tau}{2}) \vec{U}^T A(\omega) \vec{U}, \end{aligned} \tag{2.26}$$

where we define the matrix $A(\omega) \in \mathbb{C}^{M\times M}$ whose (m, m') entry is

$$A_{m,m'}(\omega) = e^{i\omega(m-m')\tau}. \tag{2.27}$$

We can further define the matrix $B(S) \in \mathbb{C}^{M\times M}$ whose (m, m') entry is

$$B_{m,m'}(S) = \hat{S}_{m-m'} \equiv \int_{-\pi/\tau}^{\pi/\tau} d\omega S(\omega) \operatorname{sinc}^2(\tfrac{\omega\tau}{2}) A_{m,m'}(\omega) \tag{2.28}$$

where $\hat{S}_{m-m'}$ is equal to the $(m-m')$'th coefficient of the Fourier series expansion of $S(\omega)\operatorname{sinc}^2(\frac{\omega\tau}{2})$.

Thus we can write χ_U in the following form:

$$\chi_U = \frac{\tau^2}{2\pi}\vec{U}^T B(S)\vec{U}, \tag{2.29}$$

Therefore, the expectation value of $W(\omega)$ is

$$\begin{aligned}\mathbb{E}(W(\omega)) &= \tau^2 \operatorname{sinc}^2(\tfrac{\omega\tau}{2})\, \mathbb{E}(\vec{U}^T A(\omega)\vec{U}) \\ &= \tau^2 \operatorname{sinc}^2(\tfrac{\omega\tau}{2}) \sum_{m,m'} (\mathbb{E}(U_m U_{m'}) A_{m,m'}(\omega)) \\ &= M\tau^2 \operatorname{sinc}^2(\tfrac{\omega\tau}{2})[1 + 2\sum_{k=1}^{\lambda} R(k)\cos(k\omega\tau)(1 - \tfrac{k}{M})].\end{aligned} \tag{2.30}$$

The expectation value of $\chi_U(T)$ is

$$\mathbb{E}(\chi_U(T)) = \frac{M\tau^2}{2\pi}\int_{-\omega_c}^{\omega_c} d\omega S(\omega) \operatorname{sinc}^2(\tfrac{\omega\tau}{2})[1 + 2\sum_{k=1}^{\lambda} R(k)\cos(k\omega\tau)(1 - \tfrac{k}{M})] \tag{2.31}$$

In some cases, time-varying FIR filters may be used for improved computational efficiency (see Appendix 2.8).

The above construction is related to the phase retrieval problem, in the following way. We can see from Eq. (2.21) that the correlations $R(k)$ in the random pulse sequence are related to the autocorrelation function of the filter coefficients a_i. One can interpret the a_i as Fourier coefficients of some periodic function on the real line:

$$b(m) = \sum_{j=0}^{\lambda-1} a_j e^{-j\frac{2\pi i m}{2\lambda-1}}. \tag{2.32}$$

Then the $R(k)$ can be rewritten in terms of $|b(m)|^2$, i.e., they encode information about the

magnitudes, but not the complex phases, of the function $b(m)$. This is analogous to a phase retrieval problem.

Now, given some desired correlations $\tilde{R}(k)$, let our goal be to choose filter coefficients a_i that will generate random variables U_i whose correlations $R(k)$ approximately match the $\tilde{R}(k)$. We will do this using phase retrieval techniques, in the following way. We interpret the $\tilde{R}(k)$ as "noisy" measurements of $|b(m)|^2$, where the "noise" is due to the fact that the desired correlations $\tilde{R}(k)$ may not be exactly realizable by a stochastic process of the form (2.20). We then use algorithms for phase retrieval to learn a function $b(m)$ such that $|b(m)|^2$ is approximately compatible with the desired correlations $\tilde{R}(k)$. From $b(m)$ we finally obtain the corresponding filter coefficients a_i.

Assuming that the $\tilde{R}(k)$ satisfy some mild admissibility conditions, the above phase retrieval problem is guaranteed to have a feasible solution, due to the Fejér-Riesz theorem [84, 85]. In practice, solutions can be found using gradient descent methods, or the Gerchberg-Saxton (GS) algorithm [64]. See section 2.5 for details.

2.5 Approximating a desired window function

Recall from Section 2.4 that our goal is to ensure that the averaged window function $\mathbb{E}(W(\omega))$ approximates some prescribed target function $T(\omega)$. Note that the cosine functions $\{\cos(k\omega\tau)\}$ form an almost complete basis (the zeroth term excluded) in the region $[-\frac{\pi}{\tau}, \frac{\pi}{\tau}]$. Thus we take the following approach: we match the time interval between segments and the cut-off frequency of the noise (i.e., setting $\tau = \frac{\pi}{\omega_c}$), and we adjust the random pulse generator (i.e.,

optimizing the filter coefficients $(a_0, a_1, \ldots, a_{\lambda-1})$), so that

$$R(k) = \frac{M}{\pi(M-k)} \int_{-\omega_c}^{\omega_c} \frac{cT(\omega)\cos(k\omega\tau)}{\operatorname{sinc}^2(\frac{\omega\tau}{2})} d\omega \quad (\forall k = 1, \ldots, \lambda), \tag{2.33}$$

which implies

$$\mathbb{E}(W(\omega)) \xrightarrow{\lambda\to\infty} M\tau^2[cT(\omega) + (1 - cT_0)\operatorname{sinc}^2(\tfrac{\omega\tau}{2})]. \tag{2.34}$$

Here c is an adjustable parameter that ensures the positivity of $W(\omega)$, and T_0 is a constant term depending on $T(\omega)$,

$$T_0 = \frac{1}{\omega_c} \int_{-\omega_c}^{\omega_c} \frac{T(\omega)}{\operatorname{sinc}^2(\frac{\omega\tau}{2})} d\omega. \tag{2.35}$$

Combining equations (2.21) and (2.33), we finally get an equation to generate the filter coefficients:

$$\sum_{i=0}^{\lambda-1-k} a_i a_{i+k} = \sin\left(\frac{\pi}{2} R(k)\right) = \sin\left(\frac{M}{2(M-k)} \int_{-\omega_c}^{\omega_c} \frac{cT(\omega)\cos(k\omega\tau)}{\operatorname{sinc}^2(\frac{\omega\tau}{2})} d\omega\right) \quad (\forall k = 1, \ldots, \lambda). \tag{2.36}$$

Note that the left side of this equation can be seen as the autocorrelation of a sequence formed by a_i, so solving for the values of a_i is equivalent to a 1-dimensional discrete phase retrieval problem [64]. This can be solved by switching to the Fourier domain, as follows.

Define $R(k)$ for all integers k, by defining $R(0) = 1$ and $R(k) = R(-k)$. We define $q(m)$ to be a periodic function on the real line, with $q(m) = q(m + 2\lambda - 1)$, whose Fourier coefficients are $\sin\left(\frac{M}{2(M-k)} \int_{-\omega_c}^{\omega_c} \frac{cT(\omega)\cos(k\omega\tau)}{\operatorname{sinc}^2(\frac{\omega\tau}{2})} d\omega\right)$:

$$q(m) = \sum_{k=-(\lambda-1)}^{\lambda-1} \sin\left(\frac{M}{2(M-k)} \int_{-\omega_c}^{\omega_c} \frac{cT(\omega)\cos(k\omega\tau)}{\operatorname{sinc}^2(\frac{\omega\tau}{2})} d\omega\right) e^{-k\frac{2\pi i m}{2\lambda-1}}. \tag{2.37}$$

Next, we define $b(m)$ to be a periodic function on the real line, with $b(m) = b(m + 2\lambda - 1)$, as follows:

$$b(m) = \sum_{j=0}^{\lambda-1} a_j e^{-j\frac{2\pi i m}{2\lambda-1}} \tag{2.38}$$

Then equation (2.36) becomes:

$$q(m) = |b(m)|^2, \quad \forall m \in \mathbb{R}. \tag{2.39}$$

That is, given a function $q(m)$ (which is defined by (2.37)), we want to solve for a function $b(m)$ that has the form (2.38). Note that m can take arbitrary real values.

When $q(m)$ is non-negative, the existence of solutions to Eq. (2.39) can be guaranteed by the well-known Fejér-Riesz theorem [84, 85]:

Theorem 1 *(Fejér-Riesz) If*

$$Y(e^{it}) = \sum_{n=-M}^{M} y(n) e^{-int} \tag{2.40}$$

and assumes non-negative real values for all real t, then there is a polynomial

$$X(z) = \sum_{n=0}^{M} x(n) z^{-n} \tag{2.41}$$

such that

$$Y(e^{it}) = |X(e^{it})|^2. \tag{2.42}$$

To use the Fejér-Riesz theorem, we need to guarantee the non-negativity of $q(m)$ for all m. We will do this by adjusting the value of c. For instance, we can always set c sufficiently small

so that $\max_{k\neq 0,\,|k|\leq\lambda-1} |\sin(\frac{\pi}{2}R(k))| \leq \frac{1}{2\lambda-2}$. Then we have

$$\begin{aligned} q(m) &= 1 + \sum_{k\neq 0,\,|k|\leq\lambda-1} \sin(\frac{\pi}{2}R(k))e^{-k\frac{2\pi im}{2\lambda-1}} \\ &\geq 1 + \sum_{k\neq 0,\,|k|\leq\lambda-1} -|\sin(\frac{\pi}{2}R(k))| \geq 0, \end{aligned} \tag{2.43}$$

as desired. This proves the existence of a solution to Eq. (2.39), and thus Eq. (2.36), for any target function $T(\omega)$.

In practice, we would like to set c as large as possible, and hence set $\max|R(k)|$ as large as possible (not necessarily bounded by $\max_{k\neq 0}|\sin(\frac{\pi}{2}R(k))| = \frac{1}{2\lambda-2}$). That is to say, we want to find:

$$c_{\text{opt}} = \arg\max c, \text{ subject to } q(m) \geq 0,\ \forall m \in \mathbb{R}. \tag{2.44}$$

An efficient and practical way to solve this problem is to relax these constraints, by restricting m to lie in the set $\{0, 1, ..., 2\lambda-2\}$, so that $e^{-k\frac{2\pi im}{2\lambda-1}}$ is uniformly distributed on the unit circle. Thus we can easily maximize c subject to these constraints:

$$c_{\text{relax}} = \arg\max c, \text{ subject to } q(m) \geq 0,\ \forall m \in \{0, 1, ..., 2\lambda-2\}. \tag{2.45}$$

Since c_{opt} is always smaller than c_{relax}, we should set c to be slightly smaller than c_{relax}. In practice, this can be done by trial and error.

Finally, we can solve Eq. (2.39) to recover $b(m)$, and thus obtain the a_i. In practice, this

can be done by solving the following nonlinear least-squares problem:

$$\vec{a} = \arg\min \sum_{m=0}^{2\lambda-2} (q(m) - |b(m)|^2)^2, \text{ such that } b(m) = \sum_{j=0}^{\lambda-1} a_j e^{-j\frac{2\pi i m}{2\lambda-1}}, \ \forall m \in \{0, 1, ..., 2\lambda-2\}. \tag{2.46}$$

This can be solved using gradient descent methods, or the Gerchberg-Saxton (GS) algorithm [64].

2.6 Measuring Linear Functionals of $S(\omega)$

We now combine all of the above pieces, in order to show, given a target function $T(\omega)$, how to construct the corresponding random pulse sequence that estimates the linear functional $I = \int S(\omega)T(\omega)d\omega$.

The random pulse sequence produces a certain window function, $W(\omega)$, that probes the noise. The expectation value of the window function over all the possible realizations of $\vec{U}$ yields

$$\mathbb{E}(W(\omega)) = M\tau^2 \operatorname{sinc}^2(\tfrac{\omega\tau}{2})[1 + 2\sum_{k=1}^{\lambda} R(k)\cos(k\omega\tau)(1 - \tfrac{k}{M})], \tag{2.47}$$

where we define $\operatorname{sinc} x = \frac{\sin x}{x}$ and λ is the cutoff distance of the correlation between random variables, i.e., $R(k) = 0$ whenever $k > \lambda$.

Our goal is to ensure that $\mathbb{E}(W(\omega))$ approximates some prescribed target function $T(\omega)$. Note that the cosine functions $\{\cos(k\omega\tau)\}$ form an almost complete basis (the zeroth term excluded) in the region $[-\frac{\pi}{\tau}, \frac{\pi}{\tau}]$. Thus, we take the following approach: we match the time interval between segments and the cutoff frequency of the noise (i.e., setting $\tau = \frac{\pi}{\omega_c}$), and we adjust the random pulse generator (i.e., optimizing the filter coefficients $(a_0, a_1, \ldots, a_{\lambda-1})$, using techniques

from phase retrieval, as explained in section 2.5), so that

$$R(k) = \frac{M}{\pi(M-k)} \int_{-\omega_c}^{\omega_c} \frac{cT(\omega)\cos(k\omega\tau)}{\mathrm{sinc}^2(\frac{\omega\tau}{2})} d\omega \quad (k = 1, \ldots, \lambda), \tag{2.48}$$

which implies

$$\mathbb{E}(W(\omega)) \xrightarrow{\lambda\to\infty} M\tau^2[cT(\omega) + (1 - cT_0)\,\mathrm{sinc}^2(\tfrac{\omega\tau}{2})]. \tag{2.49}$$

In Eqs. (2.48) and (2.49), c is a parameter that "rescales" the target function $T(\omega)$, in order to ensure that it can be approximated by a window function $W(\omega)$ that is generated by a stochastic process of the form (2.20). We show that a suitable value of the parameter c always exists, and describe a heuristic way of setting the parameter c (see Appendix 2.5). Essentially, we want to choose c as large as possible, subject to certain constraints (which can be easily checked). T_0 is a constant term depending on $T(\omega)$,

$$T_0 = \frac{1}{\omega_c} \int_{-\omega_c}^{\omega_c} \frac{T(\omega)}{\mathrm{sinc}^2(\frac{\omega\tau}{2})} d\omega. \tag{2.50}$$

Here, we have constructed the random pulse sequence $\vec{U}$ so that $R(k)$ is proportional to the k-th coefficient of the Fourier series representation of $T(\omega)/\,\mathrm{sinc}^2(\frac{\omega\tau}{2})$ (Eq. (2.48)). As such, Eq. (2.49) is a good approximation for a finite λ, if $R(k)$ converges to 0 as $k \to \infty$. By plugging Eq. (2.49) into Eq. (2.14), the expectation value of the decay exponent yields

$$\mathbb{E}(\chi) = \frac{M\tau^2}{2\pi} \int_{-\omega_c}^{\omega_c} [cT(\omega)S(\omega)d\omega + (1 - cT_0)\,\mathrm{sinc}^2(\tfrac{\omega\tau}{2})S(\omega)d\omega]. \tag{2.51}$$

Note that $\mathbb{E}(\chi)$ grows linearly with the total evolution time $T = M\tau$, as expected.

From Eq. (2.51), we can extract the desired functional, $I = \int S(\omega)T(\omega)d\omega$, by subtracting

the second term $\int S(\omega)\,\mathrm{sinc}^2(\frac{\omega\tau}{2})d\omega$ from $\mathbb{E}(\chi)$. This term can be estimated by applying an additional series of "base" random pulse sequences, for which $\vec{U}$ contains independent random variables (that is, $R(k) = 0$ for all $k > 0$). The expectation value of the "base" sequence's window function is $\mathbb{E}(W_{\text{base}}(\omega)) = \frac{M\tau^2}{2\pi}\,\mathrm{sinc}^2(\frac{\omega\tau}{2})$, and the corresponding decay exponent is $\mathbb{E}(\chi_{\text{base}}) = \frac{1}{2\pi}\int S(\omega)\,\mathbb{E}(W_{\text{base}}(\omega))$. This allows us to subtract the second term in Eq. (2.51). Alternatively, one can set up a Ramsey experiment of time τ to measure the second term. The cost for each method depends on experimental details. For example, ideally we want χ to be of order 1. When τ is too small, χ might be too close to 0 for the Ramsey experiment, thus increasing the number of measurements needed to reach certain accuracy.

Figure 4.1 illustrates the window functions generated by the random pulse protocol for a target function of $T_1(\omega) = \mathrm{sinc}^2\left(\frac{\omega\tau}{2}\right)\cos\left(3\omega\tau\right)$. The value of $\mathbb{E}(W_{base})$ (dashed magenta line in Fig. 2.5a) is subtracted from $\mathbb{E}(W(\omega))$ (dashed cyan line in Fig. 2.5a), to obtain $T(\omega)$ (dashed cyan line in Fig. 2.5b).

The experimental estimation of the desired functional, I^{exp}, requires measuring the decay exponent χ^{exp}, by generating N_1 different random pulse sequences with each repeated N_2 times, as well as measuring the base decay exponent, $\chi^{\text{exp}}_{\text{base}}$, by generating $N_{\text{base},1}$ different random pulse sequences with each repeated $N_{\text{base},2}$ times (see section 2.7.3).

Note that we are free to choose larger values of N_1 and N_2 in order to obtain better accuracy; whereas our choices of T, M and τ are more constrained. In particular, T must be chosen so that the decay exponent χ is of order 1 (so that it can be estimated from a small number of experimental trials); τ is constrained by the capabilities of the experimental apparatus and its control system; and M must satisfy $T = M\tau$.

For the specific target function $T(\omega)$ in Fig. 4.1, the application of random pulse sequences

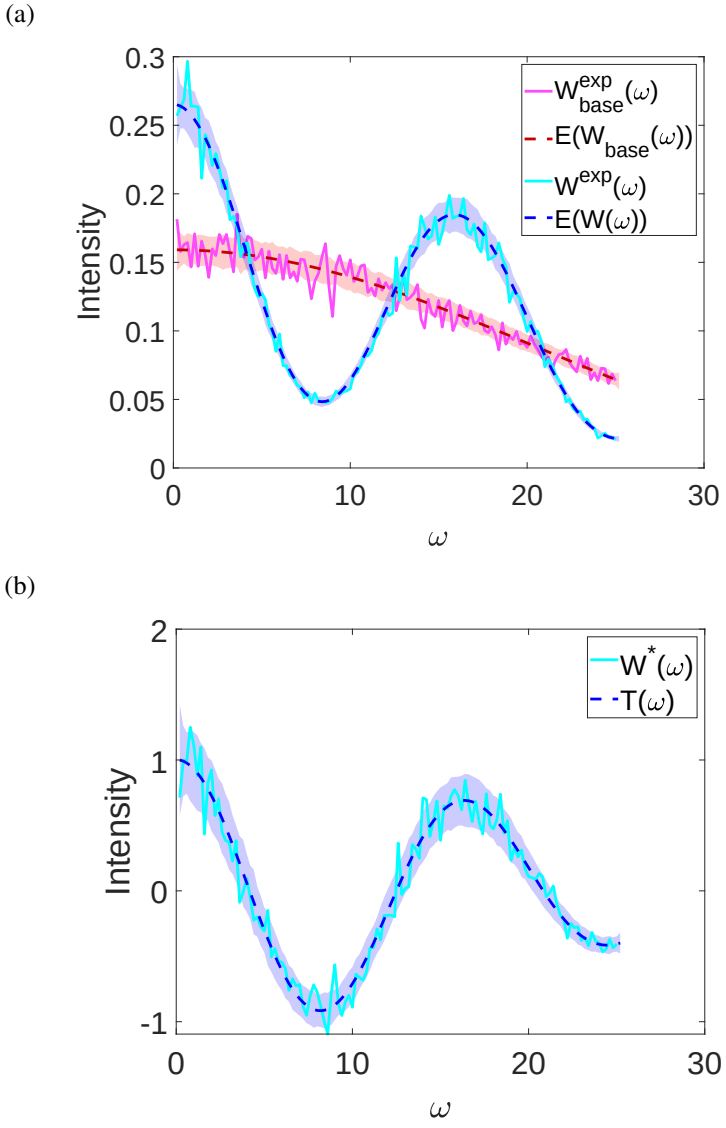


Figure 2.5: Illustration of the generation of the target function $T(\omega) = \mathrm{sinc}^2(\omega\pi/50)\cos(3\omega\pi/25)$ by two groups of random pulses. In both plots, the dashed lines represent exact expectation values. The solid lines represent simulated results of an experimental realization considering 200 random pulse sequences with 250 segments, each repeated 200 times. The shaded areas represent the ± 1 standard deviation of these results. (a) The dashed blue line (dashed red line) stands for the expectation value of the window function, $\mathbb{E}(W(\omega))$ (of the base window function, $\mathbb{E}(W_{\text{base}}(\omega))$), generated by $T(\omega)$, and the solid cyan line (solid magenta line) is one corresponding simulation of the experimental result, $W^{\text{exp}}(\omega)$ ($W^{\text{exp}}_{\text{base}}(\omega)$). (b) The dashed blue line represents $T(\omega)$. The solid cyan line stands for the extracted window function of the two averaged window functions in (a), calculated by $W^*(\omega) = [W^{\text{exp}}(\omega) - (1 - cT_0)W^{\text{exp}}_{\text{base}}(\omega)]/c$. Here c is set to be $1/3$.

with $(M, N_1, N_2) = (M, N_{\text{base},1}, N_{\text{base},2}) = (200, 200, 50)$ (solid lines in Fig. 4.1) provides a close estimation of the expectation values (dashed lines in Fig. 4.1).

2.7 Accuracy of the method

In this section, we will analyze the accuracy of the random pulse sequence method. Recall that we need to estimate the desired linear functional, $I = \int S(\omega)T(\omega)d\omega$, from the expected decay exponent $\mathbb{E}(\chi)$ (Eq. (2.51)). The accuracy of the estimator thus depends on the error in the decay exponent measured, χ^{exp}.

Theorem 2 *For random pulse sequence experiments containing N_1 different sequences with each repeated N_2 times, the accuracy of the measured decay exponent, $\chi^{exp} = \chi_U^{exp}(T)$, is upper bounded by*

$$|\chi_U^{exp}(T) - \mathbb{E}(\chi_U(T))| = O\left(\frac{\sqrt{Var(\chi_U(T))}}{\sqrt{N_1}} + \frac{\mathbb{E}(\chi_U(T))}{\sqrt{N_1 N_2}}\right), \tag{2.52}$$

$$Var(\chi_U(T)) \leq \frac{(7\tilde{\lambda}^2 + 10\tilde{\lambda} + 1)M\tau^3}{\pi} ||S(\omega)\,\text{sinc}^2(\tfrac{\omega\tau}{2}) - \langle S(\omega)\,\text{sinc}^2(\tfrac{\omega\tau}{2})\rangle||_{L2}^2. \tag{2.53}$$

Here $\tilde{\lambda}$ is a parameter that quantifies the correlations in the random pulse sequence, which is defined precisely in Section 2.7.2. $S(\omega)$ is the noise spectrum, M is the total number of pulses, τ is the time between pulses, and $\langle\cdot\rangle$ denotes averaging over the frequency domain, i.e., $\langle f(\omega)\rangle = \frac{\tau}{2\pi}\int_{-\pi/\tau}^{\pi/\tau} f(\omega)d\omega$.

The proof of this theorem goes in this way: we first upper-bound the variance of the decay exponent, $\text{Var}(\chi_U(T))$, for a given group of random pulse sequences. Then we describe the method for estimating $\chi_U(T)$ (i.e., computing $\chi_U^{\text{exp}}(T)$) based on experimental data, and we derive a bound on the error in $\chi_U^{\text{exp}}(T)$.

2.7.1 Variance of the decay exponent: the uncorrelated case

In this part we calculate the variance of the decay exponent. Using Eqs. (4.11) and (2.29), the variance of $\chi_U(T)$ is given by

$$\begin{aligned}\text{Var}(\chi_U(T)) &= \mathbb{E}(\chi_U(T)^2) - \mathbb{E}(\chi_U(T))^2 \\ &= \frac{\tau^4}{4\pi^2}\sum_{ijkl}(\mathbb{E}(U_iU_jU_kU_l) - \mathbb{E}(U_iU_j)\,\mathbb{E}(U_kU_l))B_{i,j}(S)B_{k,l}(S)\end{aligned} \tag{2.54}$$

The fourth order term $\mathbb{E}(U_iU_jU_kU_l)$ is in general hard to evaluate. So let us first consider a special case, where the U_i are completely independent. For this case, we will obtain the upper bound (2.53) with $\tilde{\lambda} = 0$.

This uncorrelated case is also referred in the main work as the base random pulse sequence. Recall that the random variables of the base sequence are all independent with $\mathbb{E}(U_iU_j) = \delta_{ij}$, such that

$$\mathbb{E}(U_iU_jU_kU_l) = \delta_{ij,kl} + \delta_{ik,jl} + \delta_{il,kj} - 2\delta_{i,j,k,l}. \tag{2.55}$$

Substitute it into Eq. (2.54). Combined with the fact that $B(S) = B(S)^T$ ($S(\omega)$ is an even function of ω), we get

$$\text{Var}(\chi_U(T)) = \frac{\tau^4}{4\pi^2}[2\text{Tr}(B(S)^2) - 2\sum_i B_{i,i}(S)^2]. \tag{2.56}$$

We can bound $\text{Tr}(B(S)^2)$ as follows, using Parseval's theorem:

$$\begin{aligned}
\text{Tr}(B(S)^2) &= \sum_{m,m'=1}^{M} |B_{m,m'}(S)|^2 \\
&= \sum_{m=1}^{M} \sum_{l=1-m}^{M-m} |\hat{S}_l|^2 \\
&\leq M \sum_{l=-\infty}^{\infty} |\hat{S}_l|^2 \\
&= \frac{2M\pi}{\tau} \int_{-\pi/\tau}^{\pi/\tau} S^2(\omega) \,\text{sinc}^4(\tfrac{\omega\tau}{2}) d\omega \\
&= \frac{2M\pi}{\tau} ||S(\omega) \,\text{sinc}^2(\tfrac{\omega\tau}{2})||_{L2}^2.
\end{aligned} \tag{2.57}$$

We then have an upper bound for the variance of the decay exponent:

$$\begin{aligned}
\text{Var}(\chi_U(T)) &= \frac{\tau^4}{4\pi^2} (\frac{4M\pi}{\tau} ||S(\omega) \,\text{sinc}^2(\tfrac{\omega\tau}{2})||_{L2}^2 - 2M ||S(\omega) \,\text{sinc}^2(\tfrac{\omega\tau}{2})||_{L1}^2) \\
&\leq \frac{M\tau^3}{\pi} ||S(\omega) \,\text{sinc}^2(\tfrac{\omega\tau}{2}) - \langle S(\omega) \,\text{sinc}^2(\tfrac{\omega\tau}{2}) \rangle||_{L2}^2.
\end{aligned} \tag{2.58}$$

Interestingly, the variance of the measured decay rate is bounded by the difference between the square of L2 norm and L1 norm of the function $S(\omega) \,\text{sinc}^2(\frac{\omega\tau}{2})$. This can be seemed as the deviation of $S(\omega) \,\text{sinc}^2(\frac{\omega\tau}{2})$ from a constant function. When this function is exactly a constant function in the frequency regime $[-\pi/\tau, \pi/\tau]$, $\text{Var}(\chi_U(T))$ is precisely 0. At the opposite extreme, if $S(\omega) \,\text{sinc}^2(\frac{\omega\tau}{2})$ is a sparse signal with a single peak of width $\Delta\omega$, then $\text{Var}(\chi_U(T))$ is of order $O(\frac{\omega_c}{M\Delta\omega} \,\mathbb{E}^2(\chi_U(T)))$.

2.7.2 Variance of the decay exponent: the general case

In this section, we will derive an upper bound on the variance of the decay exponent $\chi_U(T)$, in a more general case where $\mathbb{E}(U_i U_j) = R(j-i)$ for some arbitrary correlation coefficients

$R(1), R(2), R(3), \ldots$. For this purpose, we will define a parameter $\tilde{\lambda}$ that characterizes the structure of the correlations among the random variables $U_i (i = 1, \ldots, M)$.

We will view U_i as a Markov random field. According to Section 2.4, U_i is defined by the sign of jointly normal random variables: $U_i = \text{sign}(\vec{V}_i \vec{N}^T)$. We define a dependency graph G (on vertices $V = \{1, \ldots, M\}$) based on the normal random variables $\vec{V}_i \vec{N}^T$, in which vertices i, j are connected if $\mathbb{E}(\vec{V}_i \vec{N}^T \vec{V}_j \vec{N}^T) \neq 0$. It follows that $\vec{V}_i \vec{N}^T$ form a Gaussian Markov random field (GMRF) respect to G [86]:

1. For any i, j not equal or adjacent, $\vec{V}_i \vec{N}^T \perp\!\!\!\perp \vec{V}_j \vec{N}^T \mid \vec{V}_{V \setminus \{i,j\}} \vec{N}^T$,
2. For any $i \in V$ and $J \subset V$ not containing or adjacent to i, $\vec{V}_i \vec{N}^T \perp\!\!\!\perp \vec{V}_J \vec{N}^T \mid \vec{V}_{V \setminus \{i\} \cap J} \vec{N}^T$.

Applying the sign function does not introduce new dependencies that would alter the conditional independence structure inherent in the original GMRF. That is to say,

1. For any i, j not equal or adjacent, $\vec{V}_i \vec{N}^T \perp\!\!\!\perp \vec{V}_j \vec{N}^T \mid \text{sign}(\vec{V}_{V \setminus \{i,j\}} \vec{N}^T)$,
2. For any $i \in V$ and $J \subset V$ not containing or adjacent to i, $\vec{V}_i \vec{N}^T \perp\!\!\!\perp \vec{V}_J \vec{N}^T \mid \text{sign}(\vec{V}_{V \setminus \{i\} \cap J} \vec{N}^T)$.

Furthermore, since the sign function is symmetric on normal random variables with zero mean, the marginal probability distributions of $\text{sign}(\vec{V}_i \vec{N}^T)$ and $\text{sign}(\vec{V}_j \vec{N}^T)$ are also conditionally independent for any i, j not equal or adjacent. For example,

$$
\begin{aligned}
&P(\text{sign}(\vec{V}_i \vec{N}^T) = 1, \text{sign}(\vec{V}_j \vec{N}^T) = 1 | \text{sign}(\vec{V}_{V \setminus \{i,j\}} \vec{N}^T)) \\
&\quad = P(\vec{V}_i \vec{N}^T > 0,\ \vec{V}_j \vec{N}^T > 0 | \text{sign}(\vec{V}_{V \setminus \{i,j\}} \vec{N}^T)) \\
&\quad = P(\vec{V}_j \vec{N}^T > 0 | \text{sign}(\vec{V}_{V \setminus \{i,j\}} \vec{N}^T))\, P(\vec{V}_j \vec{N}^T > 0 | \text{sign}(\vec{V}_{V \setminus \{i,j\}} \vec{N}^T)) \\
&\quad = P(\text{sign}(\vec{V}_i \vec{N}^T) = 1 | \text{sign}(\vec{V}_{V \setminus \{i,j\}} \vec{N}^T))\, P(\text{sign}(\vec{V}_j \vec{N}^T) = 1 | \text{sign}(\vec{V}_{V \setminus \{i,j\}} \vec{N}^T)).
\end{aligned}
\tag{2.59}
$$

Thus we have:

1. For any i, j not equal or adjacent, $U_i \perp\!\!\!\perp U_j \mid U_{V\setminus\{i,j\}}$,

2. For any $i \in V$ and $J \subset V$ not containing or adjacent to i, $U_i \perp\!\!\!\perp U_J \mid U_{V\setminus\{i\}\cap J}$.

So the U_i also form a Markov random field respect to the same dependency graph G. We then define $\tilde{\lambda}$ as the maximum degree of G, which equals 2 times the number of nonzero $R(K)$s.

Next, we can use Eq. (2.54) to write the variance of $\chi_U(T)$ as:

$$\frac{4\pi^2}{\tau^4}\text{Var}(\chi_U(T)) = \sum_{ijkl} \Lambda_{ijkl} B_{ij}(S) B_{kl}(S),$$

where we define

$$\Lambda_{ijkl} = \mathbb{E}(U_i U_j U_k U_l) - \mathbb{E}(U_i U_j)\,\mathbb{E}(U_k U_l).$$

Note that $U_i^2 = 1$. Hence, whenever $i = j$ or $k = l$, we have $\Lambda_{ijkl} = 0$. Thus we can write:

$$\frac{4\pi^2}{\tau^4}\text{Var}(\chi_U(T)) = \sum_{i\neq j, k\neq l} \Lambda_{ijkl} B_{ij}(S) B_{kl}(S). \tag{2.60}$$

Now consider any $(i, j, k, l) \in \{1, ..., M\}^4$ such that $i \neq j$ and $k \neq l$. Then (i, j, k, l) must belong to one of the cases described below. For each of these cases, we will upper-bound the corresponding contribution to the sum in Eq. (2.60):

- Case 1: $\{i, j\} = \{k, l\}$. Then we have the following upper bound:

$$\sum_{(i,j,k,l) \text{ in case 1}} \Lambda_{ijkl} B_{ij}(S) B_{kl}(S) \leq 2 \sum_{i\neq j} |B_{ij}(S)|^2 \leq 2M \sum_{\ell\neq 0} \left|\hat{S}_\ell\right|^2,$$

where we used the fact that $\Lambda_{ijij} = \Lambda_{ijji} = 1 - \mathbb{E}(U_i U_j)^2 \leq 1$, and the definition of $B_{ij}(S)$ in Eq. (4.11).

- Case 2: $|\{i,j\} \cap \{k,l\}| = 1$. Without loss of generality, suppose that $j = k$. Then we have $\Lambda_{ijkl} = \Lambda_{ijjl} = \mathbb{E}(U_i U_l) - \mathbb{E}(U_i U_j)\,\mathbb{E}(U_j U_l)$. Now let H be the induced subgraph of G on the set of vertices $\{i,j,l\}$. H belongs to one of the following cases:

  - Case 2(a): H has no edges, i.e., all three vertices in H are isolated. This implies that $\Lambda_{ijjl} = 0$, and thus does not contribute to the above sum.

  - Case 2(b): H consists of two connected components. This implies that one of the vertices in H is isolated (has no edges). If the isolated vertex is i or l, then $\Lambda_{ijjl} = 0$, and thus does not contribute to the above sum. If the isolated vertex is j, then $\Lambda_{ijjl} = \mathbb{E}(U_i U_l) \leq 1$, and i and l are connected by an edge in H. Then we have the following upper bound:

$$\begin{aligned}
&\sum_{(i,j,j,l) \text{ in case 2(b)}} \Lambda_{ijjl} B_{ij}(S) B_{jl}(S) \\
&\qquad \leq \tfrac{1}{2} \sum_{(i,j,j,l) \text{ in case 2(b) s.t. } i \sim l \text{ in } H} |B_{ij}(S)|^2 + |B_{jl}(S)|^2 \\
&\qquad \leq \tfrac{1}{2}\tilde{\lambda} \sum_{i \neq j} |B_{ij}(S)|^2 + \tfrac{1}{2}\tilde{\lambda} \sum_{j \neq l} |B_{jl}(S)|^2 \leq \tilde{\lambda} M \sum_{\ell \neq 0} \left|\hat{S}_\ell\right|^2,
\end{aligned}$$

    where we used the arithmetic-geometric mean inequality, and the fact that for any choice of i, there are at most $\tilde{\lambda}$ choices of l that contribute to the sum, and vice versa.

  - Case 2(c): H consists of a single connected component. Note that $\Lambda_{ijjl} \leq 2$. Using a

similar argument as in case 2(b), we have the following upper bound:

$$\begin{aligned}
&\sum_{(i,j,j,l) \text{ in case 2(c)}} \Lambda_{ijjl} B_{ij}(S) B_{jl}(S) \\
&\qquad \leq \sum_{(i,j,j,l) \text{ in case 2(c) s.t. } H \text{ is connected}} |B_{ij}(S)|^2 + |B_{jl}(S)|^2 \\
&\qquad \leq 2\tilde{\lambda} \sum_{i \neq j} |B_{ij}(S)|^2 + 2\tilde{\lambda} \sum_{j \neq l} |B_{jl}(S)|^2 \leq 4\tilde{\lambda} M \sum_{\ell \neq 0} \left| \hat{S}_\ell \right|^2,
\end{aligned}$$

where we used the fact that for any choices of i and j (respectively j and l), there are at most $2\tilde{\lambda}$ choices of l (respectively i) that contribute to the sum.

- Case 3: $\{i, j\} \cap \{k, l\} = \emptyset$. Let H be the induced subgraph of G on the set of vertices $\{i, j, k, l\}$. H belongs to one of the following cases:

  – Case 3(a): There exists at least one vertex in H has no edges, i.e., it is isolated (disconnected) from all of the other vertices. Without loss of generality, let this be vertex i. This implies that

$$\Lambda_{ijkl} = \mathbb{E}(U_i)\, \mathbb{E}(U_j U_k U_l) - \mathbb{E}(U_i)\, \mathbb{E}(U_j)\, \mathbb{E}(U_k U_l) = 0,$$

  and thus does not contribute to the above sum.

  – Case 3(b): H consists of two edges (i, j) and (k, l). This implies that

$$\Lambda_{ijkl} = \mathbb{E}(U_i U_j)\, \mathbb{E}(U_k U_l) - \mathbb{E}(U_i U_j)\, \mathbb{E}(U_k U_l) = 0,$$

  and thus does not contribute to the above sum.

– Case 3(c): H consists of two edges (i,k) and (j,l). Then we have the following upper-bound:

$$\sum_{(i,j,k,l) \text{ in case 3(c)}} \Lambda_{ijkl} B_{ij}(S) B_{kl}(S)$$
$$\leq \tfrac{1}{2} \sum_{(i,j,k,l) \text{ in case 3(c) s.t. } i\sim k, j\sim l \text{ in } H} |B_{ij}(S)|^2 + |B_{kl}(S)|^2$$
$$\leq \tfrac{1}{2}\tilde{\lambda}^2 \sum_{i\neq j} |B_{ij}(S)|^2 + \tfrac{1}{2}\tilde{\lambda}^2 \sum_{k\neq l} |B_{kl}(S)|^2 \leq \tilde{\lambda}^2 M \sum_{\ell\neq 0} \left|\hat{S}_\ell\right|^2,$$

where we used the fact that for any choices of i and j (respectively k and l), there are at most $\tilde{\lambda}^2$ choices of k and l (respectively i and j) that contribute to the sum.

– Case 3(d): H consists of two edges (i,l) and (j,k). For this case, we have the same upper-bound as for case 3(c).

– Case 3(e): H consists of a single connected component. Note that $\Lambda_{ijkl} \leq 2$. Then we have the following upper bound:

$$\sum_{(i,j,k,l) \text{ in case 3(e)}} \Lambda_{ijkl} B_{ij}(S) B_{jl}(S)$$
$$\leq \sum_{(i,j,k,l) \text{ in case 3(e) s.t. } H \text{ is connected}} |B_{ij}(S)|^2 + |B_{jl}(S)|^2$$
$$\leq 6\tilde{\lambda}^2 \sum_{i\neq j} |B_{ij}(S)|^2 + 6\tilde{\lambda}^2 \sum_{j\neq l} |B_{jl}(S)|^2 \leq 12\tilde{\lambda}^2 M \sum_{\ell\neq 0} \left|\hat{S}_\ell\right|^2,$$

where we used the fact that for any choices of i and j (respectively k and l), there are at most $(2\tilde{\lambda})(3\tilde{\lambda})$ choices of k and l (respectively i and j) that contribute to the sum.

Combining the above results, and using Parseval's identity, we get the following upper

bound on the variance of $\chi_U(T)$:

$$\mathrm{Var}(\chi_U(T)) \leq \frac{(7\tilde{\lambda}^2 + 10\tilde{\lambda} + 1)M\tau^3}{\pi} ||S(\omega)\,\mathrm{sinc}^2(\tfrac{\omega\tau}{2}) - \langle S(\omega)\,\mathrm{sinc}^2(\tfrac{\omega\tau}{2})\rangle||_{L2}^2. \tag{2.61}$$

Note that the bound in Eq. (2.61) also holds for previous cases in Eq. (2.58) and Eq. (2.82) when one sets $\tilde{\lambda} = 0$ and $\tilde{\lambda} = 1$, respectively.

2.7.3 Experimental estimation of the decay exponent

In order to estimate the $\chi_U(T)$ accurately, we need to set the parameters τ and M appropriately, perform multiple runs of the experiment (using different pulse sequences), and average the results. Here, we describe how to do this.

First, we choose the period τ of the random pulse sequences. We assume that we are given some high-frequency cutoff ω_c, such that $S(\omega)$ is supported inside the interval $[-\omega_c, \omega_c]$.

Next, we choose the length M of the random pulse sequences. Our goal is to ensure that $\chi_U(T)$ is of order 1, so that it can be accurately estimated by observing events that occur with probability $P_0(\vec{U}) = \frac{1}{2}(1 + e^{-\chi_U(T)})$. Based on equation (2.34), we know that $\chi_U(T)$ is linearly dependent on M. Here, we assume that we are given an initial guess for $\chi_U(T)$ (call it χ_g) that has the correct order of magnitude. We then use χ_g to choose the value of M.

To be concrete, let us assume that χ_g lies within the range

$$\frac{\chi_U(T)}{10} \leq \chi_g \leq 10\chi_U(T). \tag{2.62}$$

Then we set

$$M = \left\lceil \frac{2\pi}{\tau^2 \chi_g} \right\rceil. \tag{2.63}$$

The actual value of $\chi_U(T)$ will fluctuate around its expectation, but these fluctuations will less than 1 with high probability, as shown later by equation (2.68).

Let us fix two parameters N_1 and N_2. We then choose N_1 random pulse sequences (let us call them $\vec{U}^{(j)}$, for $j = 1, \ldots, N_1$). For each pulse sequence $\vec{U}^{(j)}$, we run N_2 trials of the experiment, and obtain measurement outcomes

$$X_{jk} = \begin{cases} 1 & \text{if we observe } |0\rangle \\ -1 & \text{if we observe } |1\rangle, \end{cases} \tag{2.64}$$

for $k = 1, \ldots, N_2$. Note that X_{jk} has expectation value $\mathbb{E}(X_{jk} \,|\, \vec{U}^{(j)}) = \exp\bigl(-\chi_{U_j}(T)\bigr)$. This motivates us to define an estimator χ as follows:

$$Y_j = \frac{1}{N_2} \sum_{k=1}^{N_2} X_{jk}, \tag{2.65}$$

$$Z_j = -\log Y_j, \tag{2.66}$$

$$\chi^{\text{exp}} = \frac{1}{N_1} \sum_{j=1}^{N_1} Z_j. \tag{2.67}$$

2.7.4 Accuracy of the estimator

At last, we can combine the previous results and derive a bound for χ^{exp}. Recall that the variance of χ_U is bounded by Eq. (2.61). Using Chebyshev's inequality plus a union bound, we

can prove that for all j over $\vec{U}^{(j)}$,

$$P(|\chi_{U_j}(T) - \mathbb{E}(\chi)| > N_1 \sqrt{\frac{(7\tilde{\lambda}^2 + 10\tilde{\lambda} + 1)M\tau^3}{\pi}} ||S(\omega)\,\mathrm{sinc}^2(\tfrac{\omega\tau}{2}) - \langle S(\omega)\,\mathrm{sinc}^2(\tfrac{\omega\tau}{2})\rangle||_{L2}) \leq \frac{1}{N_1}. \tag{2.68}$$

Since $\mathbb{E}(\chi)$ scales linearly with M, $\chi_{U_j}(T)$ is quite concentrated when M is large. Following a Bernstein-type inequality for sub-exponential random variables [37], we obtain

$$\frac{1}{N_1}\sum_{j=1}^{N_1} \chi_{U_j}(T) \approx \mathbb{E}(\chi_U(T)) \pm \sqrt{\frac{(7\tilde{\lambda}^2 + 10\tilde{\lambda} + 1)M\tau^3}{\pi}} \frac{||S(\omega)\,\mathrm{sinc}^2(\tfrac{\omega\tau}{2}) - \langle S(\omega)\,\mathrm{sinc}^2(\tfrac{\omega\tau}{2})\rangle||_{L2}}{\sqrt{N_1}}. \tag{2.69}$$

Conditioned on choices of the $\vec{U}^{(j)}$ that satisfy the above properties, we will now consider the probabilities over X_{jk}, which are independent Bernoulli random variables. According to Hoeffding's inequality,

$$P(|Y_j - \exp\big(-\chi_{U_j}(T)\big)| \geq t) \leq 2\exp\left(-\frac{N_2 t^2}{2}\right). \tag{2.70}$$

So Y_j has a binomial distribution with exponentially-decaying tails, centered around $\exp\big(-\chi_{U_j}(T)\big)$, with standard deviation $O(\exp\big(-\chi_{U_j}(T)\big)/\sqrt{N_2})$. The random variable Z_j takes the negative logarithm of Y_j, which also has exponentially-decaying tails centered around $\chi_{U_j}(T)$ and with standard deviation $O(\chi_{U_j}(T)/\sqrt{N_2})$. This holds because we are in the regime where the log function does not blow up too badly, because of (2.68). Then with high probability,

$$\chi^{\text{exp}} \approx \frac{1}{N_1}\sum_{j=1}^{N_1} \chi_{U_j}(T) \pm \frac{O(\chi_{U_j}(T))}{\sqrt{N_1 N_2}}. \tag{2.71}$$

This follows from a Bernstein-type inequality for sub-exponential random variables [37].

Now combining (2.69) and (2.71), we can see that

$$\chi^{\text{exp}} \approx \mathbb{E}(\chi) \pm \sqrt{\frac{(7\tilde{\lambda}^2 + 10\tilde{\lambda} + 1)M\tau^3}{\pi}} \frac{||S(\omega)\,\text{sinc}^2(\frac{\omega\tau}{2}) - \langle S(\omega)\,\text{sinc}^2(\frac{\omega\tau}{2})\rangle||_{L2}}{\sqrt{N_1}} \pm O(\frac{\mathbb{E}(\chi)}{\sqrt{N_1 N_2}}). \tag{2.72}$$

Note that there are two error terms. Increasing N_1 causes both error terms to decrease, increasing N_2 only helps with the second error term. Thus the best strategy is to make N_1 large, and keep N_2 as small as possible.

But how small can we choose N_2? If N_2 is too small, we have problems: Y_j can be close to zero, which causes the log function to blow up when computing Z_j. To avoid these problems, we need to make sure that $1/\sqrt{N_2} \leq O(\exp(-\chi_{U_j}))$, or equivalently, $N_2 \geq \Omega(\exp(2\chi_{U_j}))$.

Although we don't know the value of χ_{U_j} a priori, we can set N_2 adaptively to get close to this bound. For most choices of $\vec{U}^{(j)}$, χ_{U_j} is at most some constant, hence setting N_2 to be a constant should be good enough. However, since we are using N_1 random pulse sequences ($\vec{U}^{(j)}$, for $j = 1, \ldots, N_1$), we expect there could be a few $\vec{U}^{(j)}$ where χ_{U_j} could be as large as equation (2.68). For those $\vec{U}^{(j)}$, we could obtain a large estimation for χ_{U_j} and increase N_2 accordingly.

Another way to get rid of the problem with large χ_{U_j} is to use the median of means method [87, 88]. We can construct K independent sets of size N_1. For each individual set, we do the same experiment as we discussed before and get an estimation for the decay rate. We then find the median of their values. It is guaranteed that for K independent sets of size $N_1 = 34Z/\epsilon^2$ suffice to construct a median of mean estimator $\chi^{\text{exp}}_{\text{median}}$ that obeys

$$\Pr(|\chi^{\text{exp}}_{\text{median}} - \mathbb{E}(X)| \geq \epsilon) \leq 2e^{-K/2}, \tag{2.73}$$

where $Z = \frac{(7\tilde{\lambda}^2+10\tilde{\lambda}+1)M\tau^3}{\pi}||S(\omega)\,\mathrm{sinc}^2(\frac{\omega\tau}{2}) - \langle S(\omega)\,\mathrm{sinc}^2(\frac{\omega\tau}{2})\rangle||_{L2}^2$.

Combine all of the above pieces, the accuracy of the experimental estimation of the desired functional, I^{exp}, depends on the accuracies of the experimentally measured decay exponents, which are also yielded by the method to generate random pulses. This accuracy can be bounded in the following way:

$$\mathrm{Var}(\chi) \leq \frac{(7\tilde{\lambda}^2+10\tilde{\lambda}+1)M\tau^3}{\pi}||S(\omega)\,\mathrm{sinc}^2(\tfrac{\omega\tau}{2}) - \langle S(\omega)\,\mathrm{sinc}^2(\tfrac{\omega\tau}{2})\rangle||_{L2}^2, \tag{2.74}$$

$$|\chi^{\mathrm{exp}} - \mathbb{E}(\chi)| = O\left(\frac{\sqrt{\mathrm{Var}(\chi)}}{\sqrt{N_1}} + \frac{\mathbb{E}(\chi)}{\sqrt{N_1 N_2}}\right). \tag{2.75}$$

Here $\mathrm{Var}(\chi)$ is the variance of the decay rate χ with respect to the choice of the random pulse sequence. $\tilde{\lambda}$ denotes twice the number of nonzero $R(k)$s, and can be interpreted as an upper bound on the complexity of the correlations among the random pulses. $\langle\cdot\rangle$ denotes averaging over the frequency domain, i.e., $\langle f(\omega)\rangle = \frac{\tau}{2\pi}\int_{-\pi/\tau}^{\pi/\tau} f(\omega)d\omega$. Finally, a bound similar to Eq. (2.75) holds for $|\chi_{\mathrm{base}}^{\mathrm{exp}} - \mathbb{E}(\chi_{\mathrm{base}})|$ with $\mathbb{E}(W_{\mathrm{base}}(\omega)) = M\tau^2\,\mathrm{sinc}^2(\frac{\omega\tau}{2})$.

One interesting consequence of Eq. (2.74) is that, as the number of pulses M grows large, $\mathrm{Var}(\chi)$ scales roughly linearly with M. This implies that the fluctuations in χ are small (of order $1/\sqrt{M}$) relative to the expectation value of χ:

$$\frac{\sqrt{\mathrm{Var}(\chi)}}{\mathbb{E}(\chi)} \propto \frac{\tilde{\lambda}}{\sqrt{M}}. \tag{2.76}$$

Intuitively, the M random pulses behave as if they were independent, up to a correction factor that depends on $\tilde{\lambda}$ (but not on M). This intuition is made precise in the proof of Eq. (2.74), by modeling the random variables U_i as a Markov random field with some correlation graph G, and observing that $\tilde{\lambda}$ is related to the maximum degree of G. (See section 2.7.2.)

Equation (2.74) also depends on the squared L_2 norm of $S(\omega)\,\mathrm{sinc}^2(\frac{\omega\tau}{2})$ minus its average value. This can be viewed as a measure of the smoothness of $S(\omega)\,\mathrm{sinc}^2(\frac{\omega\tau}{2})$. This is consistent with what one might intuitively expect, when applying a random pulse sequence that samples the noise at many different frequencies simultaneously: when $S(\omega)\,\mathrm{sinc}^2(\frac{\omega\tau}{2})$ is roughly constant on all frequencies, the fluctuations in χ should be small; but when $S(\omega)\,\mathrm{sinc}^2(\frac{\omega\tau}{2})$ consists of isolated peaks, the fluctuations in χ can be large.

When performing noise spectroscopy on a real physical system, one needs a way to estimate the right hand side of Eq. (2.74), using physical parameters of the environment that may be known *a priori*. This can be done by using Holder's inequality $\|A\|_{L2}^2 \leq \|A\|_{L1}\|A\|_{L\infty}$, and then plugging in upper bounds on the total noise strength, and the maximum noise strength at any single frequency. These bounds can come from knowledge of physical interactions and energy scales in the system.

Finally, Eq. (2.75) suggests a simple strategy for minimizing the error in the measured decay exponent χ^{exp}: make N_1 large, while keeping N_2 as small as possible. One interesting possibility is to set $N_2 = 1$, so that each run of the experiment uses an independently-sampled random pulse sequence. This approach bears some resemblance to fully randomized benchmarking [89].

Setting $N_2 = 1$ causes difficulties with the statistical estimation of the decay exponent for each random pulse sequence, because there is no averaging to smooth out the shot noise. Nonetheless it is still possible to obtain crude statistical estimates in this situation (see Appendix 2.7.4). This approach is suitable for experimental setups where the random pulse sequence can be generated in real time, using a field programmable gate array (FPGA) or fast programmable logic. One advantage of this approach is that it removes the need to store the random pulse sequence in

computer memory.

2.8 Alternative generator

The general method is powerful since it can be used to approximate arbitrary target functions, $T(\omega)$, using the average window function of the pulse sequences. However, in some special cases where the form of $T(\omega)$ is restricted, we can utilize other simplified but efficient pulse generators. For example, in the compressed sensing case, we want to generate random pulse sequences where only one of the covariances $R(k)$ ($k \neq 0$) is nonzero, i.e., there exists some $k' \geq 1$ such that, for all $k \geq 1$, $R(k)$ has the form $R(k) = \delta_{kk'} R(k')$. An alternative generator can be used for this particular job with a simpler structure and fewer hardware memories.

Using the terminology of the previous section, this alternative method is equivalent to using a *time-varying* FIR filter. The resulting covariances $\mathbb{E}(U_i U_{i+k})$ depend on both the time i and the time-difference k; but if one averages over i, one obtains the desired covariance $R(k)$. This kind of averaging occurs naturally in experiments, whenever the bath dynamics are *time-independent*.

The idea of this alternative method is to create correlated pairs. As shown in Fig. 2.6, the chain of circles represents the random pulse sequence, labelled by the random variables $\vec{U} = (U_1, U_2, ..., U_M) \in \{1, -1\}^M$. The sequence of random variables is split into independent segments with length $2k'$, indicated by the red dashed lines, so that the random variables from different segments are independent. Each segment is further divided into two halves ("left" and "right") by the green dashed lines. The variables on the left side of the segments are chosen uniformly random from $\{-1, 1\}$. We then choose some r in the range $[-1/2, 1/2]$. For every variable on the right side, one can always find a corresponding variable in the left side, such that

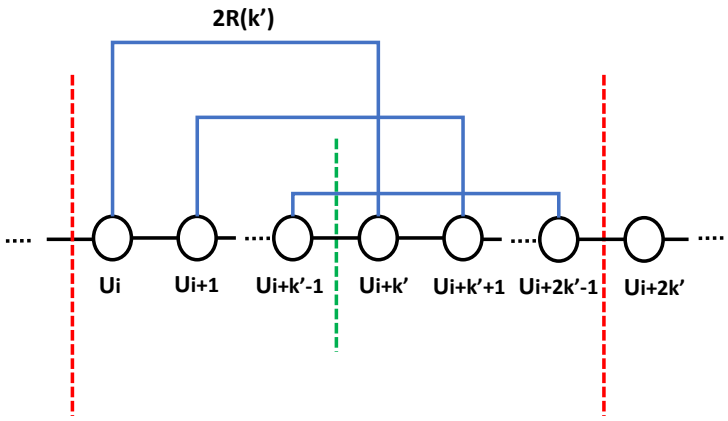


Figure 2.6: An illustration to generate the random pulses with only one nonzero $R(k)$ (corresponding to $k = k'$) using the alternative generator. The black circles represent the random pulse sequence, labelled with random variables $\vec{U}$. The red dashed lines split the pulse sequence to individual segments with length $2k'$. The green dashed line further divides the segments into two halves ("left" and "right"). The random variables on the left side are correlated with corresponding ones on the right side, indicated by the blue lines. The distance between the correlated pairs is always k', and the covariance is $2R(k')$.

the distance between them is k'. We denote the left and right variables in the pair as U_i and $U_{i+k'}$. Conditioned on U_i, $U_{i+k'}$ is generated according to the following probability distribution:

$$\begin{aligned} P(U_{i+k'} = u | U_i = u) &= 1/2 + r, \\ P(U_{i+k'} = -u | U_i = u) &= 1/2 - r, \end{aligned} \tag{2.77}$$

for all $u \in \{1, -1\}$. As a result, the covariance between U_i and $U_{i+k'}$ is $2r$.

We assume that M is divisible by $2k'$, and the pulse sequence starts with a complete segment. When one averages over all choices of i (including those values of i where $i + k'$ no longer lies in the same segment as i), the averaged covariance between U_i and $U_{i+k'}$ is

$$\begin{aligned} R(k) &= \delta_{kk'} \, \mathbb{E}_i(U_i U_{i+k'}) \\ &= \delta_{kk'} \frac{2r \cdot M/2}{M - k'} \\ &= \delta_{kk'} \frac{M}{M - k'} r. \end{aligned} \tag{2.78}$$

Assuming $k' \ll M$, and substituting the result into Eq. (2.30), we have

$$\mathbb{E}(W(\omega)) = M\tau^2 \, \mathrm{sinc}^2(\tfrac{\omega\tau}{2})[1 + 2r\cos(k'\omega\tau)]. \tag{2.79}$$

In the compressed sensing scenario, we can simply set $r = 1/2$, which means that the paired variables take the same value. The expectation value of the window function is thus

$$\mathbb{E}(W(\omega)) = M\tau^2 \, \mathrm{sinc}^2(\tfrac{\omega\tau}{2})[1 + \cos(k'\omega\tau)], \tag{2.80}$$

which is perfect for compressed sensing (see Section 3). Compared to the general method, this

alternative method has a much simpler structure. In addition, those independent segments can be generated in parallel. This may be advantageous in the NISQ era where the hybrid quantum systems have limited memory resources.

The variance of this alternative method can be calculated easily. It can be considered as simplified version of the general one described in section 2.7.2, where the dependency graph G is of degree 1, i.e., $\tilde{\lambda} = 1$. Similar to the general model, we have

$$\frac{4\pi^2}{\tau^4}\text{Var}(\chi_U(T)) = \sum_{i\neq j, k\neq l} \Lambda_{ijkl} B_{ij}(S) B_{kl}(S). \tag{2.81}$$

The remaining cases of (i, j, k, l) that have a nonzero contribution to the sum are: Case 1, Case 2(b), Case 3(c) and Case 3(d). It can be calculated that

$$\text{Var}(\chi_U(T)) \leq \frac{4M\tau^3}{\pi} ||S(\omega)\,\text{sinc}^2(\tfrac{\omega\tau}{2}) - \langle S(\omega)\,\text{sinc}^2(\tfrac{\omega\tau}{2})\rangle||_{L2}^2. \tag{2.82}$$

2.9 Applications to 1-D Chain Mapping of Open Quantum Systems

In this section, we illustrate a direct application of random pulse sequences to efficient simulation of the short-time dynamics of an open quantum system, using the 1-D chain mapping technique [69]. Instead of trying to learn a complete description of the environment, we can use random pulses to extract just a few parameters that capture how the environment affects the qubit over short times. Those parameters let us replace the complicated bath with a simple one-dimensional chain model, whose first links encode the most important features. We then simulate the qubit interacting with this chain, using efficient numerical methods such as DMRG (density

matrix renormalization group). We find that even with only a handful of calibrated parameters, the predicted dynamics closely track the exact result.

First, we briefly review the 1-D chain mapping technique [69]. In the spin-boson model, the bath can be described by infinite number of bosonic modes, with the total Hamiltonian given by

$$H = H_{\text{system}} + H_{\text{bath}} + V_{\text{int}} = H_{\text{system}} + \int_{x_{\min}}^{x_{\max}} dx g(x) a_x^\dagger a_x + \int_{x_{\min}}^{x_{\max}} dx h(x) \hat{A}(a_x + a_x^\dagger) \quad (2.83)$$

where x is some continuous real variable, $g(x)$ represents the dispersion relation of the bath frequency to x, $\hat{A}$ is some operator on the system and $h(x)$ represents the coupling strength between the system and each mode. The spectral density is given by $S(\omega) = \pi h^2(g^{-1}(\omega))|\frac{dg^{-1}(\omega)}{d\omega}|$, which fully determines the dynamics induced in this open quantum system (OQS). This gives us freedom to choose the variable x as well as $g(x)$ and $h(x)$, as long as $S(\omega)$ does not change. Thus, by setting $g(x) = gx$, Eq. (2.83) can be written in a 1-D chain form as

$$\begin{aligned} H &= H_{\text{system}} + H'_{\text{bath}} + V' \\ &= H_{\text{system}} + g\sum_{n=0}^{\infty}(\sqrt{\beta_{n+1}} b_n^\dagger b_{n+1} + \sqrt{\beta_{n+1}} b_{n+1}^\dagger b_n + \alpha_n b_n^\dagger b_n) + ||\pi_0|| \hat{A}(b_0 + b_0^\dagger) \end{aligned} \quad (2.84)$$

where b_n are the transformed bosonic operators with $b_n^\dagger = \int_{x_{\min}}^{x_{\max}} dx U_n(x) a_x^\dagger$. The unitary operator $U_n(x)$ can be written in the form of a polynomial as $U_n(x) = h(x)\frac{\pi_n(x)}{||\pi_n||}$. The coefficients α_n, β_n together with π_n are defined recursively,

$$\begin{aligned} \pi_{n+1} = (x - \alpha_n)\pi_n - \beta_n \pi_{n-1}, \quad \pi_0 = 1, \quad \pi_1 = x - \langle x \rangle \\ \alpha_n = \frac{\langle x\pi_n, \pi_n \rangle}{\langle \pi_n, \pi_n \rangle}, \quad \beta_n = \frac{\langle \pi_n, \pi_n \rangle}{\langle \pi_{n-1}, \pi_{n-1} \rangle} \end{aligned} \quad (2.85)$$

where $\langle\cdot\rangle$ represents the integral with respect to the measure $\int_0^1 \cdot\, dx S(\omega_c x)/||S||$, normalized so that $\langle 1\rangle = 1$, and ω_c is the cutoff frequency. This recurrence procedure is known as "Stieltjes's procedure" [90].

Note that $\langle x\rangle$ can be seen as the 1st order moment of $S(\omega_c x)/||S||$. We can rewrite the coefficients in terms of central moments, $\mu_i = \langle (x - \langle x\rangle)^i\rangle$ for $i \neq 1$, where μ_1 is defined as the moment $\langle x\rangle$. For example,

$$
\begin{aligned}
&\pi_0 = 1, \quad \alpha_0 = \mu_1, \quad \beta_0 = 1,\\
&\pi_1 = x - \mu_1, \quad \alpha_1 = \mu_1 + \frac{\mu_3}{\mu_2}, \quad \beta_1 = \mu_2,\\
&\pi_2 = (x-\mu_1)^2 - \frac{\mu_3}{\mu_2}(x-\mu_1) - \mu_2,\\
&\alpha_2 = \mu_1 + \frac{\mu_5 - \frac{2\mu_3}{\mu_2}\mu_4 + (\frac{\mu_3^2}{\mu_2^2} - 2\mu_2)\mu_3 + 2\mu_3\mu_2 + \mu_2^2}{\mu_4 - \frac{\mu_3^2}{\mu_2} - \mu_2^2},\\
&\beta_2 = \mu_4 - \frac{\mu_3^2}{\mu_2^2} - \mu_2.
\end{aligned}
\tag{2.86}
$$

So the first few parameters can be characterized without knowing the whole spectrum if we can measure the first few central moments. This can be done, by a straightforward application of the random pulse sequences method developed in this chapter.

Usually, the noise spectrum of a physical bath belongs to the Szego class and the parameters will quickly converge ($\alpha_n \to 1/2, \sqrt{\beta_n} \to 1/4$). Thus, the short time dynamics of the spin system is determined by those central moments, which we can measure efficiently using the random pulse sequence method.

2.9.1 Numerical example

We start with a simple bath $S(\omega) = \lambda\omega\theta(\omega_c - \omega)$, where $\theta(\cdot)$ denotes the Heaviside step function. This is a special case of a power law, with a high-frequency cutoff ω_c [69]. Its exact chain-mapping parameters can be calculated using the shifted-Jacobi polynomials,

$$\begin{aligned} \alpha_n &= \frac{1}{2}(1 + \frac{1}{(1+2n)(3+2n)}), \\ \sqrt{\beta_n} &= \frac{(1+n)}{2(3+2n)}\sqrt{\frac{2+n}{1+n}}. \end{aligned} \tag{2.87}$$

The system Hamiltonian and the coupling term are set to be

$$H_{\text{system}} = E\sigma_z, \quad \hat{A} = (I + \sigma_4)/4 \tag{2.88}$$

We initialize a chain with a truncation length of 60, then apply time-dependent DMRG (t-DMRG) [91, 92] to simulate the coherence of the qubit over time. In Fig. 2.7, the purple line represents the result we get using the exact chain-mapping parameters.

In contrast, we can also initialize a homogeneous chain in which all the parameters are set to be constants ($\alpha_n = 1/2, \sqrt{\beta_n} = 1/4$ for all n), *with only the first m parameters measured by the random pulse sequences method,* and simulate the dynamics of those approximately-reconstructed chains using t-DMRG. Different colors in Fig. 2.7 represents the results of different numbers of parameters being measured. The simulated dynamics of the qubit rapidly converge to the exact case as m increases.

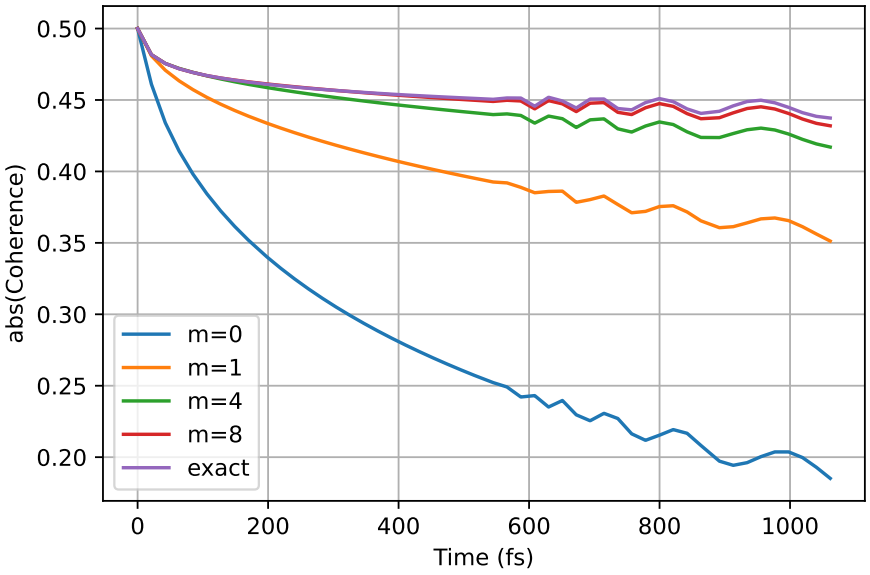


Figure 2.7: The t-DMRG simulation of the coherence of the qubit over time using the 1-D chain mapping technique, with m parameters measured by the random pulse sequences method. The purple line represents the t-DMRG simulation of the exact analytical chain, while other colors stand for the approximately-reconstructed chains with only m parameters measured by the random pulse sequences method.

Chapter 3: Compressed Sensing with Random Pulses

In chapter 2, we developed a general framework that has many possible applications. In this chapter, we apply that framework to demonstrate the efficient reconstruction of sparse noise spectra $S(\omega)$, using a combination of the random pulse sequences described above, and techniques from compressed sensing [31, 93]. This method is reminiscent of compressed sensing techniques used in NMR, though the domain where we apply these techiques (noise spectroscopy) is quite different [94, 95]. This method requires measurements of only $O(s \log n)$ linear functionals of $S(\omega)$, where s is the sparsity and n is the number of grid points in the frequency domain.

For a realistic physical system that has a sparse noise spectrum, self-assembled quantum dots [80, 96], numerical simulations show that this method can achieve an order of magnitude speedup, compared to conventional dynamical decoupling sequences. In addition, proof-of-concept demonstrations on commercially-available quantum information processors, using superconducting qubits and trapped ions, and synthetically generated noise with correlations that are much slower than the system dynamics [67, 68], show the practical feasibility of this approach.

3.1 Theory

A promising application of the random pulse method is the compressed sensing (CS) [31, 93] of sparse noise spectra. Let us approximate a noise spectrum by a function on a discrete set of N "grid points" in the frequency domain (call this subset G_N). We say the noise spectrum is s-sparse if it is nonzero at (at most) s points in G_N. As we show below, our method can use $O(s \log N)$ sets of random pulses to fully reconstruct an s-sparse spectrum, ideally providing an exponential speedup compared to $O(N)$ sets of experiments required by the CPMG protocol.

The main idea of the CS method is to choose a random set of Fourier basis functions, and then generate random pulse sequences whose window functions approximate these Fourier basis functions, in order to probe the noise spectrum. More precisely, we choose m random Fourier functions with frequencies $k_1, \ldots, k_m$. For each $a \in \{1, \ldots, m\}$, we define target functions $T_{k_a}(\omega) = \cos(k_a \omega \tau) \operatorname{sinc}^2(\frac{\omega\tau}{2})$, and we generate random pulse sequences with $R(j) = \frac{M}{2(M-k_a)} \delta(j - k_a)$. Using equations (2.47) and (2.49), these random pulse sequences have decay exponents χ_{k_a} that satisfy

$$\mathbb{E}(\chi_{k_a} - \chi_{\text{base}}) = M\tau^2 \int_{-\omega_c}^{\omega_c} S(\omega) \operatorname{sinc}^2(\tfrac{\omega\tau}{2}) \cos(k_a \omega \tau) d\omega. \tag{3.1}$$

We view this as a compressed sensing measurement of the function $S(\omega) \operatorname{sinc}^2(\frac{\omega\tau}{2})$, from which we can readily extract the noise spectrum $S(\omega)$. Note that $S(\omega) \operatorname{sinc}^2(\frac{\omega\tau}{2})$ has the same sparsity as $S(\omega)$, since $\operatorname{sinc}^2(\frac{\omega\tau}{2})$ varies mildly between $\frac{4}{\pi^2}$ and 1, when ω is in the interval $[-\frac{\pi}{\tau}, \frac{\pi}{\tau}]$. By the same token, estimating $S(\omega) \operatorname{sinc}^2(\frac{\omega\tau}{2})$ is equivalent to estimating $S(\omega)$, up to a small loss of precision.

According to the CS theory [31, 93], the discretized spectrum $S^* : G_N \to \mathbb{R}$ (where G_N is the set of grid points) can be recovered by solving a convex optimization problem. Given experimental measurements of $\chi^{\text{exp}}_{k_a}$ $(a = 1, \ldots, m)$ and $\chi^{\text{exp}}_{\text{base}}$, one can solve:

$$\begin{aligned} &\min_{S^*:\, G_N \to \mathbb{R}} ||S^*(\omega)\,\text{sinc}^2(\tfrac{\omega\tau}{2})||_{L_1}, \text{ subject to} \\ &\sum_{a=1}^{m} \left| \chi^{\text{exp}}_{k_a} - \chi^{\text{exp}}_{\text{base}} - \tfrac{2\omega_c M\tau^2}{N|G_N|} \sum_{\omega \in G_N} S^*(\omega)\,\text{sinc}^2(\tfrac{\omega\tau}{2})\cos(k_a\omega\tau) \right|^2 \leq \epsilon. \end{aligned} \tag{3.2}$$

Here, ϵ is chosen by the experimenter to allow for noise in the measurements of $\chi^{\text{exp}}_{k_a}$ and $\chi^{\text{exp}}_{\text{base}}$. The solution $S^*(\omega)$ to Eq. (4.4) is an accurate approximation of (the discretized approximation of) $S(\omega)$, when the number of generated Fourier functions satisfies $m \geq \Omega(s \log N)$. Rigorous error bounds for $S^*(\omega)$ can be derived using standard techniques from compressed sensing theory [93].

In practice, one may have prior information about the range of frequencies $[f_1, f_2]$ where noise will occur. In the above discussion, we have considered the special case where $f_1 = 0$. However, one can easily extend our method to the case where $f_1 > 0$, in the following way: First, one constructs random pulse sequences whose window functions are sinusoidal functions with wavelengths $(f_2 - f_1)/k$, for randomly chosen integers $k \in \{1, 2, 3, \ldots\}$. Then, when solving for the noise spectrum $S(\omega)$, one imposes constraints that specify the values of $S(\omega)$ for $\omega \in [0, f_1]$. Compressed sensing then works in the same way described above. When the range $[f_1, f_2]$ is large, compressed sensing is expected to outperform conventional CPMG pulse sequences.

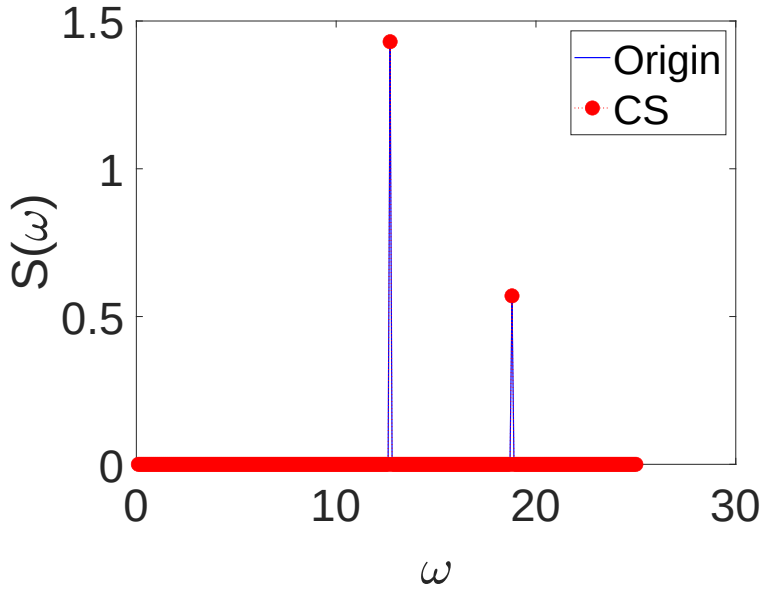
3.2 Numerical Examples

Fig. 3.1a presents a numerical simulation of the CS method on an ideal sparse spectrum. The solid blue line represents a 2-sparse spectrum with $N = 250$ grid points. The red circles represent the reconstructed spectrum, $S^*(\omega)$, obtained from CS with $m = 12$ different Fourier basis functions. By accurately identifying the non-zero elements of the original spectrum (blue line), the CS method (red circles) succeeeds in reconstructing it.

We further examine the accuracy of CS in reconstructing ideal spectra under different sparsities, s, as a function of the number of Fourier basis functions, m (Fig. 3.1b). These random spectra are generated in the following way. We initialize a vector of dimension N, with every coordinate equal to zero. Then we randomly pick s coordinates, where s is the prescribed sparsity. Next, we set the amplitudes of those chosen coordinates to be uniformly random in $[0, 1]$. Finally, we normalize the vector so that its ℓ_1 norm equals s. The average value of the peaks remains the same regardless of s, thus we can compare the accuracy of the CS method under different random spectra and different sparsities.

For each sparsity (different curves in Fig. 3.1b), we randomly generate 200 sparse spectra with $N = 250$ grid points to obtain the averaged accuracy. The accuracy is defined as the L_∞ norm of the difference between the discretized true spectrum, $S(\omega)$, and the reconstructed spectrum, $S^*(\omega)$. For each sparsity, the accuracy undergoes a clear phase transition at a certain value of m. We define m_c as the critical number of Fourier basis functions for which the accuracy reaches 0.5 (e.g., for $s = 13$, $m_c = 40$). It can be seen that m_c is a linear function of s (inset of Fig. 3.1b), which is consistent with the theoretically-predicted proportionality between m and $s \log N$.

(a)



(b)

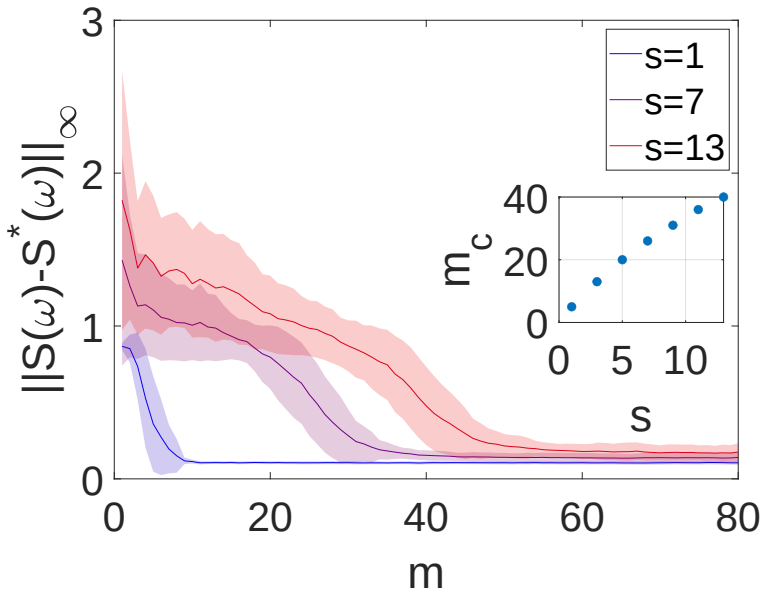


Figure 3.1: (a) A reconstruction of an ideal sparse spectrum using the CS method. The solid blue line represents a 2-sparse spectrum with $N = 250$ grid points. The red circles represent the decomposed spectrum using CS based on $m = 12$ different Fourier basis functions. For each Fourier basis function, we generate random pulse sequences with $(M, N_1, N_2) = (250, 1000, 50)$. (b) The accuracy of CS ($(M, N_1, N_2) = (250, 1000, 50)$) in reconstructing ideal spectra as a function of the number of Fourier basis functions. Different curves represent different sparsities s, considering 200 randomly generated spectra with $N = 250$, normalized so that the L_1 norm equals $0.1s$. Each simulation is repeated 100 times and the shaded areas represent the 95% confidence regime. Inset: The scaling of the critical number of Fourier basis functions, m_c, as a function of the sparsity of the spectrum.

3.3 Application to Quantum Dots

Next, to quantify the performance of the CS method for realistic physical systems, we explore the ability of the method to extract the spectral density of noise that interacts with InAs/GaAs quantum dots. This noise represents the decoherence of the quantum dots due to their hyperfine interaction with an ensemble of nuclear spins broadened by strain [80, 96]. The solid blue line in Fig. 3.2 shows the theoretical spectral density of such a noise source calculated from the Fourier transform of the autocorrelators of the fluctuating nuclear spins, while considering quantum dots of pure indium and arsenic at a temperature of 4 K and under a magnetic field of B = 2 T applied perpendicular to the growth direction of the dots (Voigt geometry) [96]. This spectrum consists of several narrow peaks at spectral frequencies that correspond to different Larmor frequencies of the nuclei.

The red dots in Fig. 3.2 represent the discrete spectrum obtained by simulating the performance of CS with $m = 40$ different Fourier basis functions. While the theoretical spectrum is not ideally sparse, we adopt suitable data analysis techniques (least absolute shrinkage and selection (LASSO) [97]), along with cross-validation (CV), see section 1.4.4) to successfully identify the centers of the major peaks.

We quantify the accuracy of extracting the InAs/GaAs noise spectrum by comparing the central frequencies of the largest three peaks obtained from CS to their theoretical values. The theoretical central frequencies, $\hat{\omega}^{\text{th}} = (\omega_1, \omega_2, \omega_3)$, are calculated by a Gaussian fitting to the theoretical spectrum. The experimental results, $\hat{\omega}^* = (\omega_1^*, \omega_2^*, \omega_3^*)$, are the weighted mean values of the frequencies from the neighboring non-zero discrete $S^*(\omega)$ obtained from CS. The reconstruction accuracy is defined as the ℓ_∞ norm of the difference between these two vectors, i.e.

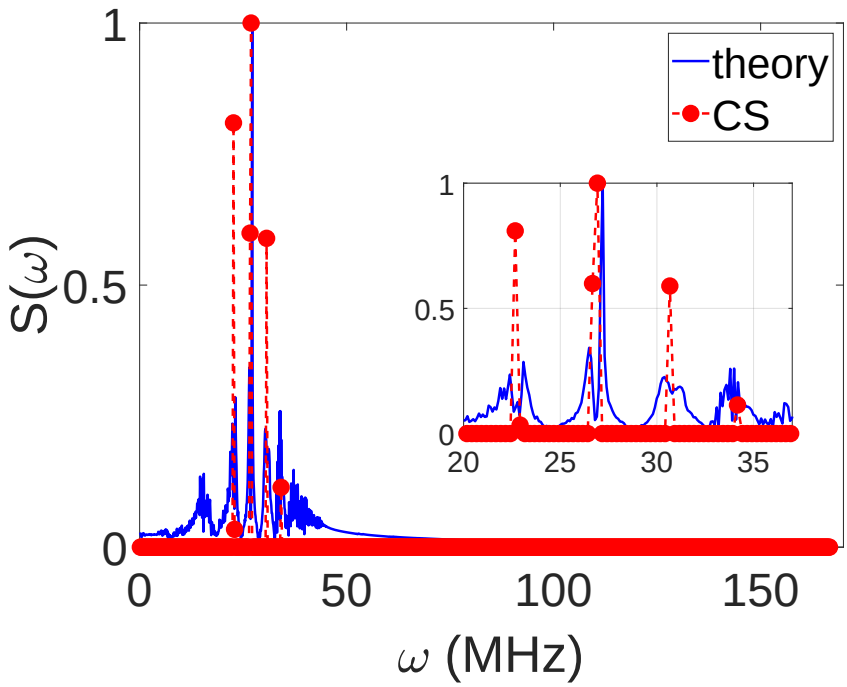


Figure 3.2: A reconstruction of the noise spectrum of an ensemble of nuclear spins interacting with an InAs/GaAs quantum dot (under an external magnetic field of B = 2 T at the Voigt geometry) using pulse sequences of compressed sensing. The blue solid line represents the theoretically simulated noise spectrum, with the maximum intensity normalized to 1. The red dots represent the simulated reconstructed spectrum considering random pulse sequences with $(M, N_1, N_2) = (200, 2000, 50)$ and $m = 40$ different Fourier basis functions. For the CS method, we estimate the spectrum using the LASSO, with $N = 667$ grid points and 10-fold cross validation, which successfully identifies the central frequencies of the major peaks.

$|\hat{\omega}^* - \hat{\omega}^{\text{th}}|_\infty$.

The solid blue line and the dashed red line in Fig. 3.3 represent the simulated reconstruction accuracies of CS with $N = 167$ and $N = 667$ grid points, respectively. In these simulations, we assume no experimental errors and only focus on the effect of the number of different sets of experiments, N_{set}. For CS, $N_{\text{set}} = m + 1$ for m Fourier basis functions and one additional experiment with the base random pulse sequence. For both choices of N, we observe a sharp change (phase transition) in the accuracy of reconstructing the spectrum at $N_{\text{set}} \approx 40$. The reconstruction accuracies then converge to constant values inversely proportional to N (e.g., the dashed red line

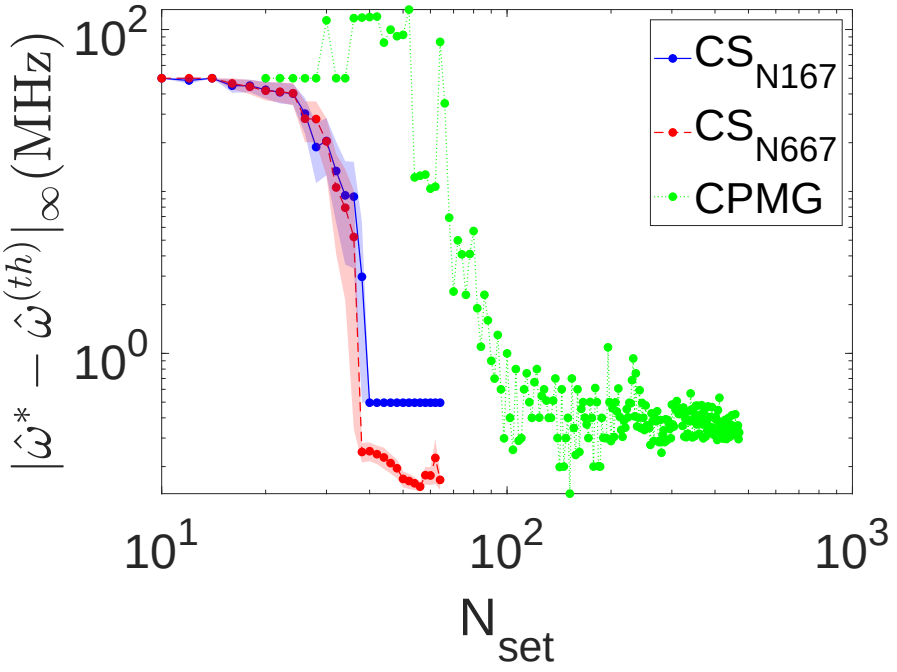


Figure 3.3: Numerical simulations of the accuracy of reconstructing the central frequencies of the InAs/GaAs noise spectrum as a function of the number of sets of experiments, N_{set}. The reconstruction accuracy, $|\hat{\omega}^* - \hat{\omega}^{\text{th}}|_\infty$, quantifies the deviation between the reconstructed frequencies and the theoretical ones for the three largest peaks. The solid blue line and the dashed red line represent the accuracy of CS with $N = 167$ and $N = 667$ grid points, respectively. The CS simulations are repeated for 30 times and the shaded areas represents the 95% confidence regimes. The dotted green line represents the reconstruction accuracy of the noise spectrum using the CPMG sequences. Achieving a certain accuracy by utilizing the CPMG sequences requires an order of magnitude more sets of experiments than by utilizing CS.

for $N = 667$ has a lower baseline than the solid blue line for $N = 167$). As a result, increasing the number of grid points N in post-processing could boost the spectral resolution of CS without adding any resources.

To further demonstrate the resource efficiency of the CS method, we compare the accuracies of CS in resolving the InAs/GaAs noise spectrum to the ones obtained by using the conventional CPMG method (dotted green line in Fig. 3.3). For CPMG, the number of sets of experiments required for noise spectroscopy is given by $N_{\text{set}} = 2\omega_c T/\pi$, i.e., the number of different sequences that probe the noise spectrum over the frequency range $[0, \omega_c]$ given the total experiment time, T [19–23, 61, 79, 80].

For $N_{\text{set}} < 100$, the CPMG sequences cannot resolve adjacent spectral peaks of the InAs/GaAs noise spectrum (i.e., $|\hat{\omega}^* - \hat{\omega}^{\text{th}}|_\infty > 1$), because the sampling frequency interval associated with the sequences is wider than the spectral distance between nearby peaks in the spectrum. Meanwhile, for $N_{\text{set}} > 100$, the CPMG protocol can resolve the desired spectrum, with accuracy inversely proportional to N_{set}. However, to achieve a certain level of accuracy, the CPMG sequences require at least an order of magnitude more resources than the CS method. For example, as we illustrate for the InAs/GaAs noise spectrum, $|\hat{\omega}^* - \hat{\omega}^{\text{th}}|_\infty \approx 0.2$ for CS dashed red line) with $N = 667$ grid points and $N_{\text{set}} \approx 40$; but this accuracy is hardly reached by CPMG (dotted green line) up to $N_{\text{set}} \approx 500$.

3.4 Experimental Demonstration

Finally, we demonstrate the compressed sensing technique on two experimental quantum devices. This provides evidence that our methods can be made robust to various imperfections

that occur in real experiments.

For example, in real experiments, the pulses are imperfect as they have finite pulse width and often contain some systematic error. Using our method, the effects of the finite pulse width will be felt equally across the frequency domain; whereas using CPMG pulse sequences, these effects will be worse at high frequencies and less harmful at low frequencies. It is not surprising that our method behaves this way, because our method works across a broad range of frequencies, i.e., it is a "broadband" measurement technique.

As for systematic errors like over-rotation or axis error, it is well known in the context of CPMG pulse sequences that these kinds of errors can be canceled out by using composite pulses [98]. The same technique can be applied to our random pulse sequences. In the following experiments, we apply robust $\pi\bar{\pi}$ pulse sequences (each π pulse followed by a $-\pi$ pulse).

The first device we examined is $ibmq_lima$, a superconducting quantum information processor built by IBM. We utilize the Schrodinger Wave Autoregressive Moving Average (SchWARMA) tools [67, 68] to inject noise (with a sparse noise spectrum) into the qubit. The solid blue line in Fig. 3.4a shows a random 2-sparse spectrum. Noise with this spectrum was generated using SchWARMA. The green squares represent the spectrum reconstructed from the CPMG method, plus a non-negative least squares fitting (NNLS). The CPMG process contains 64 sets of experiments on different frequencies, with each experiment repeated 5000 times ($(M, N_{\text{CPMG}}) = (64, 5000)$). The red circles represent the reconstructed spectrum obtained from CS with $m = 10$ different Fourier basis functions, each contains random pulse sequences with $(M, N_1, N_2) = (64, 100, 50)$. We also use LASSO and CV to analyze the data.

Compared to the CPMG method, the CS result captures the main peaks of the injected noise, while eliminating the background white noise caused by the gate and SPAM (state prepa-

ration and measurement) errors. This is as expected, because the random pulse sequences we used here were designed to search for sparse "pulse-like" features that resemble delta functions, rather than smoothly-varying background noise such as white noise or 1/f noise [1].

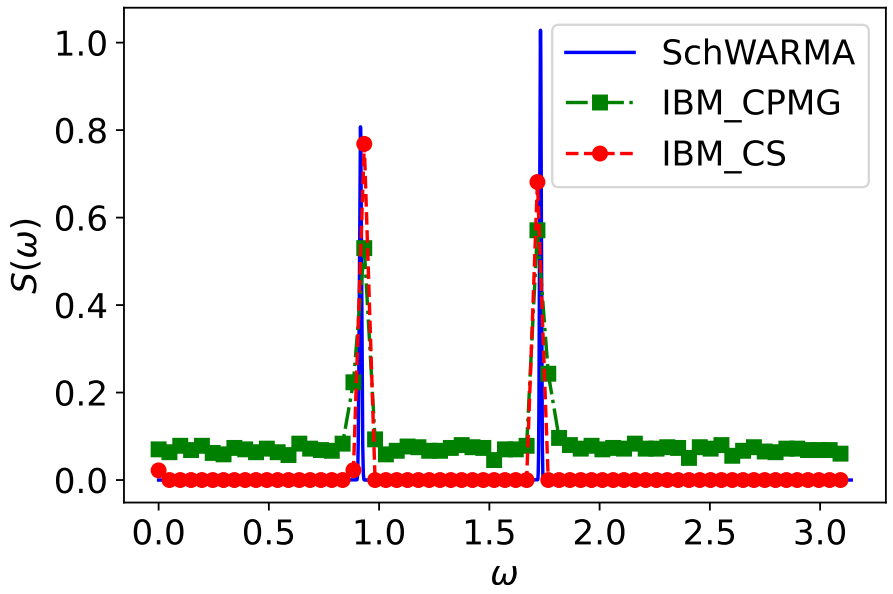
device	T_1	T_2	SPAM	Gate error	Gate time
$ibmq_lima$	109 μs	188 μs	0.66%	0.14%	305.77 ns
$ionq_harmony$	10 s	0.2 s	0.26%	0.15%	10 μs

Table 3.1: Properties of qubit 0 in $ibmq_lima$ and average performance in $ionq_harmony$ [99]. SPAM represents error associated with state preparation and measurement inaccuracies. Gate error represents averaged error rate occurring during the operation of single-qubit gates.

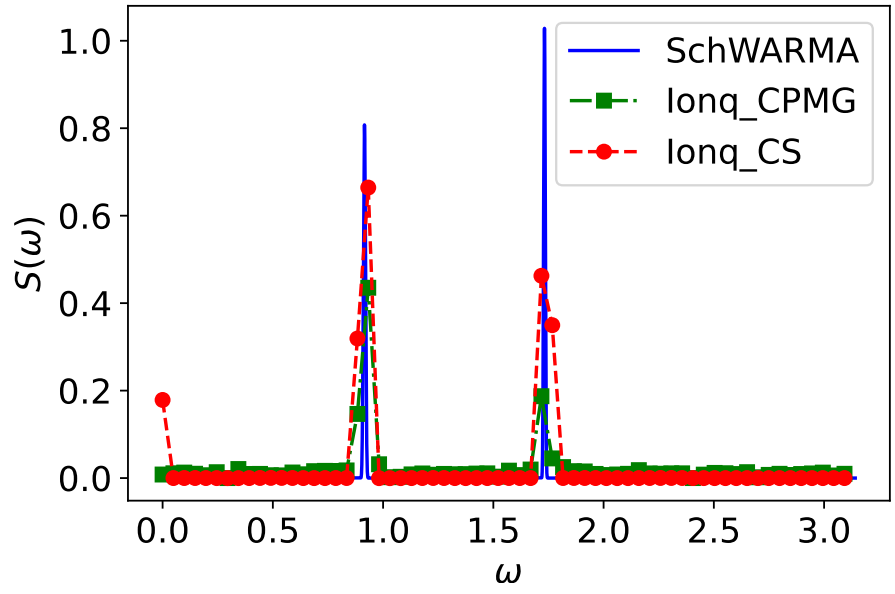
We also perform the same experiments on $ionq_harmony$, a trapped-ion quantum computing platform built by IonQ. The basic settings, including sets of experiments and numbers of pulse sequences, are exactly the same as the ones for $ibmq_lima$. The results are shown in Fig. 3.4b. The CS method again well captured the main peaks of the injected noises. Compared with the superconducting qubits result, the trapped ion experiments have less background noise in the CPMG, due to the smaller SPAM error rate (see table 3.1).

Similar to Fig. 3.3, we can further quantify the accuracy of the CS method on both platforms by comparing the central frequencies of the peaks obtained from CS to the actual values. The dashed red and blue lines in Fig. 3.5 represent the results for $ibmq_lima$ and $ionq_harmony$. It is interesting to see that the phase transition points of the accuracy are almost the same for both platforms, despite different hardware properties.

[1] In principle, it is possible to design random pulse sequences with window functions that are more suitable for parametric fitting of 1/f noise. It is an interesting question whether this approach could perform better than parametric fitting of 1/f noise using CPMG pulse sequences.



(a)



(b)

Figure 3.4: (a) A reconstruction of the (artificially generated) sparse noise spectrum on the superconducting qubit $ibmq_lima$. The blue solid line represents the ideal sparse spectrum we want to inject using SchWARMA, with maximum intensity normalized to 1. The green squares represent the CPMG (plus NNLS) result with 64 sets of experiments, each repeated 5000 times $((M, N_{\text{CPMG}}) = (64, 5000))$. The red circles represent the CS reconstruction with $m = 10$ different Fourier basis functions and random pulse sequences with $(M, N_1, N_2) = (64, 100, 50)$. (b) Same experiments performed on $ionq_harmony$.

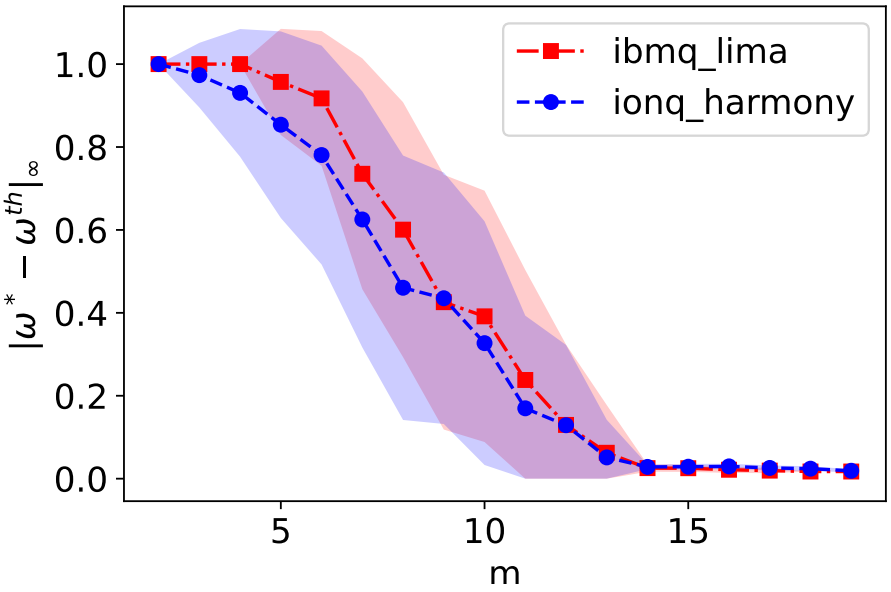


Figure 3.5: The accuracy of reconstructing the central frequencies of the injected noise spectrum on different platforms as a function of the number of sets of experiments. The dashed red and blue lines represent the results for $ibmq_lima$ and $ionq_harmony$, respectively. The shaded areas represent ± 1 standard deviation, averaged over 60 different choices of CS bases.

3.5 Outlook

To conclude, we develop a new method for qubit noise spectroscopy based on the realization of random pulse sequences. By using mathematical techniques for phase retrieval, this method allows us to measure arbitrary linear functionals of the noise spectrum. As an application, we demonstrate the reconstruction of sparse noise spectra, by using random pulse sequences together with compressed sensing (CS). Furthermore, the proposed method can be used to reconstruct noise spectra of realistic physical systems, such as optically-active quantum dots, with an order of magnitude less resources than conventional dynamical decoupling techniques.

While it may seem surprising that random pulse sequences can be used to implement such a large class of spectroscopic measurements, our results are consistent with recent findings on

the realization of optimal quantum control using switching pulse sequences [100]. These results suggest that optimal control and characterization of large numbers of qubits can be achieved using relatively simple control electronics (i.e., without resorting to arbitrary waveform generators).

For future research, our method can be generalized to incorporate pulses with durations other than π, and toward the characterization of multi-qubit systems [59]. In addition, while we have only considered the reconstruction of the noise spectrum on a finite set of sample points, similar ideas can be applied to reconstruction over continuous domains [101–103].

Finally, the accuracy of CS utilizing random pulse sequences strongly depends on the spectral properties of the probed noise source. Beyond the experimental realization of CS on the specific platform of InAs/GaAs quantum dots, it would be beneficial to study the performance of random pulse sequences on realistic noise sources with various spectral features. For example, our method can be used to probe noise spectra of NV centers in diamond, which consist of a sharp (sparse) peak due to the interaction with 13C nuclear spin as well as slow decaying components associated with a bath of P1 electronic spins [104].

The raw data that support the findings of this article are openly available [105]. Source codes are available upon reasonable request from the authors.

Chapter 4: Piecewise Linear Modeling and Rademacher Measurements

4.1 Introduction

Characterizing the spectral properties of environmental noise is essential for understanding and mitigating decoherence in quantum systems. In particular, the accurate reconstruction of the noise spectral density, $S(\omega)$, informs both noise-resilient control protocols and error mitigation strategies in quantum technologies [106–108]. Dynamical decoupling (DD) techniques enable indirect access to $S(\omega)$ by modulating a system's sensitivity to environmental fluctuations via tailored control sequences. However, conventional methods of DD often rely on coarse frequency resolution or assumptions of spectral smoothness, limiting their effectiveness in resolving structured and non-smooth features [19, 23, 24, 56, 58].

To improve the resolution and resource efficiency of noise spectroscopy, compressed sensing (CS) has emerged as a powerful framework for spectral reconstruction in quantum noise spectroscopy, particularly when the spectrum possesses sparse structure in a suitable representation [109, 110]. Recent work has introduced random pulse sequences as a tool for the direct measurement of arbitrary linear functionals of $S(\omega)$, enabling the CS reconstruction of sharp spectral peaks with significantly fewer measurements [17].

While this approach is effective for perfectly sparse spectra, it leaves two key challenges unresolved: can this method be applied to a larger class of noise spectra that are not perfectly

sparse, and can the practical difficulty of applying the desired random pulse sequences in an experiment be reduced? This paper addresses both of these challenges separately.

First, many realistic noise processes, including charge and magnetic noise in solid-state qubits, exhibit more complicated spectral features rather than sparse peaks represented by simple delta functions [80, 96]. For example, the spectra of quantum dot systems often combine narrow resonances with broad, slowly varying backgrounds. This motivates the need for models that retain sparsity while capturing richer structures. Piecewise-linear, and more generally piecewise-polynomial, functions provide such a representation.

In this work, we develop a CS protocol for reconstructing piecewise-linear noise spectra by enforcing sparsity on the second derivative $S''(\omega)$. Specifically, we apply an L_1-norm regularization on $S''(\omega)$, which promotes reconstructions that are globally continuous but exhibit sparse curvatures. This approach aligns with recent advances in total generalized variation (TGV) [111–113] and higher-order sparse regularization techniques for inverse problems [114, 115]. It can also be viewed as an extension of previous work on compressed sensing, for piecewise-constant images in two dimensions, based on regularization using the total variation (TV) norm [41–44].

Our method extends this to the problem of compressed sensing of a piecewise-linear function using TGV regularization, in one dimension. This particular setting appears to be more challenging from a theoretical perspective, and beyond the scope of the above works. Nonetheless, our numerical simulations on simulated spectra with varying degrees of piecewise-linearity demonstrate high-fidelity reconstructions.

Second, we consider the experimental implementation of random pulse sequences, which can be resource-intensive. In particular, previous work proposed the use of random pulse sequences with complex, long-range correlations, which are difficult to generate in real time. In-

stead, the entire pulse sequence typically had to be generated "offline," using a desktop computer, then transferred to an arbitrary waveform generator (AWG), before being applied to a physical qubit. The loading and storage of a great number of different pulse sequences creates a bottleneck in experiments.

To address this, we introduce a simplified variant of the method, using uncorrelated random pulses, which we call Rademacher measurements. These pulse sequences are easier to generate in real time, so that the entire pulse sequence never has to be stored in memory. In this scheme, the total evolution time is divided into equal segments indexed by $m = 1, 2, \ldots, M$, each time segment is assigned a Rademacher random variable U_m (i.e., an independent random variable that takes on the values 1 and -1 with equal probability), and rotation π-pulses are applied whenever $U_{m+1} \neq U_m$.

Because these pulse sequences have no correlations, it is easy to generate them on-the-fly, using a short random seed and a pseudorandom number generator; thus they can be generated in real time using a field-programmable gate array (FPGA), without any need for an AWG. Despite their simplicity, we show via simulations that Rademacher measurements retain the same compressed-sensing efficiency as Fourier-based random pulses [17] while substantially reducing experimental complexity.

Finally, we extend our investigation to realistic physical systems, focusing on the noise spectra of self-assembled quantum dots [80]. We demonstrate the efficiency of the TGV-based CS method, combine it with the Rademacher measurements technique, and demonstrate its potential for rapidly reconstructing realistic noise spectra. We also explore modifications of the protocol that further reduce the number of control pulses without significant loss in reconstruction accuracy. These results broaden the applicability of random-pulse-based noise spectroscopy

and improve its practicality for near-term quantum devices.

The remainder of this chapter is organized as follows. The basic model and background are introduced in section 4.2. The two main results of the paper are discussed in detail in section 4.3 and section 4.4. We then verify our results by simulations on realistic systems in section 4.5. We conclude with a summary and a discussion of open problems in Section 4.6.

4.2 Model

Similar to previous chapters, we consider a single qubit subject to pure dephasing due to coupling with a stationary bath. Equation (2.14) provides a pathway for estimating the spectrum of a noisy environment via linear inversion. We apply a set of m control sequences on the system, then measure the corresponding survival probabilities P_k, $k = 1, \ldots, K$. For each k, one obtains estimates of $\chi_k = -\log(2P_k - 1)$. To make the inversion tractable, we discretize the frequency axis at N points $\{\omega_n\}$, leading to the approximation

$$\chi_k = \sum_{n=1}^{N} F_k(\omega_n) S(\omega_n) + \epsilon_k. \tag{4.1}$$

Here ϵ_k represents the error in the k-th measurement. In matrix form, Eq. (4.1) becomes

$$\boldsymbol{\chi} = \mathbf{F}\mathbf{S} + \boldsymbol{\epsilon}, \tag{4.2}$$

where $\boldsymbol{\chi} \in \mathbb{R}^K$ contains the measured decay exponents, $\mathbf{F} \in \mathbb{R}^{K \times N}$ encodes the filter functions, and $\mathbf{S} \in \mathbb{R}^N$ represents the discretized noise spectrum. The estimation of $\mathbf{S}$ then reduces to solving a linear regression problem.

A common way to solve this problem is to apply the Carr-Purcell-Meiboom-Gill (CPMG) pulse sequence with evenly spaced rotation π pulses, whose filter function is approximately the Dirac δ-function. One can then solve Eq. (4.2) via nonnegative least squares (NNLS) or other deconvolution methods [17]. Intuitively, each CPMG sequence captures a narrow range of the spectrum, and one needs to apply many sequences to cover all frequency ranges. As a result, the number of measurements needed, K, is of the same order as the discrete number in the frequency domain, N. However, such numerous measurements are not always necessary for extracting noise spectra with some prior knowledge. For example, we may know *a priori* that the spectrum we are investigating has some sparse structure in a suitable representation [109, 110].

Recent studies have shown that the random pulse sequence method [17] and the CS method [31, 93] can be used to greatly speed up the reconstruction of sparse spectra. By generating random pulse sequences whose filter functions are Fourier basis functions, the number of measurements needed, K, is reduced from $O(N)$ to $O(s \log N)$, where s is the sparsity of $\mathbf{S}$.

However, the previous approaches are only capable of fully reconstructing ideal sparse spectra with Dirac δ function shapes. For realistic spectra with more complicated shapes, one could only detect the centers of the peaks, and not a complete characterization of their shapes [17]. In addition, for each measurement of the decay exponent, we need to generate a set of different random pulse sequences and load them into the experimental control system. This loading procedure could be time-consuming on current quantum computing platforms.

To solve the above limitations of the random pulse sequences method, we will advance this method in two complementary directions. We first extend the random pulse sequences method to piecewise linear spectra, and demonstrate the efficiency of the method through numerical simulations. Next, we introduce a simplified variant of the random pulse sequences method using

Rademacher measurements, which greatly reduces experimental complexity for sparse spectra.

4.3 Estimation of Piecewise Linear Spectra

In this section, we show how random pulse sequences can be adapted to estimate piecewise linear noise spectra. Following [17], we generate random pulse sequences with total time T and M equal segments, such that $T = M\tau$. Here τ is the minimum time between two consecutive pulses in the sequence, and we choose $\tau \ll 1/\omega_c$, where ω_c is the high-frequency cutoff of the noise spectrum $S(\omega)$. The filter functions of those sequences can be set to approximate the Fourier basis functions,

$$F_k(\omega_n) \propto \cos(j_k \omega_n \tau). \tag{4.3}$$

Here, j_k is a random integer chosen between $[0, M]$. If we assume that $S(\omega_n)$ is sparse with at most s nonzero points, the discretized spectrum $\mathbf{S}^* : G_N \to \mathbb{R}$ (where G_N is the set of grid points) can then be recovered by solving a convex optimization problem,

$$\mathbf{S}^* = \underset{\mathbf{S}:G_N\to\mathbb{R}}{\arg\min} \left(\|\boldsymbol{\chi} - \mathbf{F}\mathbf{S}\|_{L_2}^2 + \lambda \|\mathbf{S}\|_{L_1} \right). \tag{4.4}$$

λ can be optimized via the cross-validation method. The solution $\mathbf{S}^*$ to Eq. (4.4) is an accurate approximation of $\mathbf{S}$ if the number of generated Fourier functions satisfies $K \geq \Omega(s \log N)$.

We then generalize the result to noise spectra that are piecewise linear. This class of functions appears in various physical systems, where the underlying noise processes vary smoothly within frequency bands, but exhibit kinks or discontinuities at a few locations. A prototypical example includes Lorentzian kinks with $1/f$ noise background regularized at high and low

frequencies, or engineered environments with structured frequency response [67, 68]. The classification of a spectrum as piecewise linear is useful because the *second-order derivative* is still sparse, which allows us to perform CS.

We define the second-order discrete difference operator $\mathbf{D}^2 \in \mathbb{R}^{(N-2)\times N}$ as

$$(\mathbf{D}^2\mathbf{S})_n = S_{n+2} - 2S_{n+1} + S_n, \quad 1 \le n \le N-2. \tag{4.5}$$

This operator acts as a discrete Laplacian and evaluates local curvature; for a piecewise linear function, $\mathbf{D}^2\mathbf{S}$ is sparse, with nonzero entries only at the discontinuity points of the slope. Note that the cosine functions are the eigenfunctions of the discrete Laplacian operator, hence we have

$$\sum_{n=1}^{N} F_k(\omega_n)S(\omega_n) \approx \frac{1}{(j_k\tau)^2}\sum_{n=1}^{N} F_k(\omega_n)\mathbf{D}^2 S(\omega_n). \tag{4.6}$$

We define $\Delta = \mathbf{D}^2\mathbf{S}$ as the second order derivatives of the spectrum. As a result, similar to problem (4.4), we are guaranteed to recover Δ by solving the following optimization problem:

$$\Delta^* = \underset{\Delta: G_N \to \mathbb{R}}{\arg\min} \left(\|\boldsymbol{\chi}^* - \mathbf{F}\Delta\|_{L_2}^2 + \lambda \|\Delta\|_{L_1} \right), \tag{4.7}$$

where $\boldsymbol{\chi}^* = ((j_1\tau)^2\chi_1, \ldots, (j_K\tau)^2\chi_K)$. We define s^* as the sparsity in Δ. Intuitively, s^* equals the number of kinks in the spectrum. The solution Δ^* to Eq. (4.7) is again exact when the number of generated Fourier functions satisfies $K \ge \Omega(s^* \log N)$. One may then reconstruct $\mathbf{S}$ by double integration (solving $\mathbf{D}^2\mathbf{S} = \Delta^*$) with boundary constraints (e.g., $S_1 = S_N = 0$, or by low-frequency anchors).

However, the above procedure can be numerically unstable: it can amplify low-frequency

noise, and accumulate error when integrating $\mathbf{D}^2\mathbf{S}^*$. In practice, we can solve a one-step convex problem that directly estimates $\mathbf{S}$ while promoting second-order sparsity:

$$\mathbf{S}^* = \underset{\mathbf{S}:G_N\to\mathbb{R}}{\arg\min} \left(\|\boldsymbol{\chi} - \mathbf{F}\mathbf{S}\|_{L_2}^2 + \lambda \|\mathbf{D}^2\mathbf{S}\|_{L_1} \right). \tag{4.8}$$

Equation (4.8) can also be viewed as a second order TGV-regularized [111] optimization problem.

While first-order TGV enjoys mature, sharp error bounds with Fourier sampling [41–44, 116, 117], the second-order case lacks equally general bounds in our setting. However, studies have shown that the second order TGV can be applied for signal reconstruction with undersampled discrete Fourier measurements, and yields results that are superior to conventional methods [112, 118]. In this work, we show through simulations on piecewise linear spectra that problem (4.8) can be solved efficiently, and produces accurate reconstructions of $\mathbf{S}$.

Figure 4.1a shows a numerical example demonstrating the effectiveness of CS with 2nd order TGV penalty (CS_{TGV}) in reconstructing an ideal piecewise linear spectrum. The true spectrum, which is 4-sparse in the second-order difference domain over $N = 100$ grid points, is represented as a solid blue curve. The spectrum recovered from CS_{TGV} is shown as red circles and is obtained using only $K = 20$ random Fourier basis measurements. For each Fourier basis, we generate $N_1 = 100$ different random pulse sequences with each individual sequence repeated $N_2 = 50$ times. The reconstruction closely aligns with the original signal, confirming that CS_{TGV} is capable of accurately recovering the spectrum structure with far fewer samples than grid points.

To further investigate the performance of CS_{TGV}, we assess its reconstruction accuracy across various levels of second-order sparsity, s^*, as a function of the number of Fourier basis measurements, K, as illustrated in Fig. 4.1b. For each sparsity [different dotted lines in Fig. 4.1b],

we generate 100 random piecewise linear spectra with fixed norm, each with $N = 100$ grid points, to obtain the averaged accuracy. The accuracy is quantified as the L_2 norm of the difference between the discrete true spectrum, $S(\omega)$, and the CS estimate $S^*(\omega)$. For each sparsity, the accuracy increases sharply as K increases, revealing the potential of CS_{TGV} to fast reconstruct piecewise linear spectra.

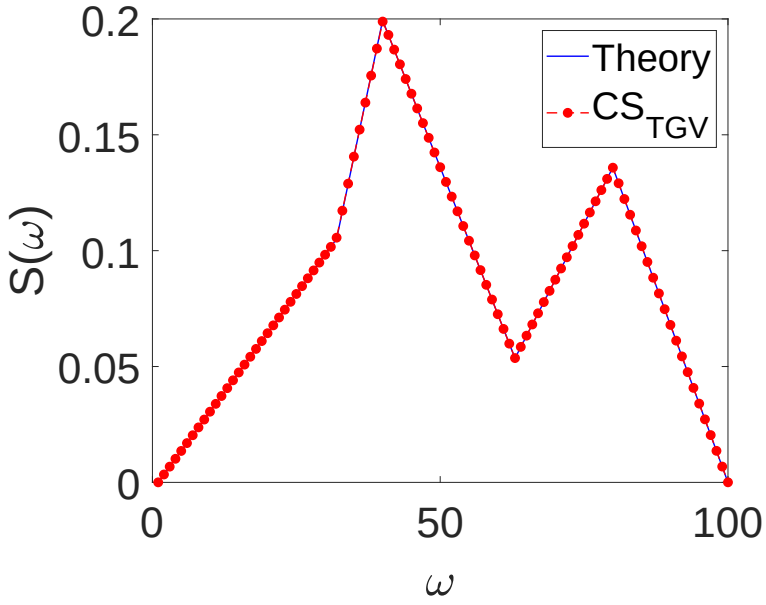
4.4 Rademacher Measurements for Sparse Spectra

In the previous section, we described improvements to the numerical algorithms for reconstructing sparse and piecewise-linear noise spectra. Now we turn our attention to different classes of random pulse sequences that can be used for CS. In this section, we will demonstrate a new way of reconstructing sparse noise spectra using Rademacher random pulse sequences and CS.

This new class of random pulse sequences is much simpler compared to the previous work [17], as it only contains uncorrelated π-pulses. Specifically, we assign a sequence of Rademacher random variables (sampled independently and uniformly from $\{1, -1\}$), denoted $\vec{U} = (U_1, \ldots, U_M) \in \{1, -1\}^M$, to the M segments of the total experimental time T. In other words, the probability that $U_m = 1$ is $p = 0.5$ and so is the probability that we generate a π-pulse in between the time segments. (In the same way as before, we write $T = M\tau$, and we assume $\tau \ll 1/\omega_c$, where ω_c is the high-frequency cutoff of the noise spectrum $S(\omega)$.)

Different from the previous approach, the random pulses are completely uncorrelated, and the Rademacher measurements do not involve the averaging of the filter function over many independent realizations of $\vec{U}$, but rather focus on the specific filter function of each individual

(a)



(b)

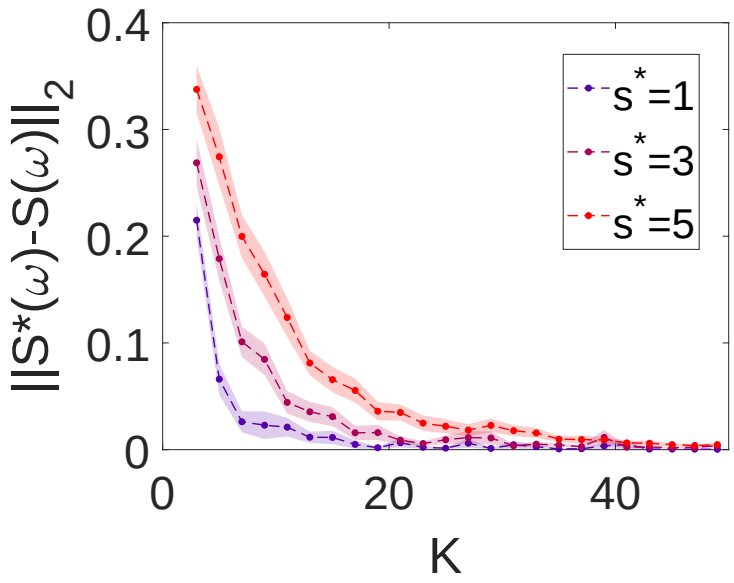


Figure 4.1: (a) A reconstruction of an ideal piecewise linear spectrum using the CS_{TGV} method. The solid blue line represents a randomly generated spectrum with $N = 100$ grid points. This spectrum is 4-sparse in its 2nd order derivatives. The red line represent the decomposed spectrum using CS_{TGV} based on $K = 20$ different Fourier basis functions. For each Fourier basis function, we generate random pulse sequences with $(M, N_1, N_2) = (100, 100, 50)$. (b) The accuracy of CS_{TGV} ($(M, N_1, N_2) = (100, 100, 50)$) in reconstructing ideal spectra as a function of the number of Fourier basis functions. Different curves represent different sparsities s in the 2nd order derivatives, considering 40 randomly generated spectra with $N = 100$, normalized so that the L_2 norm equals 1. Each simulation is repeated 100 times and the shaded areas represent the 95% confidence regime.

$\vec{U}$, such that

$$\begin{aligned} F_k(\omega) &= \tau^2 \operatorname{sinc}^2(\tfrac{\omega\tau}{2}) \Big| \sum_{m=1}^{M} U_m e^{i\omega m\tau} \Big|^2 \\ &= \tau^2 \operatorname{sinc}^2(\tfrac{\omega\tau}{2}) \vec{U}^T A(\omega) \vec{U}, \end{aligned} \tag{4.9}$$

where we define the matrix $A(\omega) \in \mathbb{C}^{M\times M}$ whose (m, m') entry is

$$A_{m,m'}(\omega) = e^{i\omega(m-m')\tau}. \tag{4.10}$$

We can further define the matrix $B(S) \in \mathbb{R}^{M\times M}$ whose (m, m') entry is

$$B_{m,m'}(S) = \hat{S}_{m-m'} \equiv \int_{-\pi/\tau}^{\pi/\tau} d\omega S(\omega) \operatorname{sinc}^2(\tfrac{\omega\tau}{2}) A_{m,m'}(\omega) \tag{4.11}$$

where $\hat{S}_{m-m'}$ is equal to the $(m-m')$'th coefficient of the Fourier series expansion of $S(\omega)\operatorname{sinc}^2(\frac{\omega\tau}{2})$. We find that $B(S)$ is a Toeplitz matrix, in which each descending diagonal from left to right is constant. The eigenvalues of $B(S)$ equal $M\mathbf{S}' : G_M \to \mathbb{R}$, which is the discretized spectrum of $MS(\omega)\operatorname{sinc}^2(\frac{\omega\tau}{2})$ on M grid points.

Then we can rewrite Eq. (4.2) as a linear operator $\boldsymbol{A}(B) : \mathbb{R}^{M\times M} \to \mathbb{R}^K$ that maps $B(S) \in \mathbb{R}^{M\times M}$ to $\boldsymbol{\chi} \in \mathbb{R}^K$:

$$\boldsymbol{\chi} = \boldsymbol{A}(B(S)) = \frac{\tau^2}{2\pi} \mathbf{U}^T B(S) \mathbf{U} + \boldsymbol{\epsilon}. \tag{4.12}$$

Here $\mathbf{U} \in \{1, -1\}^{K\times M}$ encodes K sets of Rademacher sequences.

Similarly to the previous CS scenario, if we assume that $\mathbf{S}'$ is sparse with sparsity s, the

Toeplitz matrix $B(S)$ is also of low rank s. Thus, the estimation of $\mathbf{S}'$ is equivalent to the recovery of the low-rank matrix $B(S)$:

$$B^* = \underset{B\in\mathbb{R}^{M\times M}, B \text{ is Toeplitz}}{\arg\min} \left(||\boldsymbol{\chi} - \boldsymbol{A}(B)||_{L_2}^2 + \lambda ||B||_* \right). \tag{4.13}$$

Here $||\cdot||_*$ represents the nuclear norm of the matrix.

Using recent theoretical results on recovery of low-rank Toeplitz matrices [47], we show that this problem can be solved accurately if $K \geq \Omega(s \log^2 M)$.

Theorem 3 *[47] Let $||\boldsymbol{\epsilon}||_2 \leq \eta$. With probability exceeding $1 - e^{-cK}$, the solution B^* to Eq. (4.13) satisfies*

$$||B^* - B||_F \leq C \frac{\eta}{K^{1/2}}, \tag{4.14}$$

where this bound holds simultaneously for all symmetric Toeplitz matrices B of rank at most s, provided that $K > Ls \log^2 M$. Here c, C and L are some numerical constants.

In realistic physical systems, the noise spectrum $S(\omega)$ is non-negative, and so is $\mathbf{S}'$. As such, we have

$$||B(S)||_* \propto ||\mathbf{S}'||_{L_1} \approx ||\mathbf{S}||_{L_1} \tag{4.15}$$

The problem in Eq. (4.13) can then be rewritten in the same form as in the previous section.

$$\mathbf{S}^* = \underset{\mathbf{S}:G_N\to\mathbb{R}}{\arg\min} \left(\|\boldsymbol{\chi} - \mathbf{F}\mathbf{S}\|_{L_2}^2 + \lambda \|\mathbf{S}\|_{L_1} \right). \tag{4.16}$$

Since both B and B^* are Toeplitz and diagonal in the Fourier basis, we have

$$||B^* - B||_F = M||S^* \operatorname{sinc}^2(\tfrac{\omega\tau}{2}) - S \operatorname{sinc}^2(\tfrac{\omega\tau}{2})||_2. \tag{4.17}$$

In practice, we can set the number of grid points $N = M$. Thus, substituting Eq. 4.17 into theorem 3, we get that with probability exceeding $1 - e^{-cK}$, the solution S^* to Eq. (4.16) satisfies

$$||S^* - S||_2 \leq C\frac{\eta}{NK^{1/2}}. \tag{4.18}$$

Provided that $K > Ls \log^2 N$, c, C and L are some numerical constants.

As a result, despite using a different measurement setup (with uncorrelated random pulses), and a different mathematical formulation (low-rank Toeplitz matrix recovery), we arrive at a place which is reassuringly familiar: we can still use the same CS algorithms as before to reconstruct sparse noise spectra efficiently. We denote this CS method combined with Rademacher measurements as CS_R later on.

Figure 4.2a presents a simulation that shows the efficiency of the Rademacher measurements technique. The solid blue line depicts the true spectrum, a 4-sparse signal defined over $N = 100$ grid points. Using only $K = 20$ random Rademacher measurements, the CS_R method accurately reconstructs the spectrum, shown as red circles.

We then investigate the accuracy of this new method as a function of the number of Rademacher sequences, K, in Fig. 4.2b. For each value of the sparsity, s, we generate 100 random spectra with a constant norm, each with $N = 100$ grid points, and compute the average reconstruction error. We again quantify the accuracy using the L_2 distance between the discrete true spectrum,

$S(\omega)$, and the CS_R estimate $S^*(\omega)$. Each dotted line in Fig. 4.2b exhibits a distinct phase transition: as K increases, the error drops sharply around a threshold value. We define this threshold K_c as the minimum number of basis functions needed for the reconstruction error to fall below 0.5. For example, $K_c = 9$ when $s = 3$.

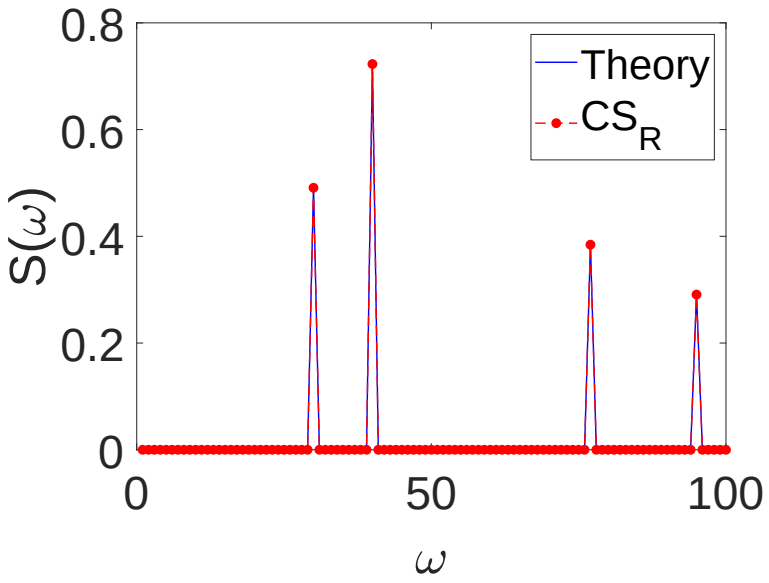
Figure 4.3 is similar to the simulations in Fig. 4.2b, in which we draw the accuracy of CS_R in reconstructing ideal sparse spectra as functions of K. Different dotted lines (with different colors) represent simulations with different grid numbers, N. For each value of N, we fix the sparsity $s = 2$, and generate 100 random spectra (again with fixed norm) to compute the averaged results. The distinct phase transition of the accuracy can be obtained as K increases. As shown in the inset of Fig. 4.2b and 4.3, K_c scales linearly with s and quadratically with $\log N$, in agreement with the theoretical prediction that $K \sim s^* \log^2 N$.

4.5 Applications

4.5.1 Quantum Dots

Next, to quantify the performance of our new methods for realistic physical systems, we examine their ability to reconstruct the spectral density of noise that interacts with InAs/GaAs quantum dots. This type of noise arises from decoherence mechanisms due to hyperfine interactions between the electron spin and a surrounding ensemble of nuclear spins broadened by strain [80, 96]. The solid blue line in Fig. 4.4a shows the theoretical noise spectral density, computed by taking the Fourier transform of the autocorrelation functions of fluctuating nuclear spin dynamics. The simulation assumes quantum dots composed of pure indium and arsenic, maintained at a temperature of 4 K and subjected to a magnetic field of $B = 2$ T applied perpendicular to

(a)



(b)

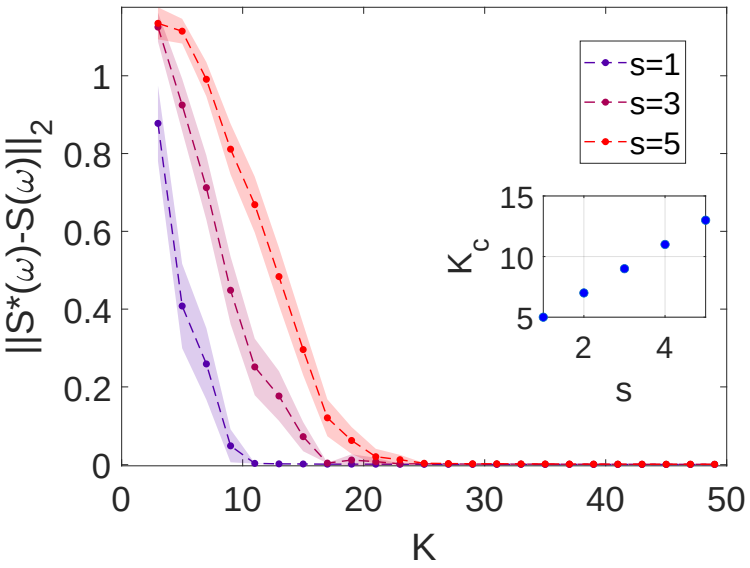


Figure 4.2: (a) A reconstruction of an ideal sparse spectrum using the Rademacher measurements based CS method. The solid blue line represents a randomly generated spectrum with $N = 100$ grid points. This spectrum is 4-sparse. The red line represent the decomposed spectrum using CS_R based on $K = 20$ different Rademacher sequences, with each repeated for 5000 times. (b) The accuracy of CS_R in reconstructing ideal spectra as a function of sets of Rademacher sequences. Different dotted lines represent different sparsities s, considering 100 randomly generated spectra with $N = 100$. In (b), each simulation is repeated 100 times and the shaded areas represent the 95% confidence regime.

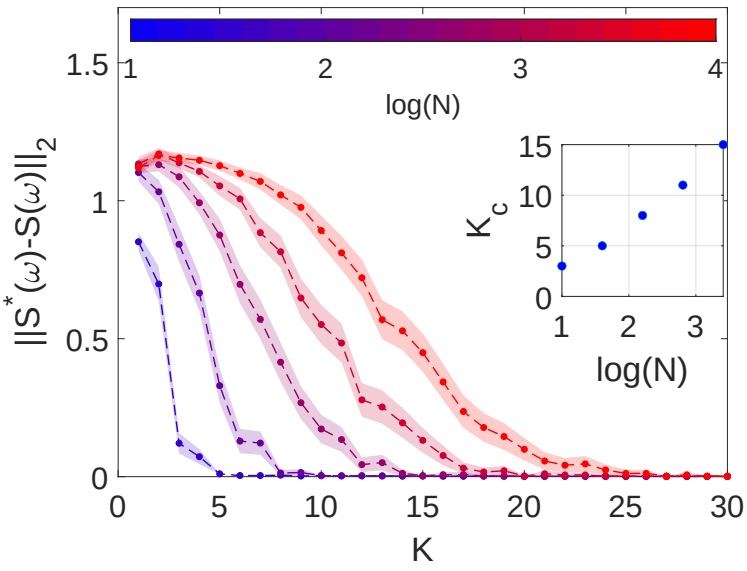


Figure 4.3: (c) The accuracy of CS_R as a function of sets of sequences. Different dotted lines (with different colors) represent different grid numbers, N, representing in the logarithm scale. Each dot contains the simulation of 100 random spectra. Inset: The scaling of the critical number of Rademacher measurements, K_c, as a function of the logarithm of the grid numbers, $\log(N)$. In (c), each simulation is repeated 100 times and the shaded areas represent the 95% confidence regime.

the growth axis (Voigt geometry) [96]. This spectrum features several narrow resonances corresponding to distinct nuclear Larmor precession frequencies.

First, we demonstrate the recovery of piecewise-linear approximations of this noise spectrum, using the technique from Section 4.3. The red dotted line in Fig. 4.4a shows the discretized spectrum reconstructed using the CS_{TGV} method with $K = 70$ randomly chosen Fourier basis functions. The reconstruction successfully recovers both the positions and shapes of the narrow peaks, as well as the slowly decaying broadband background, demonstrating the method's effectiveness in capturing realistic spectral features with limited measurements. In contrast, the previous method only provides the positions of peaks.

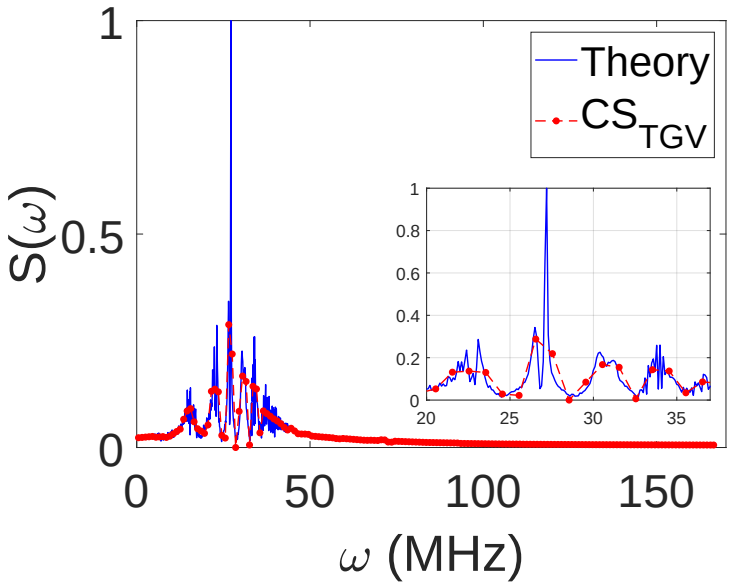
Note that the noise spectrum of the previously introduced InAs/GaAs quantum dot system can also be approximated by a sparse function (albeit with poorer accuracy and sparsity, than the piecewise-linear approximation). So, we can again use it to test the new Rademacher random pulse sequences method of Section 4.4. Inspired by the previous section, we modify the Lagrangian in Eq. (4.16) by adding a penalty term on the discrete Laplacian of $\mathbf{S}$:

$$\mathbf{S}^* = \underset{\mathbf{S}:G_N\to\mathbb{R}}{\arg\min} \left(||\boldsymbol{\chi} - \mathbf{F}\mathbf{S}||_{L_2}^2 + \lambda_1 ||\mathbf{S}||_{L_1} + \lambda_2 ||D^2\mathbf{S}||_{L_1} \right). \tag{4.19}$$

Equation (4.19) is a combination of the TGV and Rademacher measurements ($\text{CS}_{\text{R+TGV}}$). As is shown in Sec. 4.3, the second order TGV penalty term restricts the recovered spectrum to be piecewise linear, thus revealing more details than a simple sparse signal recovery.

Figure 4.4b shows the discretized spectrum (red dots) reconstructed by $\text{CS}_{\text{R+TGV}}$ from $K = 90$ randomly chosen Rademacher sequences. The method accurately recovers the narrow peaks and the slowly decaying broadband background.

(a)



(b)

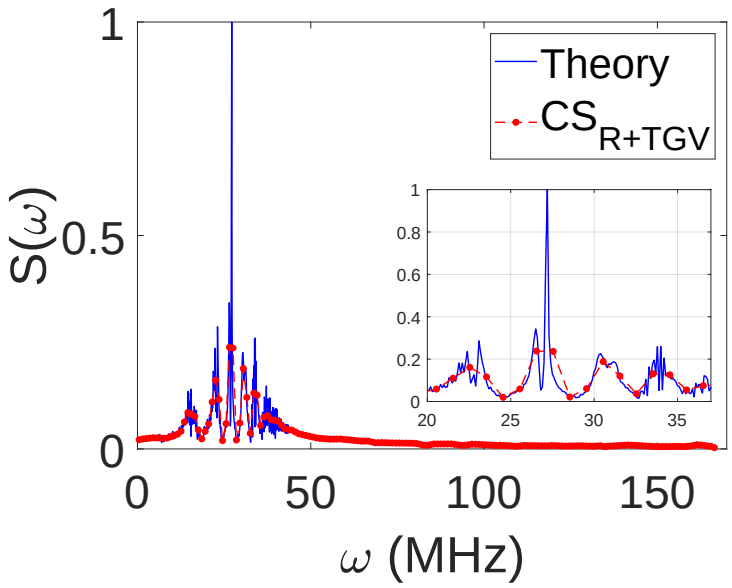


Figure 4.4: (a) A reconstruction of the noise spectrum of an ensemble of nuclear spins interacting with an InAs/GaAs quantum dot (under an external magnetic field of B = 2 T at the Voigt geometry) using CS_{TGV}. The blue solid line represents the theoretically simulated noise spectrum, with the maximum intensity normalized to 1. The red dotted line represent the simulated reconstructed spectrum considering random pulse sequences with $(M, N_1, N_2) = (200, 200, 50)$ and $K = 70$ different Fourier basis functions. (b) Same experiments with the Rademacher measurements method. The blue solid line represents the theoretically simulated noise spectrum. The red dots represent the simulated reconstructed spectrum considering random pulse sequences with $K = 90$ different sequences.

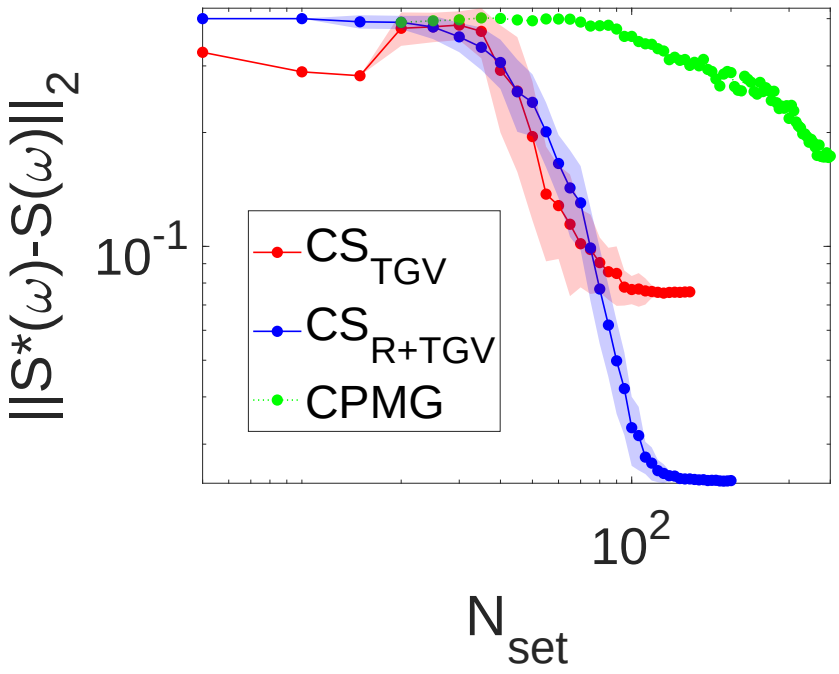


Figure 4.5: Accuracy of reconstructing the InAs/GaAs noise spectrum as a function of the number of sets of experiments, N_{set}. The solid blue line and the dashed red line represent the accuracy of CS with 2nd order TGV, and Rademacher measurements combined with TGV. The CS simulations are repeated for 30 times and the shaded areas represents the 95% confidence regimes. The dotted green line represents the reconstruction accuracy of the noise spectrum using the CPMG sequences.

We further quantify the accuracy of extracting the InAs/GaAs noise spectrum under different approaches. The reconstruction accuracy is defined as the L_2 norm of the difference between the reconstructed spectrum, $S^*(\omega)$, and the true spectrum, $S(\omega)$. The dotted red and blue lines in Fig. 4.5 represent the simulated reconstruction accuracies of CS_{TGV} and $\text{CS}_{\text{R+TGV}}$, respectively. For both methods, we have $N = 200$ grid points. In these simulations, we assume no experimental errors and only focus on the effect of the number of different sets of experiments, N_{set}. For both random pulse sequence methods, $N_{\text{set}} \approx K$. And for both methods, we observe a sharp change (phase transition) in the accuracy of reconstructing the spectrum.

We also compare the accuracies of both CS methods in resolving the InAs/GaAs noise spectrum to the ones obtained by using the conventional CPMG method (dotted green line in Fig. 4.5). For CPMG, the number of sets of experiments required for noise spectroscopy is given by $N_{\text{set}} = 2\omega_c T/\pi$, i.e., the number of different sequences that probe the noise spectrum over the frequency range $[0, \omega_c]$ given the total experiment time, T. When $N_{\text{set}} < 100$, the CPMG method can not resolve the peaks because of poor resolution. When $N_{\text{set}} > 100$, the accuracy in reconstruction decreases with a constant rate. In contrast, both CS methods experience a sharp phase transition, and gain decent speedup over the CPMG method.

4.5.2 Sensing with Fewer Pulses

As discussed in section 4.5.1, the Rademacher random pulse sequences, combined with TGV techniques, can be used to rapidly reconstruct the noise spectra of a quantum dot system. However, in some experimental platforms, it is difficult to apply large numbers of pulses to the qubits, due to undesirable physical effects such as laser-induced tunneling, or practical limitations

of the control electronics [80].

In this section, we show that we can even further reduce the number of pulses when performing Rademacher measurements. Recall from section 4.4 that the pulse sequence is controlled by a Rademacher random vector $\vec{U}$, with probability $p = 0.5$ that $U_m = 1$, and probability $1 - p = 0.5$ that $U_m = -1$. The expected number of pulses, N_p, we need to apply in the Rademacher random pulse sequences equals

$$N_p = M2p(1-p). \tag{4.20}$$

Equation 4.20 can be calculated by observing that we apply a pulse whenever $U_{m+1} \neq U_m$, which happens with probability $2p(1-p)$. As such, when p deviates from 0.5, the number of pulses decreases quadratically. We then investigate how the accuracy of the CS method changes when we adjust the value of p.

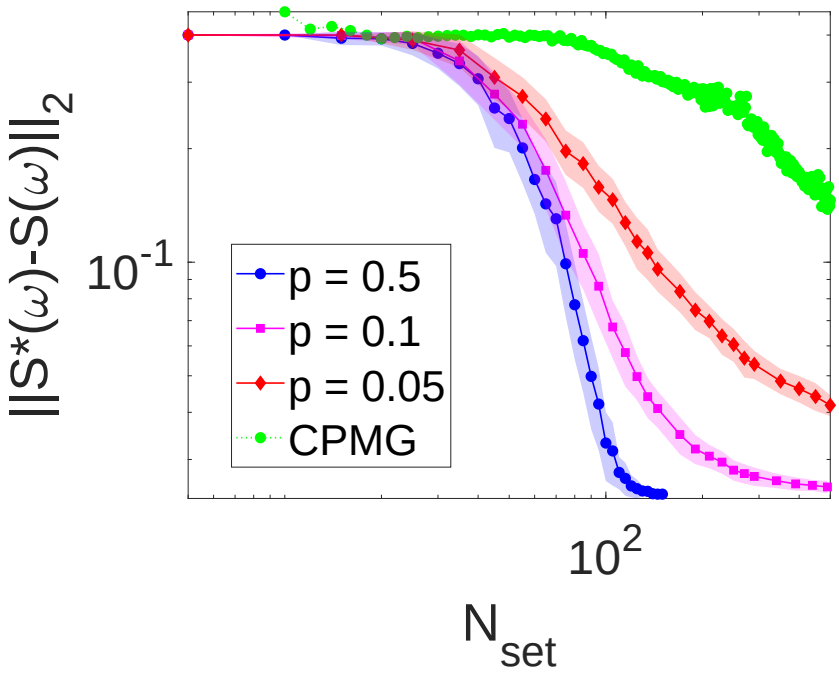


Figure 4.6: Numerical simulations of the accuracy of reconstructing the InAs/GaAs noise spectrum as a function of the number of sets of experiments, N_{set}. The blue dotted, magenta squared and red diamond lines represent the accuracy of Rademacher pulse sequences with $M = N = 200$ and $p = 0.5, 0.1, 0.05$, respectively. The corresponding averaged numbers of pulses are $N_p = 100, 36, 19$. The simulations are repeated for 40 times and the shaded areas represents the 95% confidence regimes. The dotted green line represents the reconstruction accuracy of the noise spectrum using the CPMG sequences. As p decreases, the speedup for the CS method gradually disappears.

Figure 4.6 shows the simulation of the accuracy of reconstructing the InAs/GaAs noise spectrum, similarly to what we have done in Fig. 4.5. The blue dotted, magenta squared, and red diamond lines represent the results of the Rademacher measurements with different probabilities, $p = 0.5, 0.2, 0.05$, respectively. In this simulation, the number of grid numbers equals the number of time segments, such that $N = M = 200$. So the corresponding expected value for the blue, magenta, and red dotted lines can be calculated via Eq. (4.20), with $N_p = 100, 64$ and 19. The green dotted line represents the result we get from the CPMG method. Note that the blue and

green dotted lines are identical to the dotted lines with the same color in Fig. 4.5.

We see that there is a regime for p in which the number of pulses we need is greatly decreased, while the loss in the efficiency of reconstructing the spectrum of InAs/GaAs is bearable, making this a potentially useful trade-off. For example, by setting $p = 0.1$, N_p is decreased down from 100 to only 36. Meanwhile, the threshold number of N_{set} for the accuracy to drop below 0.1 barely changed from 75 to 85, and remains an advantage over the conventional CPMG method.

4.6 Outlook

To conclude, we improve on the random pulse sequence method for qubit noise spectroscopy in two respects. We expand the method's applicability to CS of noise spectra with piecewise linear features, via TGV regularization. We also simplify the implementation of the method via Rademacher measurements when reconstructing sparse noise spectra. The proposed methods are verified through numerical simulations on realistic physical systems, such as optically-active quantum dots. Compared to previous work, these new developments broaden the reach of random pulse sequences and reduce the experimental complexity while preserving reconstruction accuracy. This brings the technique closer to experimental feasibility for quantum dots, and potentially also for other quantum systems, such as nitrogen vacancy centers [104].

For future research, we would like to further explore the class of noise spectra that can be rapidly reconstructed by random pulse sequences. For example, while piecewise linear modeling works well for many realistic physical systems, there are other possible approaches, such as model-based compressive sensing [40], which may be useful for characterization of noise spectra in current quantum computing platforms. There is also room for improvement, as well as encour-

aging recent progress [44, 47], in the theoretical recovery guarantees for compressed sensing in the scenarios studied in this paper, i.e., for reconstruction of 1-dimensional signals, using TGV regularization, and Rademacher measurements.

Appendix A: Appendices

A.1 Variance of the decay exponent: a special case

In this section, we illustrate a special case in Section 2.7.2 Case 3(e), where H consists of a single connected component with $l = k+1 = j+2 = i+3$. We compute the exact value of the fourth order term $\mathbb{E}(U_iU_jU_kU_l)$, which is rather complicated. We can again utilize the geometric interpretation of random pulses with hyper-plane tessellation: we now have 4 hyper-planes, indicated by 4 normal vectors, $\vec{V_1} = (a_0, a_1, 0, 0, 0)$, $\vec{V_2} = (0, a_0, a_1, 0, 0)$, $\vec{V_3} = (0, 0, a_0, a_1, 0)$ and $\vec{V_4} = (0, 0, 0, a_0, a_1)$, with $a_0a_1 = \frac{\pi}{2}\sin(R(1))$. For simplicity, we remove the irrelevant zeros in the vectors to reduce the dimension.

The hyper-planes cut the whole space into 16 pieces. In half of the separated spaces, the product $U_iU_jU_kU_l$ equals 1, while in the other half of the spaces, $U_iU_jU_kU_l$ equals -1. The problem now is to find the total solid angles of spaces with the same value. Define Ω_+ to be the total solid angle with $U_iU_jU_kU_l = 1$, and Ω_- for the part with $U_iU_jU_kU_l = -1$, so we have

$$\mathbb{E}(U_iU_jU_kU_l) = \frac{\Omega_+ - \Omega_-}{\Omega_+ + \Omega_-}. \tag{A.1}$$

This can be calculated with the help of Ribando's formula [119]:

$$\Omega = \Omega_d \frac{|\det(V)|}{(2\pi)^{d/2}} \sum_{\vec{a}} [\frac{(-2)^{\sum_{i<j} a_{ij}}}{\prod_{i<j} a_{ij}!} \prod_i \Gamma(\frac{1 + \sum_{m \neq i} a_{im}}{2})] \vec{\alpha}^{\vec{a}}. \tag{A.2}$$

In Ribando's formula, Ω_d represents the solid angle subtended by the $(d-1)$-dimensional spherical surface of a unit sphere, which equals $8\pi^2/3$ in our case ($d = 5$). V denote the matrix formed by the unit vectors defining the angle, which are the 4 normal vectors, $\vec{V}_i$. The multivariable $\vec{\alpha}$ contains the inner products of $\vec{V}_i$, with $\alpha_{ij} = \vec{V}_i \cdot \vec{V}_j$, $1 \leq i \leq j \leq 4$. The vector $\vec{a}$ is the corresponding integer multiexponent, with $a_{ji} = a_{ij}$ and $\vec{\alpha}^{\vec{a}} = \prod \alpha_{ij}^{a_i j}$. Define matrix M whose diagonal elements are 1 and off diagonal elements equals $-|\alpha_{ij}|$. Equation (A.2) will converge to the solid angle defined by the vectors if and only if M is positive definite, which is true in our scenario.

Note that all 16 solid angles can be defined by the 4 normal vectors by adding negative signs to them. So the multivariables that determine the solid angles can be written as $\vec{\alpha} = (\pm\frac{\pi}{2}\sin(R(1)), 0, 0, \pm\frac{\pi}{2}\sin(R(1)), 0, \pm\frac{\pi}{2}\sin(R(1)))$. The 16 pieces are reduced to 8 due to the symmetry of the hyper-plane tessellation. Furthermore, we define $\Omega_{\pm\pm\pm}$ to be the specific solid angle whose notes indicates the signs of the three non-zero elements in $\vec{\alpha}$, we have

$$\begin{aligned} \Omega_- &= 2(\Omega_{+++} + \Omega_{---} + \Omega_{-+-} + \Omega_{+-+}), \\ \Omega_+ &= 2(\Omega_{-++} + \Omega_{--+} + \Omega_{+--} + \Omega_{++-}). \end{aligned} \tag{A.3}$$

Now, substituting Eq. (A.3) and Eq. (A.2) into Eq. (A.1), we can find the value of $\mathbb{E}_{\{i,j,k,l\} \in F}(U_i U_j U_k U_l)$

as an infinite series involving $R(1)$:

$$\begin{aligned}
\mathbb{E}(U_iU_jU_kU_l) =& \frac{\sum_{a_1a_2a_3} G(a_1,a_2,a_3,R(1))(1+(-1)^{a_2}-(-1)^{a_1}-(-1)^{a_3})}{\sum_{a_1a_2a_3} G(a_1,a_2,a_3,R(1))(1+(-1)^{a_2}+(-1)^{a_1}+(-1)^{a_3})}, \\
G(a_1,a_2,a_3,R(1)) :=& \frac{(-2)^{a_1+a_2+a_3}}{\prod_i a_1!a_2!a_3!}\Gamma(\frac{1+a_1}{2})\Gamma(\frac{1+a_1+a_2}{2})\Gamma(\frac{1+a_2+a_3}{2})\Gamma(\frac{1+a_3}{2}) \\
& \cdot (\tfrac{\pi}{2}\sin(R(1)))^{a_1+a_2+a_3}(1+(-1)^{a_1+a_2+a_3}).
\end{aligned} \tag{A.4}$$

One trivial example is that when $R(1) = 0$, $\mathbb{E}(U_iU_jU_kU_l) = 0$. And when $R(1) = 1/3$, $\mathbb{E}(U_iU_jU_kU_l) = 2/15$.

Bibliography

[1] M. A. Nielsen and I. L. Chuang, *Quantum computation and quantum information*, 10th Anniversary Edition (Cambridge University Press, Cambridge, UK, 2010).

[2] T. D. Ladd, F. Jelezko, R. Laflamme, Y. Nakamura, C. Monroe, and J. L. O'Brien, Quantum computers, Nature **464**, 45 (2010).

[3] F. Arute, K. Arya, R. Babbush, and et al., Quantum supremacy using a programmable superconducting processor, Nature **574**, 505 (2019).

[4] C. Monroe, W. C. Campbell, L.-M. Duan, Z.-X. Gong, A. V. Gorshkov, P. W. Hess, R. Islam, K. Kim, G. Pagano, P. Richerme, C. Senko, and N. Y. Yao, Programmable quantum simulations of spin systems with trapped ions, Rev. Mod. Phys. **93**, 025001 (2021).

[5] A. G. Fowler, M. Mariantoni, J. M. Martinis, and A. N. Cleland, Surface codes: towards practical large-scale quantum computation, Phys. Rev. A **86**, 032324 (2012).

[6] B. M. Terhal, Quantum error correction for quantum memories, Rev. Mod. Phys. **87**, 307 (2015).

[7] C. L. Degen, F. Reinhard, and P. Cappellaro, Quantum sensing, Rev. Mod. Phys. **89**, 035002 (2017).

[8] D. Budker and M. Romalis, Optical magnetometry, Nat. Phys. **3**, 227 (2007).

[9] L. Viola, E. Knill, and S. Lloyd, Dynamical decoupling of open quantum systems, Physical Review Letters **82**, 2417 (1999).

[10] G. S. Uhrig, Keeping a quantum bit alive by optimized π-pulse sequences, Physical Review Letters **98**, 100504 (2007).

[11] M. J. Biercuk, H. Uys, A. P. VanDevender, N. Shiga, W. M. Itano, and J. J. Bollinger, Optimized dynamical decoupling in a model quantum memory, Nature **458**, 996 (2009).

[12] E. Novais, E. R. Mucciolo, and H. U. Baranger, Noise threshold for a dynamical decoupling-based quantum computer, Physical Review A **79**, 032318 (2009).

[13] P. Aliferis and J. Preskill, Fault-tolerant quantum computation against biased noise, Physical Review A **79**, 012332 (2009).

[14] H. K. Ng and J. Preskill, Fault-tolerant quantum computation versus gaussian noise, Physical Review A—Atomic, Molecular, and Optical Physics **79**, 032318 (2009).

[15] A. Seif, M. Hafezi, and Y.-K. Liu, Compressed sensing measurement of long-range correlated noise, arXiv preprint arXiv:2105.12589 (2021).

[16] R. Harper, W. Yu, and S. T. Flammia, Fast estimation of sparse quantum noise, PRX Quantum **2**, 010322 (2021).

[17] K. Huang, D. Farfurnik, A. Seif, M. Hafezi, and Y.-K. Liu, Random pulse sequences for qubit noise spectroscopy, Physical Review Applied **23**, 054090 (2025).

[18] H. Breuer and F. Petruccione, *The theory of open quantum systems* (Oxford University Press, USA, 2002).

[19] J. Bylander, S. Gustavsson, F. Yan, F. Yoshihara, K. Harrabi, G. Fitch, D. G. Cory, Y. Nakamura, J.-S. Tsai, and W. D. Oliver, Noise spectroscopy through dynamical decoupling with a superconducting flux qubit, Nature Physics **7**, 565 (2011).

[20] Y.-X. Wang and A. A. Clerk, Intrinsic and induced quantum quenches for enhancing qubit-based quantum noise spectroscopy, Nature communications **12**, 1 (2021).

[21] N. Bar-Gill, L. M. Pham, C. Belthangady, D. Le Sage, P. Cappellaro, J. Maze, M. D. Lukin, A. Yacoby, and R. Walsworth, Suppression of spin-bath dynamics for improved coherence of multi-spin-qubit systems, Nature communications **3**, 1 (2012).

[22] F. K. Malinowski, F. Martins, P. D. Nissen, E. Barnes, Ł. Cywiński, M. S. Rudner, S. Fallahi, G. C. Gardner, M. J. Manfra, C. M. Marcus, et al., Notch filtering the nuclear environment of a spin qubit, Nature nanotechnology **12**, 16 (2017).

[23] K. Chan, W. Huang, C. Yang, J. Hwang, B. Hensen, T. Tanttu, F. Hudson, K. M. Itoh, A. Laucht, A. Morello, et al., Assessment of a silicon quantum dot spin qubit environment via noise spectroscopy, Physical Review Applied **10**, 044017 (2018).

[24] T. Yuge, S. Sasaki, and Y. Hirayama, Measurement of the noise spectrum using a multiple-pulse sequence, Physical review letters **107**, 170504 (2011).

[25] S. Wimperis, Broadband, narrowband, and passband composite pulses for use in advanced nmr experiments, Journal of Magnetic Resonance, Series A **109**, 221 (1994).

[26] H. K. Cummins, G. Llewellyn, and J. A. Jones, Tackling systematic errors in quantum logic gates with composite rotations, Physical Review A **67**, 042308 (2003).

[27] C. E. Shannon, Communication in the presence of noise, Proceedings of the IRE **37**, 10 (1949).

[28] H. Nyquist, Certain topics in telegraph transmission theory, Transactions of the American Institute of Electrical Engineers **47**, 617 (1928).

[29] E. J. Candès, J. Romberg, and T. Tao, Robust uncertainty principles: exact signal reconstruction from highly incomplete frequency information, IEEE Transactions on Information Theory **52**, 489 (2006).

[30] D. L. Donoho, Compressed sensing, IEEE Transactions on Information Theory **52**, 1289 (2006).

[31] E. J. Candès and M. B. Wakin, An introduction to compressive sampling, IEEE Signal Processing Magazine **25**, 21 (2008).

[32] Y. C. Eldar and G. Kutyniok, Compressed sensing: theory and applications, Cambridge University Press (2012).

[33] S. Foucart and H. Rauhut, *A mathematical introduction to compressive sensing* (Springer Science & Business Media, 2013).

[34] D. Gross, Y.-K. Liu, S. T. Flammia, S. Becker, and J. Eisert, Quantum state tomography via compressed sensing, Physical Review Letters **105**, 150401 (2010).

[35] S. S. Chen, D. L. Donoho, and M. A. Saunders, Atomic decomposition by basis pursuit, SIAM Journal on Scientific Computing **20**, 33 (1998).

[36] E. J. Candès and T. Tao, Near-optimal signal recovery from random projections: universal encoding strategies?, IEEE Transactions on Information Theory **52**, 5406 (2006).

[37] R. Vershynin, Introduction to the non-asymptotic analysis of random matrices, arXiv preprint arXiv:1011.3027 (2010).

[38] R. Tibshirani, Regression shrinkage and selection via the lasso, Journal of the Royal Statistical Society: Series B (Methodological) **58**, 267 (1996).

[39] S. S. Chen, D. L. Donoho, and M. A. Saunders, Atomic decomposition by basis pursuit, SIAM Journal on Scientific Computing **20**, 33 (1998).

[40] R. G. Baraniuk, V. Cevher, M. F. Duarte, and C. Hegde, Model-based compressive sensing, IEEE Transactions on information theory **56**, 1982 (2010).

[41] D. Needell and R. Ward, Near-optimal compressed sensing guarantees for total variation minimization, IEEE transactions on image processing **22**, 3941 (2013).

[42] C. Poon, On the role of total variation in compressed sensing, SIAM Journal on Imaging Sciences **8**, 682 (2015).

[43] F. Krahmer, C. Kruschel, and M. Sandbichler, "Total variation minimization in compressed sensing", in Compressed sensing and its applications: second international matheon conference 2015 (Springer, 2018), pp. 333–358.

[44] M. Genzel, M. März, and R. Seidel, Compressed sensing with 1d total variation: breaking sample complexity barriers via non-uniform recovery, Information and Inference: A Journal of the IMA **11**, 203 (2022).

[45] E. J. Candès and B. Recht, Exact matrix completion via convex optimization, Foundations of Computational Mathematics **9**, 717 (2009).

[46] D. Gross, Recovering low-rank matrices from few coefficients in any basis, IEEE Transactions on Information Theory **57**, 1548 (2011).

[47] G. Huang and S. Li, Low-rank toeplitz matrix restoration: descent cone analysis and structured random matrix, IEEE Transactions on Information Theory (2025).

[48] L. I. Rudin, S. Osher, and E. Fatemi, Nonlinear total variation based noise removal algorithms, Physica D: Nonlinear Phenomena **60**, 259 (1992).

[49] E. J. Candès and B. Recht, Exact matrix completion via convex optimization, Foundations of Computational Mathematics **9**, 717 (2009).

[50] E. J. Candès and Y. Plan, Tight oracle inequalities for low-rank matrix recovery from a minimal number of noisy random measurements, IEEE Transactions on Information Theory **57**, 2342 (2011).

[51] F. Yan, J. Bylander, S. Gustavsson, F. Yoshihara, K. Harrabi, D. G. Cory, T. P. Orlando, Y. Nakamura, J.-S. Tsai, and W. D. Oliver, Spectroscopy of low-frequency noise and its temperature dependence in a superconducting qubit, Phys. Rev. B **85**, 174521 (2012).

[52] O. E. Dial, M. D. Shulman, S. P. Harvey, H. Bluhm, V. Umansky, and A. Yacoby, Charge noise spectroscopy using coherent exchange oscillations in a singlet-triplet qubit, Phys. Rev. Lett. **110**, 146804 (2013).

[53] J. T. Muhonen, J. P. Dehollain, A. Laucht, F. E. Hudson, R. Kalra, T. Sekiguchi, K. M. Itoh, D. N. Jamieson, J. C. McCallum, A. S. Dzurak, et al., Storing quantum information for 30 seconds in a nanoelectronic device, Nature nanotechnology **9**, 986 (2014).

[54] F. Reinhard, F. Shi, N. Zhao, F. Rempp, B. Naydenov, J. Meijer, L. T. Hall, L. Hollenberg, J. Du, R.-B. Liu, and J. Wrachtrup, Tuning a spin bath through the quantum-classical transition, Phys. Rev. Lett. **108**, 200402 (2012).

[55] Y. Romach, C. Müller, T. Unden, L. J. Rogers, T. Isoda, K. M. Itoh, M. Markham, A. Stacey, J. Meijer, S. Pezzagna, B. Naydenov, L. P. McGuinness, N. Bar-Gill, and F. Jelezko, Spectroscopy of surface-induced noise using shallow spins in diamond, Phys. Rev. Lett. **114**, 017601 (2015).

[56] G. A. Álvarez and D. Suter, Measuring the spectrum of colored noise by dynamical decoupling, Phys. Rev. Lett. **107**, 230501 (2011).

[57] K. C. Young and K. B. Whaley, Qubits as spectrometers of dephasing noise, Phys. Rev. A **86**, 012314 (2012).

[58] L. M. Norris, G. A. Paz-Silva, and L. Viola, Qubit noise spectroscopy for non-gaussian dephasing environments, Phys. Rev. Lett. **116**, 150503 (2016).

[59] G. A. Paz-Silva, L. M. Norris, and L. Viola, Multiqubit spectroscopy of gaussian quantum noise, Phys. Rev. A **95**, 022121 (2017).

[60] C. Ferrie, C. Granade, G. Paz-Silva, and H. M. Wiseman, Bayesian quantum noise spectroscopy, New Journal of Physics **20**, 123005 (2018).

[61] U. Haeberlen, *Advances in magnetic resonance*, Vol. 1 (Academic Press, 1976).

[62] L. M. Vandersypen and I. L. Chuang, Nmr techniques for quantum control and computation, Reviews of modern physics **76**, 1037 (2005).

[63] J. Preskill, Quantum Computing in the NISQ era and beyond, Quantum **2**, 79 (2018).

[64] K. Jaganathan, Y. C. Eldar, and B. Hassibi, Phase retrieval: an overview of recent developments, Optical Compressive Imaging, 279 (2016).

[65] F. Serinaldi and F. Lombardo, Betabit: a fast generator of autocorrelated binary processes for geophysical research, Europhysics Letters **118**, 30007 (2017).

[66] F. Serinaldi and F. Lombardo, General simulation algorithm for autocorrelated binary processes, Physical Review E **95**, 023312 (2017).

[67] K. Schultz, G. Quiroz, P. Titum, and B. Clader, Schwarma: a model-based approach for time-correlated noise in quantum circuits, Physical Review Research **3**, 033229 (2021).

[68] A. Murphy, J. Epstein, G. Quiroz, K. Schultz, L. Tewala, K. McElroy, C. Trout, B. Tien-Street, J. A. Hoffmann, B. Clader, et al., Universal-dephasing-noise injection via schrödinger-wave autoregressive moving-average models, Physical Review Research **4**, 013081 (2022).

[69] M. Woods, R. Groux, A. Chin, S. Huelga, and M. B. Plenio, Mappings of open quantum systems onto chain representations and markovian embeddings, Journal of Mathematical Physics **55**, 032101 (2014).

[70] U. Weiss, *Quantum dissipative systems,* (World Scientific, Singapore, 1993).

[71] K. Khodjasteh, T. Erdélyi, and L. Viola, Limits on preserving quantum coherence using multipulse control, Physical Review A **83**, 020305 (2011).

[72] Ł. Cywi ński, R. M. Lutchyn, C. P. Nave, and S. Das Sarma, How to enhance dephasing time in superconducting qubits, Phys. Rev. B **77**, 174509 (2008).

[73] G. Ithier, E. Collin, P. Joyez, P. Meeson, D. Vion, D. Esteve, F. Chiarello, A. Shnirman, Y. Makhlin, J. Schriefl, et al., Decoherence in a superconducting quantum bit circuit, Physical Review B—Condensed Matter and Materials Physics **72**, 134519 (2005).

[74] A. J. Leggett, S. Chakravarty, A. T. Dorsey, M. P. Fisher, A. Garg, and W. Zwerger, Dynamics of the dissipative two-state system, Reviews of Modern Physics **59**, 1 (1987).

[75] L. Viola and S. Lloyd, Dynamical suppression of decoherence in two-state quantum systems, Physical Review A **58**, 2733 (1998).

[76] G. S. Uhrig, Exact results on dynamical decoupling by π pulses in quantum information processes, New Journal of Physics **10**, 083024 (2008).

[77] G. A. Paz-Silva and L. Viola, General transfer-function approach to noise filtering in open-loop quantum control, Phys. Rev. Lett. **113**, 250501 (2014).

[78] G. A. Paz-Silva, L. M. Norris, and L. Viola, Multiqubit spectroscopy of gaussian quantum noise, Phys. Rev. A **95**, 022121 (2017).

[79] T. Yuge, S. Sasaki, and Y. Hirayama, Measurement of the noise spectrum using a multiple-pulse sequence, Physical review letters **107**, 170504 (2011).

[80] D. Farfurnik, H. Singh, Z. Luo, A. S. Bracker, S. G. Carter, R. M. Pettit, and E. Waks, All-optical noise spectroscopy of a solid-state spin, Nano Lett. 23, 1781–1786 (2023).

[81] P. Szańkowski and Ł. Cywiński, Accuracy of dynamical-decoupling-based spectroscopy of gaussian noise, Physical Review A **97**, 032101 (2018).

[82] P. Szańkowski, Transition between continuous and discrete spectra in dynamical-decoupling noise spectroscopy, Physical Review A **100**, 052115 (2019).

[83] M. Rosenblatt, *Stationary sequences and random fields* (Springer Science & Business Media, 2012).

[84] *Fejer-Riesz theorem*, Encyclopedia of Mathematics, http://encyclopediaofmath.org/index.php?title=Fej%C3%A9r-Riesz_theorem&oldid=53455, 2023.

[85] L. Fejér, Über trigonometrische polynome. (1916).

[86] T. P. Speed and H. T. Kiiveri, Gaussian markov distributions over finite graphs, The Annals of Statistics, 138 (1986).

[87] M. R. Jerrum, L. G. Valiant, and V. V. Vazirani, Random generation of combinatorial structures from a uniform distribution, Theoretical computer science **43**, 169 (1986).

[88] A. S. Nemirovskij and D. B. Yudin, Problem complexity and method efficiency in optimization, (1983).

[89] A. Kwiatkowski, "Optimized experiment design and analysis for fully randomized benchmarking", PhD thesis (University of Colorado at Boulder, 2024).

[90] W. Gautschi, Algorithm 726: orthpol–a package of routines for generating orthogonal polynomials and gauss-type quadrature rules, ACM Transactions on Mathematical Software (TOMS) **20**, 21 (1994).

[91] S. R. White and A. E. Feiguin, Real-time evolution using the density matrix renormalization group, Physical review letters **93**, 076401 (2004).

[92] A. J. Daley, C. Kollath, U. Schollwöck, and G. Vidal, Time-dependent density-matrix renormalization-group using adaptive effective hilbertspaces, Journal of Statistical Mechanics: Theory and Experiment **2004**, P04005 (2004).

[93] E. J. Candès and Y. Plan, A probabilistic and ripless theory of compressed sensing, IEEE Transactions on Information Theory **57**, 7235 (2011).

[94] K. Seetharam, D. Biswas, C. Noel, A. Risinger, D. Zhu, O. Katz, S. Chattopadhyay, M. Cetina, C. Monroe, E. Demler, et al., Digital quantum simulation of nmr experiments, Science Advances **9**, eadh2594 (2023).

[95] M. Bostock and D. Nietlispach, Compressed sensing: reconstruction of non-uniformly sampled multidimensional nmr data, Concepts in Magnetic Resonance Part A **46**, e21438 (2017).

[96] R. Stockill, C. Le Gall, C. Matthiesen, L. Huthmacher, E. Clarke, M. Hugues, and M. Atatüre, Quantum dot spin coherence governed by a strained nuclear environment, Nature communications **7**, 1 (2016).

[97] T. Hastie, R. Tibshirani, J. H. Friedman, and J. H. Friedman, *The elements of statistical learning: data mining, inference, and prediction*, Vol. 2 (Springer, 2009).

[98] J. Choi, H. Zhou, H. S. Knowles, R. Landig, S. Choi, and M. D. Lukin, Robust dynamic hamiltonian engineering of many-body spin systems, Physical Review X **10**, 031002 (2020).

[99] *Ionq harmony*, https://ionq.com/quantum-systems/harmony.

[100] Q.-M. Chen, H. Rabitz, and R.-B. Wu, Quantum optimal control without arbitrary waveform generators, Phys. Rev. Appl. **20**, 064016 (2023).

[101] E. J. Candès and C. Fernandez-Granda, Towards a mathematical theory of super-resolution, Communications on Pure and Applied Mathematics **67**, 906 (2014).

[102] G. Tang, B. N. Bhaskar, P. Shah, and B. Recht, Compressed sensing off the grid, IEEE Transactions on Information Theory **59**, 7465 (2013).

[103] Y. Chi and M. F. Da Costa, Harnessing sparsity over the continuum: atomic norm minimization for superresolution, IEEE Signal Processing Magazine **37**, 39 (2020).

[104] Y. Romach, A. Lazariev, I. Avrahami, F. Kleißler, S. Arroyo-Camejo, and N. Bar-Gill, Measuring environmental quantum noise exhibiting a nonmonotonic spectral shape, Physical Review Applied **11**, 014064 (2019).

[105] K. Huang, *Data for random pulse sequences for qubit noise spectroscopy*, DOI: https://doi.org/10.5281/zenodo.15374840, May 2025.

[106] Ł. Cywiński, R. M. Lutchyn, C. P. Nave, and S. Das Sarma, How to enhance dephasing time in superconducting qubits, Physical Review B **77**, 174509 (2008).

[107] M. J. Biercuk, A. C. Doherty, and H. Uys, Dynamical decoupling sequence construction as a filter-design problem, Journal of Physics B: Atomic, Molecular and Optical Physics **44**, 154002 (2011).

[108] C. L. Degen, F. Reinhard, and P. Cappellaro, Quantum sensing, Reviews of Modern Physics **89**, 035002 (2017).

[109] L. M. Norris, G. A. Paz-Silva, and L. Viola, Optimally band-limited spectroscopy of control noise using a qubit sensor, Physical Review Letters **116**, 150503 (2016).

[110] T. Roger, M. Berta, and S. Wehner, Spectrum estimation for arbitrary quantum processes using compressive sensing, npj Quantum Information **4**, 28 (2018).

[111] K. Bredies, K. Kunisch, and T. Pock, Total generalized variation, SIAM Journal on Imaging Sciences **3**, 492 (2010).

[112] F. Knoll, K. Bredies, T. Pock, and R. Stollberger, Second order total generalized variation (tgv) for mri, Magnetic resonance in medicine **65**, 480 (2011).

[113] F. I. Karahanoglu, I. Bayram, and D. Van De Ville, A signal processing approach to generalized 1-d total variation, IEEE Transactions on Signal Processing **59**, 5265 (2011).

[114] M. A. T. Figueiredo, R. D. Nowak, and S. J. Wright, Gradient projection for sparse reconstruction: application to compressed sensing and other inverse problems, IEEE Journal of Selected Topics in Signal Processing **1**, 586 (2007).

[115] E. J. Candès, M. B. Wakin, and S. P. Boyd, Enhancing sparsity by reweighted ℓ_1 minimization, Journal of Fourier Analysis and Applications **14**, 877 (2008).

[116] E. J. Candes, Y. C. Eldar, D. Needell, and P. Randall, Compressed sensing with coherent and redundant dictionaries, Applied and Computational Harmonic Analysis **31**, 59 (2011).

[117] G. Ongie and M. Jacob, Off-the-grid recovery of piecewise constant images from few fourier samples, SIAM Journal on Imaging Sciences **9**, 1004 (2016).

[118] P. Liu, L. Xiao, and J. Zhang, Fast second degree total variation method for image compressive sensing, Plos one **10**, e0137115 (2015).

[119] J. M. Ribando, Measuring solid angles beyond dimension three, Discrete & Computational Geometry **36**, 479 (2006).